Fall 1-31-1994

An investigation of the formation of turbulent water and abrasive water jets

Md. Ekramul Hasan Khan
New Jersey Institute of Technology

ABSTRACT

An Investigation of the Formation of Turbulent Water and Abrasive Water Jets

by
Md. Ekramul Hasan Khan

This study is concerned with the development of a knowledge base for the selection of nozzle geometry by investigating the mechanism of formation and behaviors of water and abrasive water jets. A numerical prediction of turbulent water flow inside various nozzles is developed. The analysis is based on the numerical solution of conservation equations of continuity and momentum as well as equations of turbulent kinetic energy and dissipation for 2-dimensional axisymmetric flow by using a finite element package, FIDAP.

The technique for determining velocities and forces of water jet and abrasive water jet with the Laser Transit Anemometer and Piezoelectric Force Transducer is validated by numerical prediction from the formulation indicated above. The velocity ratio of abrasive to water particle is about 0.45-0.65 which primarily depends on the alignment of the carbide tube and sapphire nozzle as well as on the mixing process.

The numerically predicted velocity at the nozzle exit complies generally well with the experimental data. The converging nozzles produce a concentrated high velocity jet which can be used for conventional cutting operations whereas the nozzles with diverging section produce cavities and circulation around jet which can be used for cleaning and polishing purposes. The conventional nozzle is diverging type and produces jets with a pulsing nature having particles accumulated and segregated cavities inside the jet as identified by high speed filming. The integration of experimental and numerical results provide a knowledge base for the nozzle design in various industrial applications.

AN INVESTIGATION OF THE FORMATION OF TURBULENT WATER AND ABRASIVE WATER JETS

by
Md. Ekramul Hasan Khan

A Dissertation
Submitted to the Faculty of the
New Jersey Institute of Technology
in Partial Fulfillment of the Requirements for the Degree of
Doctor of Philosophy

Department of Mechanical and Industrial Engineering

January 1994

APPROVAL PAGE

AN INVESTIGATION OF THE FORMATION OF TURBULENT WATER AND ABRASIVE WATER JETS

Md. Ekramul Hasan Khan

Dr. Ernest S. Geskin, Dissertation Advisor — Date
Professor of Mechanical Engineering
of the Department of Mechanical and Industrial Engineering, NJIT

Dr. Rong Chen, Committee Member — Date
Professor of Mechanical Engineering and Graduate Advisor
of the Department of Mechanical and Industrial Engineering, NJIT

Dr. Avraham Harnoy, Committee Member — Date
Associate Professor of Mechanical Engineering
of the Department of Mechanical and Industrial Engineering, NJIT

Dr. Nouri Levy, Committee Member — Date
Associate Professor of Mechanical Engineering
of the Department of Mechanical and Industrial Engineering, NJIT

Dr. Eugene Gordon, Committee Member — Date
Distinguished Professor of Electrical Engineering
of the Department of Electrical and Computer Engineering, NJIT

BIOGRAPHICAL SKETCH

Author: Md. Ekramul Hasan Khan

Degree: Doctor of Philosophy

Date: January 1994

Undergraduate and Graduate Education:

- Doctor of Philosophy in Mechanical Engineering, New Jersey Institute of Technology, Newark, NJ, 1994
- Master of Science in Mechanical Engineering, New Jersey Institute of Technology, Newark, NJ, 1990
- Bachelor of Science in Mechanical Engineering, Bangladesh University of Engineering & Technology, Dhaka, Bangladesh, 1983

Major: Mechanical Engineering

Presentations and Publications:

Khan, M. E. H. and Geskin, E. S. 1993. "Numerical Study of the Formation of High Speed Water Jets." *Eastern Regional Rotating Machinery Conference.* Sommerset, NJ. Vol. 2.

Khan, M. E. H. and Geskin, E. S. 1993. "A Numerical Investigation of Turbulent Behaviors of Water Flow Inside Nozzle." *Seventh American Water Jet Conference.* Seattle, Washington.

Khan, M. E. H. and Geskin, E. S. 1993. "An Investigation of Turbulent Water and Slurry Flows in the Course of Water Jet Machining." *The ASME Graduate Student Technical Conference for Region I and II.* Polytechnic University, New York.

Khan, M. E. H. and Geskin, E. S. 1992. "Investigation of Formation and Development of Highly Turbulent Water Jet." *Third Pacific Rim International Conference on Water Jet Technology.* Tainan, Taiwan. 3: 59-78.

BIOGRAPHICAL SKETCH
(Continued)

Geskin, E. S., Chen, W. L., Hu, F. and Khan, M. E. H. 1990. "Investigation of Abrasive Water Jet Machining." *NSF Annual Report.* University of Texas, Austin.

Khan, M. E. H. 1990. "An Investigation of the Dynamics of Abrasive Water Jet Formation." *MS Thesis.* New Jersey Institute of Technology.

Geskin, E. S., Chen, W. L., Chen, S. S., Hu, F., Khan, M. E. H., Kim, S., Singh, P. and Ferguson, R. 1989. "Investigation of Anatomy of An Abrasive Water Jet." *Fifth American Water Jet Conference.* Toronto, Canada. 5: 217-230.

This dissertation is dedicated to
my parents

ACKNOWLEDGMENT

The author wishes to express his sincere gratitude to his advisor, Professor E. S. Geskin, for his guidance, friendship, and moral support throughout this research. It was an honor to work under the guidance of such an esteemed researcher.

Special thanks to Professors R. Chen, A. Harnoy, N. Levy and E. Gordon for serving as members of committee and providing valuable suggestions in this study.

The author is grateful to the Department of Mechanical & Industrial Engineering, NJIT for funding of the research and to NSF for further and continued funding for this investigation.

The author wishes to thank Pittsburgh Super Computer Center and the Sun Work-Station of Mechanical & Industrial Engineering Department, NJIT for providing computing support.

The author appreciates the timely help and suggestions from Moududur Rahman, Jo-fei Chao, Alan Bondhus, Andy Zantzen and Tom Ursin.

And finally, a sincere thank you to the author's family, especially, his sister, Quamrun Nahar Khanam and his wife, Nazneen Karim Shilpee for their help and encouragement.

TABLE OF CONTENTS

TABLE OF CONTENTS
(Continued)

TABLE OF CONTENTS
(Continued)

Chapter **Page**

TABLE OF CONTENTS
(Continued)

Chapter **Page**

LIST OF TABLES

LIST OF FIGURES

LIST OF FIGURES
(Continued)

LIST OF FIGURES
(Continued)

LIST OF FIGURES
(Continued)

Figure **Page**

LIST OF SYMBOLS

Symbols	Meaning
D	Carbide tube nozzle diameter
d	Sapphire nozzle orifice diameter
f_i (i=1,2)	body force components per unit mass
g_i (i=1,2)	gravitational force components
k	turbulence kinetic energy
l_m	Prandtl's mixing length
P	stagnation water pressure
p	fluid pressure
r	radius of the orifice
r_k (k=1,2..)	radial distance from symmetric axis
t	time
u	velocity component along axis
u_i (i=1,2)	Eulerian fluid velocity components
v	velocity component along radius
x	stand off distance from nozzle tip
x_i (i=1,2)	Cartesian coordinates of a point in the fluid
y	coordinate normal to the wall
z_k (k=1,2..)	axial distance in computational domain
σ_{ij} (i,j=1,2)	Kronecker delta
ε	turbulent dissipation
ρ	density
μ	dynamic viscosity
μ_0	laminar viscosity
μ_t	eddy viscosity

CHAPTER 1

INTRODUCTION

Since 1972, the uses of water jet (WJ) have spread, almost worldwide, from simple cleaning to decommissioning of nuclear installations and promising novel medical and other applications. High pressure water jets have been used in coal mines and other industries where fire hazard becomes common due to frictional heating. Again cavijet and pulsed jet have been used widely in the industry due to their highly destructive nature. In the formation of water jet, water is pressurized up to 345 MPa and expelled through a water nozzle to form a coherent and high velocity jet.

Abrasive water jet (AWJ) is an extension of water jet cutting technology. High pressure water is spilled out from water nozzle causing negative pressure in the mixing chamber, sucking abrasive from the side port and forming the abrasive water jet. The high velocity differential between water and abrasive particles and violent turbulent mixing resulting in reduction of over all velocity and enhancement of pulses. The corrosive nature of AWJ is a novel gift for cutting operation. The AWJ is a single point tool, which may be pointed in almost any direction, and is capable of cutting almost every kind of material. The cutting of material is a process in which material removal takes place due to the erosion of abrasive particles and continuous bombardment of droplets caused fatigue failure.

When cutting, drilling or turning operation is carried out, the objective is to attain higher velocity with minimum jet dispersion. In order to achieve high water pressure in the zone of the jet-workpiece interaction, it is necessary to understand the mechanism of jet integration, dissipation of turbulent kinetic energy and formation of cavities and pulses. This, however, requires a thorough investigation of flow inside and outside of the nozzles.

This is unfortunate that to date an adequate model to predict the flow field of the high velocity WJ and AWJ has not been developed.

The study of erosion mechanism requires the understanding of turbulent nature of the jet and the stresses developed in the cutting zone. The parameters affecting the fluid dynamics characteristics of the jet are as follows:

- supply water pressure (P) and flow rate (Q)
- geometry and orifice diameter (d_n) of water nozzle
- length (l_c) and diameter of slurry nozzle (d_c)
- type and size (d_a) of abrasive material
- mass flow rate of abrasive (m_a)

Although a substantial part of prior research has been carried out in the analysis of jet-workpiece interaction, the available information is not sufficient to describe WJ and AWJ dynamics completely. The objective of this investigation is to provide comprehensive information about jet formation, its dynamic behavior and the effect of parameters in nozzle design. To determine the jet behaviors and its fluid dynamics, it requires velocity and force measurements and an instantaneous picture of the jet. Since velocity and pressure mainly depend on the upstream characteristics of the flow, it has become essential to investigate the flow structure inside the nozzle and the conditions of jet formation. To investigate the flow characteristics inside the nozzle and the relative dependency of jet characteristics, a numerical technique is an efficient off-line prediction of the flow. The second objective of this research is to optimize the nozzle parameters with respect to the dynamics of the jet by numerical analysis of flow.

Since the jet is highly turbulent and destructive in nature, it is impossible to measure the jet velocity and forces developed in the work-piece directly. The non-intrusive approach is the only reliable way to determine these parameters. Considerable efforts has been made to develop practical techniques for determining WJ and AWJ velocities. Goldstein (1976) used Schlieren photography in supersonic flow measurement.

Unfortunately, this technique does not work well in the case of high velocity water jet since Mach lines produced by water particles and abrasive particles are not distinguishable. In 1990 W. L. Chen successfully used the Laser Transit Anemometer (LTA) to determine water and abrasive velocity of the jet. This technique as well as Laser Doppler Anemometer (LDA) were employed for velocity investigation of the jet. A Piezo-electric force transducer was used for measuring the jet force in the workpiece. Instantaneous behaviors of jets were recorded by taking photographs with a camera of speed 8000 frames per second where a copper-vapor laser was employed as the light source. This provides the qualitative information of the jet velocity.

Experimental flow investigation inside nozzle is a difficult task, hence, a numerical approach is developed based on finite element discretization of continuity, momentum and empirical k - ε turbulence equations. The k - ε turbulence model with finite element technique is chosen for its robust application in the field of flow separation. The Prandtl's mixing length approach has been tried but it could not handle wide separation and vortex inside nozzle. The information obtained from numerical computation is verified by the available experimental results. The integration of experimental and numerical results provides a knowledge base for the selection of the nozzle geometry in various industrial applications.

This thesis contains six chapters. The previous fundamental studies on WJ and AWJ are discussed chronologically in Chapter 2. The experimental approaches used in the investigation of velocities, forces and dynamic behaviors of jets are demonstrated in Chapter 3. The details of numerical technique, finite element formulation, computational domains and prescribed boundary conditions of the model are discussed in Chapter 4. In Chapter 5, the results of experimental and computational analysis, the effects of nozzle parameters and a comparison are presented. Conclusions and recommendations are made in Chapter 6.

CHAPTER 2

LITERATURE SURVEY

There are a number of researches, citations and publications concerned with water jet and abrasive water jet technologies. Most of the authors, however, discuss the applications and optimizations of cutting parameters. In this chapter, the published works related to hydrodynamic properties of jets as well as technical approaches for measuring velocity, force, pressure and turbulent characteristics of the jets and visualization of jet structure are reviewed. The prior studies of the flow characteristics inside the nozzles are also presented in this section.

2.1 Hydrodynamics of Jets

2.1.1. Water Jets

Dune and Cassen (1954) studied the supersonic liquid jet in air using photographic equipment which allowed to two successive frames to be taken on the same photographic plate, from 10 to 120 microseconds apart. At high jet velocities another type breakup was noticed besides the classical Rayleigh surface tension breakup, and the sinuous aerodynamic breakup. The authors found formation of rotationally symmetric waves which were broken by the wind-produced waves on a body of water. In 1956, Dunne and Cassen published their detailed work on the instability of high speed water jet. They used the same shadow graph technique at the interval of 30 microseconds and four successive quarter-microsecond exposures were taken using jets of water and ethanol in external atmospheres of air and helium. The authors showed theoretically that the velocity discontinuity was advanced through the jet with an instantaneous mean velocities of the particles immediately in front of and behind the discontinuity.

Semerchan et al. (1958) applied the classical momentum balance technique to determine the boundaries of a free jet in the air with supersonic water velocity. From the conicity of the jet in different fluid media, they determined the density of the moving medium at different points which in turn made it possible to find the velocity field and the distribution of kinetic energy in liquid jets of supersonic velocity with some errors.

Leach and Walker (1966) investigated water jets by optical and X-ray photography to determine the jet velocity and pressure on target materials. They used the Bernoulli's equation to compute the velocity and concluded that the shape of nozzles had a profound effect on jet pressure. They formulated an equation for pressure distribution on the target plate which predicted that pressure would fall to zero at about 2.6 jet radii and this was verified by the experimental data.

Shavlovsky (1972) presented the dynamics and structure of fine continuous water jets at pressure up to 50 MPa. The analysis showed that the conical nozzle with 10 -14 degree of convergence and the cylindrical attachment with the length of four times of orifice diameter produced maximum initial section of the jet. It was found that the compact jet could be generated only if the nozzle internal surface were highly polished.

Phinney (1973) employed an electrical method of detecting and measuring the breakup of turbulent liquid jets. It was found that the exit disturbance level which was amplified by the ambient atmosphere was the main cause of jet breakup. For long nozzles, the turbulence level at the exit reached an equilibrium value that did not depend upon the length. The experiment was performed at relatively low Reynolds numbers and hence at higher exit speed or ambient densities, the breakup mechanism would undergo a transition to some other mode that was not experienced in these tests.

The mechanics of high speed liquid jets was studied by Field and Lesser (1977) both experimentally and theoretically. The experimental works involved the use of an Imacon image converter camera to follow the mechanical events at micro-second framing intervals. The theoretical investigation employed similarity arguments and the Tschaplygin

transformation to investigate the role of liquid over-compression in the process of the jet emergence. It was found that subsonic jets would not undergo the violent decompression process that was predicted for supersonic jets.

Flow characteristics of water jets in air was investigated by Yanaida and Ohashi (1978). Their theoretical analysis was verified by an electrical method and by laser velocimeter. Their electric system consisted of gate circuit that allowed fast pulses of current through the jet when it was continuous. Table salt in the water provided the necessary conductivity. In their model a position was found where jet was continuous 50% of the time. The jet length at this position was defined as average break up length. The Laser velocimeter was a 2 focus system similar to the Laser Transit Anemometer (LTA) where the time was recorded for a certain separation distance of the two beams. The velocity of the droplet flow was then determined from this time delay. The authors characterized the water jets into three regions such as continuous flow region, droplet flow region and diffused region based on axial velocity and breakup length.

Baker and Selberg (1978) used five different nozzles to study the coherence of the jets. They found that the jets which appeared to be breaking up in the photographs had a limited cutting capability.

Davies et al. (1980) presented experimental results on water jet structure for three different nozzles using flash photography and piezo-electric force transducer. They showed that for the stand off distances used the tapered nozzles produced the most coherent jets and exhibited higher impact forces on target materials. It was found that the significant deceleration only began when the jets started to break into discrete packets of water. The authors used nozzles having diameters larger than 0.03 m and the pressure ranged from 1-2 MPa at stand off distances of x/d=300-500.

Eddingfield et al. (1981) proposed a two-dimensional axisymmetric multicomponent mathematical model which coupled the three flow fields such as

continuous water, entrained air and droplet respectively. Their model, however, did not indicate the correlation for continuity and momentum transfer terms.

Edwards et al. (1982) studied water jets using different ambient media. The authors showed that the jets traveling in air had lower coherence than the jet developed in vacuum. They constructed a theoretical model to account for observed droplet trajectories based on the magnus-effect of aerodynamic lift.

Amano et al. (1982) carried out theoretical and experimental investigation on the characteristics of the turbulent axisymmetric jets impinging on a flat plate. The turbulence model in this computation was a two-equation k-ε model with standard Navier-Stokes equations which were solved by the hybrid scheme of central and backward finite differencing techniques. Their velocity coefficient of 0.9 and 5.5 power velocity profile gave good agreement with experimental results. The turbulence intensity produced in the nozzle did not affect the total force but only the stagnation pressure.

Noumi and Yamamoto (1992) investigated the flow characteristics and impact phenomena of pulsed water jets. They used pulse jet by piston impact in straight nozzles and carried out the experiments with high speed camera to determine the leading edge velocities and impact pressure of the jet. The authors showed that the flow in nozzles reached a quasi-steady state after short transition and the separation with strong cavitation formed in straight section of the nozzle outlet. The dense jet with radial expansion experienced increasing leading edge velocity and generating intensive water hammer at the impacted area as stagnation pressure decreased.

Vijay et al. (1993) investigated enhancement using cavitating jets. The authors used different configurations of the nozzles for numerical simulations and found the performance of artificially submerged cavitating jets operating at identical conditions surpassed that of fully submerged or noncavitating jets. They suggested that the enhancement of performance mainly depends on nozzle configurations which required further investigations.

2.1.2. Abrasive Water Jets

Hjelmeflt and Mockros (1965) investigated the motion of discrete particles in a turbulent fluid. The authors determined the deviations of particle motion from fluid motion by various approximations and found that only for high density ratios and small particles, the effects of added mass, history of acceleration and pressure gradient was insignificant. Their approximation became invalid for sediment transport and motion of gas bubbles in liquids.

Distribution of mass, velocity and intensity of turbulence in a two phase turbulent jet were analyzed by Hetsroni and Sokolov (1971). It was found that the two phase jet was narrower than the single phase one, with smaller normalized velocity fluctuations. The authors showed the discontinuities were proportional to the droplets' concentration and suppressed turbulence in the dissipation range at high wave numbers. Their analysis was confined to liquid droplet in an air medium.

Parthasarathy and Faeth (1987) developed a model to investigate the structure of particle-laden turbulent water jets in a still water. The authors simulated flow by considering three limiting cases: locally homogeneous flow, deterministic separated flow and stochastic separated flow. They found best agreement of measurements with stochastic analysis.

Swanson et al. (1987) investigated abrasive particle behavior based on experimental determination of particle velocity. They mixed magnetic particles with conventional garnet sand and which was then injected into a water jet. The resulting cutting stream was then directed through a pair of current-carrying coils spaced a fixed distance apart. The magnetic particles induced a signal in each of the coils which they recorded in a digital transient recorder. Measurement of the time between the signal response from each of the coils yielded a measure of the particle velocity. The authors noticed the inefficient mixing process of abrasive water jets since water jet velocity of 550 m/s induced abrasive velocities of only 120 m/s.

Hishida et al. (1989) investigated the turbulent structure of a liquid-solid particle confined jet. A modified LDV with particle size discrimination permitted detailed measurements of velocity for each phase. The authors observed that the liquid velocity increased in two-phase flow since the slip velocity between solid and liquid phases became larger in the down stream direction. The ratio of velocity fluctuation and turbulent Reynolds shear stress to local velocity difference between the centerline and the outer flow region decreased due to the existence of particles. The authors used glass particles with an arithmetic mean diameter of 479 μm at a constant mass loading ratio of 2.59% and a pipe Reynolds number of 9000.

Chen (1990) employed LTA for velocity investigation of water and abrasive water jets. In this work, the author validated results by measuring velocities with schlieren photography and demonstrated a weak relationship between velocities and operating parameters. The regression equation has the form:

$$\frac{V_{c.w.} - V_a}{V_{s.w.}} = 0.627\left(\frac{Q_a}{Q_w}\right)^{2.557(D_o/D_t)^2} \qquad (2.1)$$

where,

V_a : velocity of abrasive particles

$V_{c.w.}$: velocity of water jet at the exit of the focusing tube

$V_{s.w.}$: velocity of water jet at the exit of water nozzle

Q_a : volume flow rate of abrasive particle

Q_w : volume flow rate of water

D_o : diameter of water nozzle

D_t : diameter of focusing tube

The effect of other variables was limited.

A similar study was carried out by Himmelreich and Riess (1991) by the use of a Laser-2-Focus method. This investigation was limited to the pressure of 100 MPa. The authors depicted a pattern of flow behaviors similar to that observed by Chen (1990).

Neusen et al. (1992) used forward-scatter LDV system to measure abrasive water jet velocity. This method could not discriminate between the velocities of particles and water drops. However, their investigation of velocities gave an indication of the effectiveness of the momentum interchange from water drops to abrasive particles.

2.2 Flow Characteristics Inside Nozzles and Diffusers

The hydraulic diffuser is one of the most common engineering devices in water jet technology and it has some similarity with sapphire water jet nozzle. Because of this, the understanding of the dynamics of the flow in the diffusers constituted the basis for numerical prediction techniques developed in the presented work.

Tropea and et al. (1989) used LDA operated in forward scatter for the study of the flow field in three axisymmetric expansions having diffusers half angles of 30^{o}, 45^{o} and 90^{o} respectively. They found that the diffuser geometry had profound influence on the separated shear layer over the entire length of the diffuser section. The formation of turbulence immediately after separation was much higher in the case of smaller angle compared to higher angle expansion, leading to higher diffusion rates of separated shear layer, and hence earlier reattachment of the shear layer.

Sala et al. (1980) modeled two (k-ε) equations for the prediction of flow characteristics of the axisymmetric diffusers with half angles of 15^{o}, 30^{o}, 45^{o} and 90^{o}. In their analysis static pressure distribution was more flattened than the experimental data, due to the underestimation of normal turbulent stresses. They also overestimated the shear stresses which counter blocked kinetic energy and momentum analysis. Their model could not predict some quantities well when recirculation regions were present as in wide angled diffusers.

Habib and Whitelaw (1982) developed a numerical method of calculating the properties of axisymmetric swirling and non swirling (swirling numbers of 0 and 0.93) turbulent recirculating flows in wide-angle (with expansion half angles of 20^{o} and 45^{o}) diffusers. They found the consistency of velocity and kinetic energy with measurements for zero swirl number. Their turbulent kinetic energy were always significantly different from measurements, and the difference increased with swirl. They predicted the defects of the numerical computation were due to the model's isotropic characteristics and inability to represent large stream line curvature and rotation. In their analysis they only found the effect of diffuser angles and swirling on flow field. But the upstream effect due to flow in different nozzle geometry is not presented in their analysis.

Baskharone (1991) developed a finite-element model of the turbulent flow field in the annular exhaust diffuser of a gas turbine. He used a modified version of the Petrov-Galerkin weighted residual method, coupled with a highly accurate biquadratic finite element formulation. His analysis showed that spurious pressure modes associated with the inertia dominated flow were alleviated while the false numerical diffusion in the finite element equations was simultaneously minimized. This model is not applicable for highly separating flows which are typical for sapphire nozzle design.

The effect of small scale, high intensity inlet turbulence on flow through a subsonic two-dimensional diffuser with total included angles of 9^{o} and 20^{o} was studied experimentally by Hoffmann and Gonzalez (1984). They noticed symmetrical velocity profiles as compared to the transitory stall regime, where flow remained attached to one wall and detached from the other. Their results might be applicable to the flows which encounter adverse pressure gradients.

Durst et al. (1993) carried out both experiments and numerical analysis for the flow through a two-dimensional plane with a symmetric sudden expansion of area ratio 1:2. They observed a symmetry breaking bifurcation of the flow leading to one long and one short separation zone and with the increase of the Reynolds numbers the long

separated region increased whereas the short one remained approximately constant in length. Their study was confined to low Reynolds numbers 300 and 610 which was far away from turbulent flow field. In earlier papers concerned with the flow downstream of a symmetric, plane sudden expansion, Durst et al. (1974), Smyth (1976) and Cherdron et al. (1977) had demonstrated the asymmetric nature of velocity distribution at Reynolds numbers above critical values which depend on the expansion and aspect ratios. This asymmetry was attributed due to the amplification of disturbances along the shear layers and the requirement, imposed by continuity, that the corresponding vortices shed and grow in an asymmetric manner. At this Reynolds number (~1000) the energy spectra showed discrete peaks with relative small energy at higher and lower frequencies.

A numerical approach was developed by Lai et al. (1991) to predict the flow characteristics inside three different nozzles. The authors showed that the incorporation of a pin or to a certain extent a center-body insert into a conical nozzle resulted in enhanced cavitation. However, the overall performance of the nozzles was not experimentally verified.

The review of numerical and experimental results related to the influence of variation in the geometry and input conditions of a variety of nozzles was presented by Edwards and Welsh (1978). The authors analyzed exponential and general nozzle shapes. They showed the straight tapered nozzle produced the highest initial velocity at the exit and also highest maximum internal pressure but it exerted lowest stagnation impulse since velocity decay was rapid. The exponential nozzles of shortest length produced the highest initial jet velocities, but they gave rise to the greatest pressures within the nozzle.

2.3 Comments on the Previous Studies

Although a substantial amount of data concerning the behavior of WJs and AWJs has been acquired, the available information is not sufficient to allow prediction of the optimal design of the nozzle and the optimal cutting strategy. The flow characteristics of jets such

as velocity, pressure and turbulent quantities mainly depend on the nozzle configurations and input conditions which have not been extensively investigated for machining process control. The numerical simulation of nozzle flow is an economical and efficient way to predict these flow characteristics. The experimental determination of jet characteristics will validate the data for practical application of WJ and AWJ machining processes. The development of a knowledge base for the nozzle design by integrating experimental and numerical results is the objective of this investigation.

CHAPTER 3

EXPERIMENTAL SETUP AND TEST PROCEDURE

The experimental investigation was concerned with the determination of velocity, force and structure of WJ and AWJ. The investigation was divided into three parts. The first experiment involved the LTA measurements of water and abrasive particle velocities along and across the jet. The second experiment was concerned with measurement of forces exerted by the jet on the workpiece. A piezoelectric force transducer was used during this study. The third experiment involved the qualitative investigation of jet structure and behaviors by high speed filming.

3.1 Experimental Facilities

The tests were carried out in the water jet machining laboratory of Mechanical and Industrial Engineering Department of the New Jersey Institute of Technology. The water jet cell was manufactured by Ingersoll Rand Co. It has a 5 axis robotics manipulator controlled with an Allen Bradley 8200R robot controller. The system consists of the units (Fig. 3.1) described below.

3.1.1 Water Preparation Unit

The major components of this unit are the booster pump, filters, water softener, prime mover, intensifier, accumulator, control and safety instrumentation. The major function of the unit is to feed continuously pure water pressurized to the required pressure. To ensure continuous flow into the high pressure cylinder, the booster pump supplies the water into the low pressure water circuit (1.25 MPa). The low pressure filters (1-10 microns) and the softener are used to remove the iron and calcium dissolved solids.

A hydraulic driven (10-40 hp) oil intensifier is used to develop pressure upto 345 MPa in the water from the booster pump. There are two separate circuits for oil and water. The oil circuit is a close circuit and the water circuit is an open one. The oil pressure of about 20 MPa developed by the rotary pump is used to drive the intensifier. The intensifier is a double acting reciprocating type pump, of 152.4 mm diameter. It is operated every few seconds by an adjustable controller.

The high pressure water from both sides of the intensifier is discharged to an accumulator where the pressure is stabilized. Since the water at 345 MPa is 12 percent compressed, the water is not discharged uniformly from the intensifier at all piston positions. Hence, the accumulator is used to maintain the uniform flow.

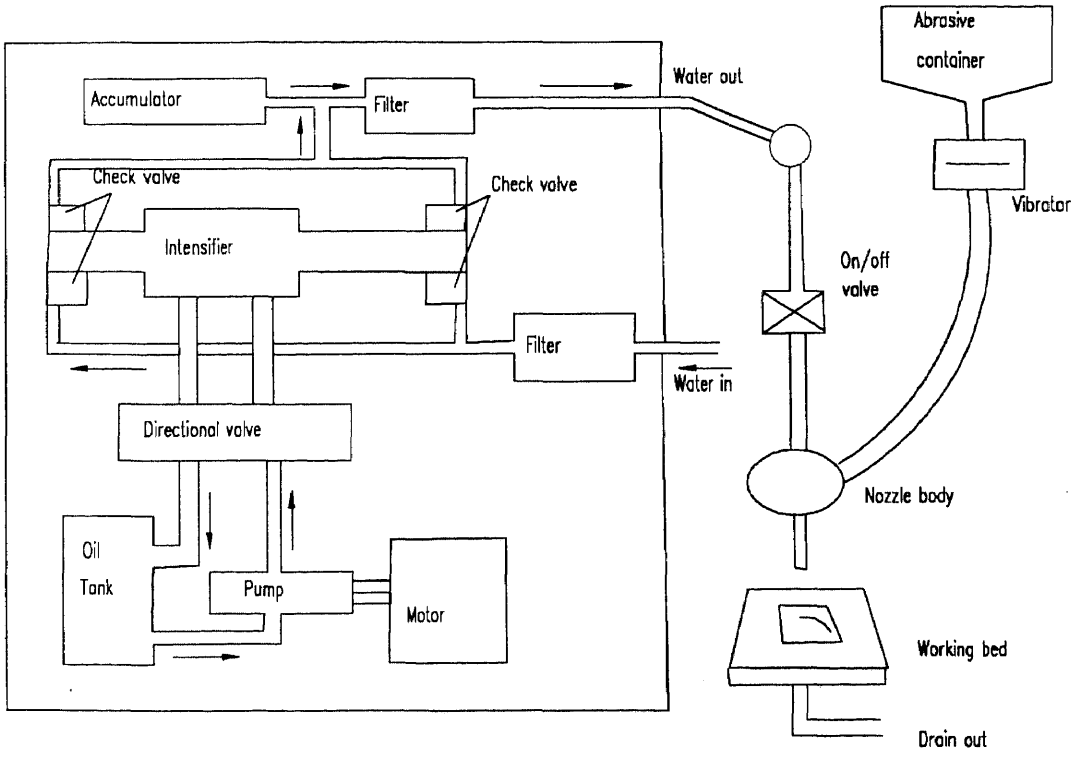

Figure 3.1 Schematic of AWJ Machining System

The high pressure water output of the accumulator is conveyed to the work station through a series of pipes, swivels, flexible joints and fittings. The line pressure drop is determined by summing up pressure drops in all joints, elbows and the pipe.

3.1.2 Work Cell

This is the place where the actual experiment was performed. It consists of a nozzle body, an abrasive feeder, traversing mechanism and a catcher.

The pressure head of water is converted into kinetic energy in the nozzle assembly. There are two nozzle bodies; -one for sapphire nozzles and another for sapphire-carbide nozzles generating WJ and AWJ respectively (Fig. 3.2). The high pressure water supplied from the water distribution line passes through the sapphire nozzle and accelerates to a higher velocity. In the case of AWJ, abrasive is feed via a side port into the water stream exiting from the sapphire nozzle. Thus, water and abrasive are well mixed in the carbide nozzle made of tungsten carbide where abrasive particles are accelerated and the momentum transformation takes place.

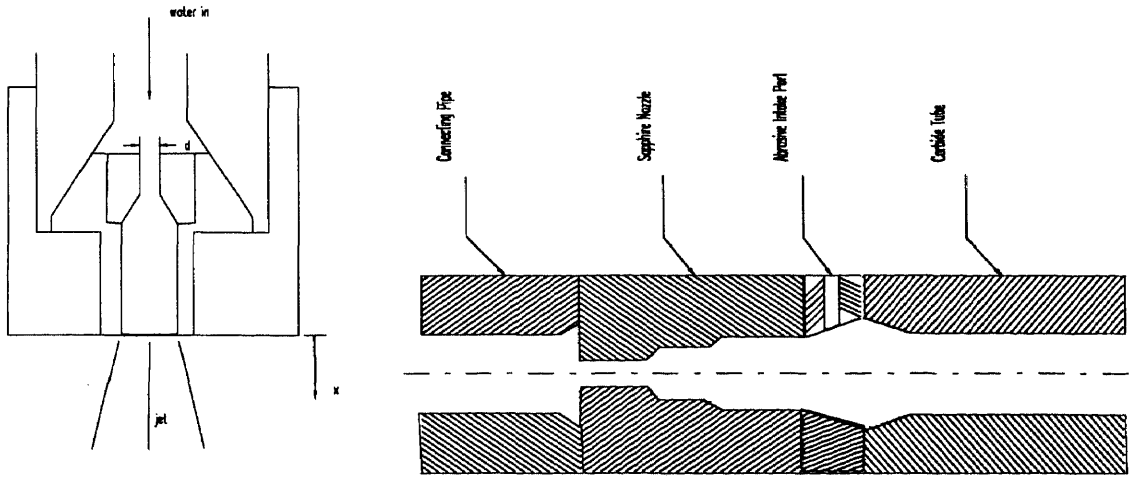

(a) (b)

Figure 3.2 Schematics of (a) WJ and (b) AWJ Nozzles

The abrasive feeder ensures continuous delivery of abrasive into the nozzle body at a controlled rate. The bulk abrasive is stored in a hopper whose exit is located on an electronically controlled vibrating tray. Through the control of the amplitude of vibration, the tray meters the flow of abrasive to a catch hopper. It is then aspirated through a short section of a flexible tube into the mixing chamber of the nozzle body.

An open tank type catcher is used to store the ejected high energy jet which contains particles of used abrasive, cut materials, water and debris. A drain near the base of the catcher tank allows water and abrasive flow into a settlement tank where the water drains out and the abrasive grit settles down. Noise reduction can be achieved by covering the cutting cell with a sound proof material such as Styrofoam.

There is a computer to load a NC program to control water and abrasive flow as well as robot movement about 5 degrees of freedom. The standard G, F and M codes are used to write the program. The technical data of the robot related to the experiment is listed in Table 3.1.

Table 3.1 Technical Data of the Robot

Position accuracy	+/- 0.005 inches
Repeatability	+/-0.005 inches
Controller resolution	0.0007 inches
Working range of rotary axes	A: 200 degrees, B: 360 Degrees

3.2 Measuring Instrument

3.2.1 Laser Transit Anemometer

The laser transit anemometer (LTA) is an nonintrosive velocity measurement device (Fig. 3.3). Particles entrained in the flow provide scattering centers for the incident light. The technique for encoding the measurement region uses two closely spaced spots, where the flow velocity component parallel to the axis connecting the spots is obtained from the

time-of-flight of the particles traversing the two spots. A Dantec made LTA was used to conduct the experiment for velocity investigation. It consists of He-Ne laser source, optics for measuring volume and signal processing counter.

The light source is a 15mw He-Ne laser to focus the flow field. There are two polarizers which make it possible to rotate the internal parts of the system i.e. the beam plane, and so the direction of the measurement can also be rotated. Both beams are focused by the lens system to form a measuring volume. The focal length is 600 mm and the two spots are separated by 449 μm. The image of the two points is received by the same lens system, and transmitted, via the mirrors, to the beam splitter which combines the two images. The back-scattered light from the particles is detected by the photo multiplier which converted the signal to voltage in the counter.

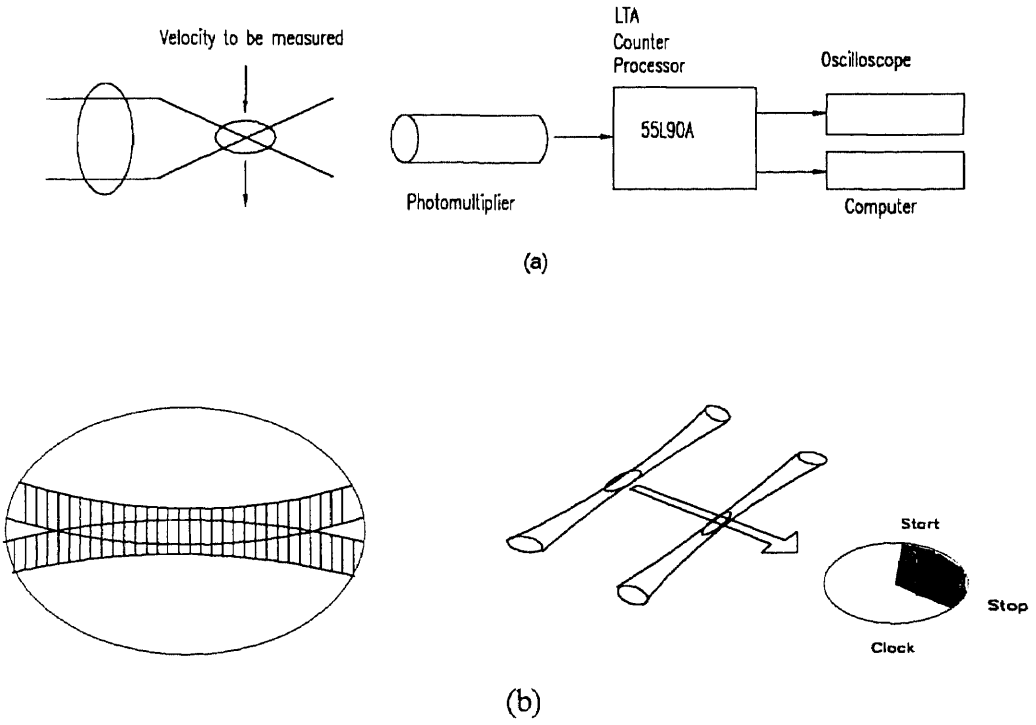

Figure 3.3 (a) The LTA System (b) The Measuring Volume & Counter's Clock Operation

The 55L90A counter is used as a signal processor for the LTA. The counter determines the velocity in the chosen direction by inverting the cross-correlated transit times for the particles passing through the two spots. The calibration factor is selected from the 55L90A instruction manual which depends on the range of jet velocity.

3.2.2 Piezoelectric Force Transducer

A Kistler made piezoelectric force transducer is used to measure the momentum distribution along the axis of the jet. The principle applied here is electric polarization produced upon the application of mechanical strain to piezoelectric materials. This relative value of polarization is proportional to the strain. This phenomena is known as direct piezoelectric effect. The piezoelectricity of a crystal is determined by its longitudinal, transverse and shear effects. These three effects are distinguished according to the position of the quartz crystal axes in relation to the force sustained.

Two identical, Kistler, three-component force measurement, platforms 9257A are used in this investigation. Each multi-component transducer is assembled from stacked quartz disks, loaded mechanically in series with electrode interlayers. The force to be measured acts on the work-piece so that each quartz disk produces the same amount of charge in the same direction at the same time.

A Kistler three-component charge amplifier, model 5007, is used as an electrometer to enable the charge alteration at the quartz transducers to be measured. The measuring range scale and sensitivity switch of each component of the charge amplifier are adjusted to suit the experiment being conducted.

A steel plate of 356X102X19 mm^3 is used as a work-piece. It contains 20 holes each of diameter 0.953 mm. This plate is attached to the insulation wood and transducers by means of screw. The bottom surface of the work-piece is fine machined to prevent possible vibration of the work-piece and the insulation wood.

3.2.3 High Speed Camera

A photec 16 mm rotating prism camera with a speed of 8,000 frames/sec is used with a copper-vapor laser beam to film the jet. The exposure time is 30 nano seconds. A ground mirror is used for illumination.

3.2.4 Matrix Video Matrix Econoscope

A matrix video matrix econoscope uses a non-contact technique to provide 3D video inspection system for dimensional verification of complete parts. It is used to measure the piercing diameter of the work-piece in order to analyze the jet core diameter. The positioning accuracy is 0.1 micron.

3.2.5 Read-Out Devices

To measure the voltage output and signal for the LTA and the piezoelectric force transducer, the following read-out devices are used.

A Fluke model 8101A digital multimeter is connected in parallel to the charge amplifier to record the voltage signals.

A Nicolct 2-channel oscilloscope is used to freeze the voltage signals generated during LTA and force transducer experiments.

3.3 Experimental Procedures

In this investigation, velocities and forces were measured for different conditions of jet formation. High speed filming of the jet and piercing of aluminum plate were also performed. The developed techniques for these investigations are described below.

3.3.1 Alignment of the Nozzle Body

Before starting the experiment, alignment of the sapphire and carbide nozzles were checked as described below.

A new sapphire nozzle was placed in the nozzle body. By turning on the intensifier at low pressure, 25-35 MPa, the coherence of the jet was observed visually and controlled by set screws, which determined the position of carbide nozzle axis. If the coherence of the jet was not found acceptable, the above procedure was repeated for new set of sapphire and carbide nozzles. Once a nozzle was aligned perfectly, the experiments were conducted by setting the intensifier to run continuously at the high pressure 345 MPa.

3.3.2 Calibration of the Abrasive Flow Rate

The garnet sands manufactured by the Barton Company have been employed as the abrasive particles in this study. In order to get an accurate abrasive flow rate for the experiments, the abrasive particles accumulated on the tray are flowed out and replaced with the new particles of the expected flow rate. The calibration of abrasive flow rate was then conducted by collecting and weighing the abrasive particles flowed out in one minute. The properties and size distribution of the abrasive particle are listed in Table 3.2.

Table 3.2 Properties and Size Distribution of Abrasive Particle

Abrasive Material (#50 HP): Garnet, Density: 3.9-4.0 g/cm^3, Hardness: 800-1000 HV		
Abrasive Size Distribution		
Tyler Mesh Size (#)	Sieve Opening (microns)	Percent Retained (%)
28	600	0.6
32	500	0.8
35	425	4.3
42	355	21.8
48	300	41.2
60	250	26.7
65	212	4.1

3.3.3 Velocity Measurement

Water and abrasive particles velocities were measured by the use of LTA. Both axial and transversal jet velocities were measured. The experimental matrix for this investigation is given in Table 3.3.

Table 3.3 Experiment Matrix for Velocity and Force Measurement (#50 HP garnet with flow rate 76 g/min used for AWJ)

Measurement Type	Sapphire Nozzle Diameter, d (mm)	Sapphire-Carbide Nozzles Diameters, d/D (mm)	Stand off distances, x (mm)
Axial velocities & Forces of WJs	0.178, 0.254, 0.305	-	0.127, 3.81, 6.35, 12.7, 25.4, 38.1, 50.8, 63.5, 76.2, 88.9, 101.6, 114.3
Axial Velocities & Forces of WJs & AWJs	-	0.178/0.762, 0.178/1.092, 0.178/1.600, 0.254/1.600, 0.305/1.600, 0.254/0.762, 0.305/0.762	0.127, 3.81, 6.35, 12.7, 25.4, 38.1
WJ Velocities Across Jet. Step in radial direction: 0.128 mm	0.178, 0.254	-	0.127, 6.35, 25.4, 50.8, 76.2, 127.0, 177.8
WJ & AWJ Velocities Across Jet. Step in radial direction: 0.128 mm	-	0.178/1.600	0.127, 25.4, 50.8, 76.2, 127.0, 177.8

LTA velocity measurement is very sensitive to its alignment with jet and measuring volume. For initial setup, a rotating wheel pinned radially with a thin wire at its perimeter was focused with LTA. At a motor speed of 1000 rpm and focusing the pin at a radius of 152 mm, the stored data in LTA was 16±0.6 m/s which had uncertainties only ±1% of actual velocity. Before carrying out actual measurement, LTA was further calibrated with

low pressure jet. To accomplish this, first the foci of the two concentrated beam were focused on low pressure jet, and a 10X magnifying glass was placed behind the jet in order to observe the location of the laser beam and the jet (Fig. 3.4). Using robot controller, the jet was aligned right at the center with two parallel laser beams. Then at a given pressure and velocity, LTA results were compared with the known velocity and found uncertainties about 2% which was acceptable to carry out velocities measurement at high pressure.

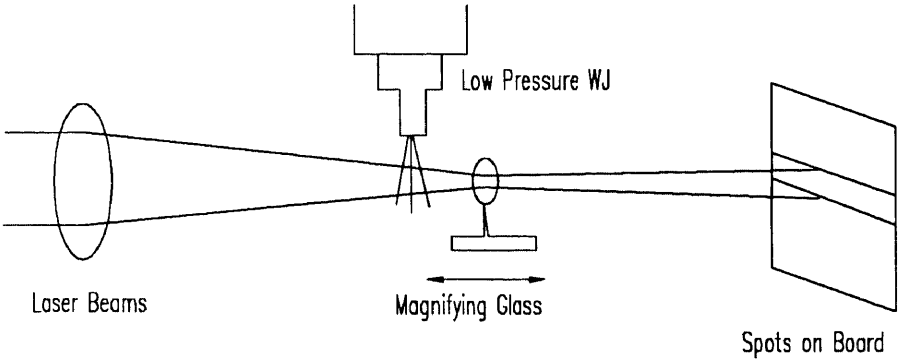

Figure 3.4 Checking of Jet Alignment with LTA Focusing Spots

Once the jet was perfectly aligned with low pressure jet as described above, the LTA was then connected with the signal processing counter, the main computer and oscilloscope. A NC program was loaded into the WJ machine for water flow at a pressure 334.6 MPa for 2000 sec without robot movement. In the counter, the maximum time was first selected high enough to allow particles at the lowest expected velocities to be accepted. By selecting the maximum time as short as possible, the counter could better reject most of the false events caused by different particles during starting and stopping. The low-pass frequency was reduced until a pulse height reduction and pulse broadening was observed. The high-pass was increased until an overshot of 30-60% was obtained. This overshot made the actual start/stop time less sensitive to pulse height variations and noise. Voltage gain was controlled in such a way as to subsidize noise level and to obtain

two distinct peaks in the oscilloscope connected with the counter. When two peaks were above 150 mv and all other peaks were below ±50 mv, oscilloscope was then receiving a satisfactory signal. This signal was stored and an instantaneous picture was taken using a Polaroid camera. At this moment about 200 data points were recorded from the counter. Later these data points were analyzed statistically to determine the average centerline velocity at that location. At each station three sets of readings were taken to get the mean value with sufficient accuracy. Using the robot controller, nozzle was moved to the next station and the experiment was performed exactly the same way as mentioned above.

For abrasive velocity measurement, the voltage in the counter was very carefully adjusted so the intensity of the back-scattered light could be distinguished in the LTA. By discriminating the weaker intensity of scattered light due to sub micron particles of water, it was possible to store the stronger signal from multimicron abrasive particles in the counter. The noise level was maintained ± 50 mv on the oscilloscope.

The velocity distribution across jet was measured for a single combination of sapphire-carbide nozzle with one kind of abrasive particle with constant flow rate. First two parallel beams of laser light were focused at the center of the jet, and then the jet was moved towards the left by an increment of 0.127 mm. At each position, the velocity was measured in a similar way as discussed above. The left-ward movement of jet and velocity measurement continued until the noise level ± 50 mv and no random velocity responses occurred.

3.3.4 Force Measurement

The piezoelectric force transducer was used to measure the forces exerted on a workpiece by the water and abrasive particles. Two transducers were installed on a flat surface. The work-piece was post-machined flat and fixed on the top of surface of the transducers. Between work-piece and the transducers, a thin wooden plate was placed as insulation, in order to reduce the signal disturbance of the transducers caused by thermal effects. Both

work-piece and the wood plate were fixed on the transducer surfaces by screws. The outputs of the transducers were connected to the charge amplifier where the signal was converted into voltages proportional to the forces acting on the work-piece. The charge amplifier was then connected parallel to the read out devices- multimeter and oscilloscope. The outputs were used to verify both readings.

Prior to the actual measurement, calibration of the transducers was done within the range of the test coordinates (x,y). The experiments were performed for the same test matrices (Table 3.3) used for velocity measurement with LTA. At first the jet was aligned with nozzle body as discussed in article 3.3.3. During the experiments the nozzle was held vertical so that the jet became normal to the work-piece. The time constant switch was set to 'long' which permitted the high frequency of the jet. The signal was stored in the oscilloscope and the voltage was calculated from the sign change of the signal due to 3 seconds duration of jet. The equivalent force was then determined from the amplifier's multification factor. After each individual measurement, the amplifier was reset. The experiments were repeated in the same location three times in order to obtain the mean value. The experimental setup for force measurement is shown in Fig. 3.5.

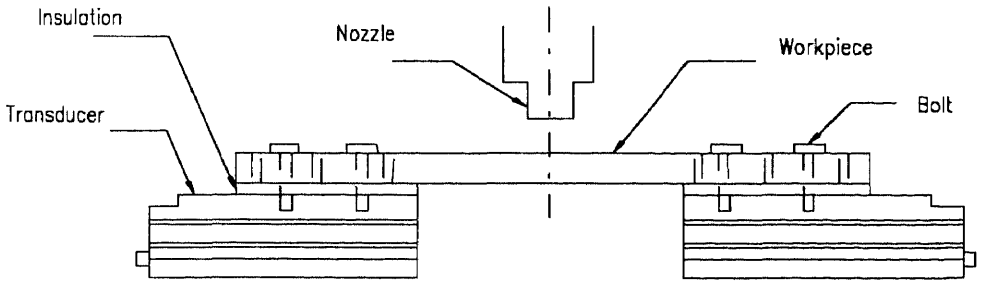

Figure 3.5 Schematic of Piezoelectric Force Transducer

3.3.5 Measurement of Mean Velocity of WJ

In this experiment, the aluminum plate was drilled by an impinging jet to create holes for conditions similar to those used in Table 3.3. An aluminum plate of 455X305X2 mm^3 was installed horizontally on the grate of the WJ machine using a spirit level. The piercing was performed for 10, 20, 30 and 40 seconds duration. It was found that piercing diameters for 30 and 40 seconds were almost the same which allowed carrying out the experiments for 30 seconds duration. The experiments were repeated three times for each location. The area of the effective jet spreading was then measured by determining the piercing area of the aluminum plate using the Matrix Econo Video Matrix. Using this knowledge of the jet area and stagnation pressure at different stand off distances, the mean velocity of jet was then determined by using the following equation.

$$F = PA = (\frac{1}{2}\rho U^2)(\frac{\pi}{4}d^2) \tag{3.1}$$

where F, ρ and d are force, water density and jet diameter respectively.

3.3.6 High Speed Filming

A photec high speed camera (8,000 frames/sec), with a 16 mm rotating prism was used for filming 20 different conditions of jet formations (Table 3.4) at the nozzle exit. The camera was placed 710 mm away from the jet axis (Fig. 3.6). The laser source and the ground mirror were placed in line to illuminate the jet. A copper-vapor laser beam of 50 mm diameter was used. The spot of 6.5 mm was focused on the nozzle and 43.5 mm on the jet. The exposure time was 30 nano seconds.

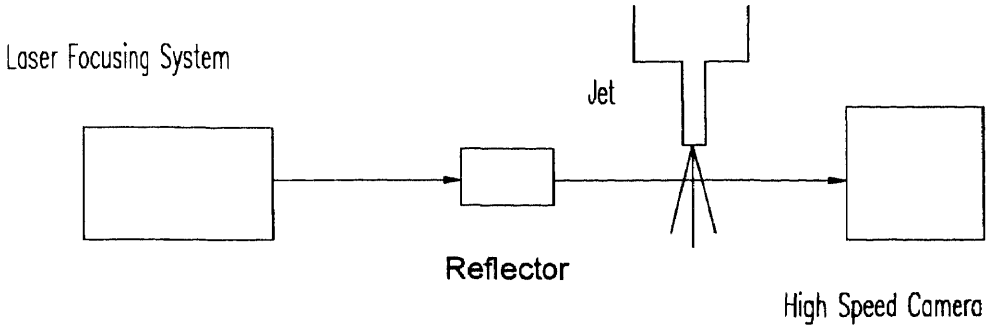

Figure 3.6 The Block Diagram of High Speed Filming

Table 3.4 Experiment Matrix for High Speed Filming

Filming No.	Abrasive Size HP #	Nozzle Diameters (mm) Sapphire, d	Carbide, D	Abrasive Flow Rate, g/min
1	-	0.127	-	-
2	-	0.178	-	-
3	-	0.254	-	-
4	-	0.356	-	-
5-7	-	0.254	0.762	-
8	-	0.254	2.362	-
9	50	0.254	0.762	540.8
10	50	0.254	0.762	540.8
11	50	0.254	2.362	540.8
12	80	0.254	0.762	102.5
13-15	80	0.254	0.762	299.3
16-17	80	0.254	0.762	370.0
18	220	0.254	0.762	191.5
19	220	0.254	0.762	318.5
20	220	0.254	2.362	318.5

CHAPTER 4

NUMERICAL SIMULATION OF TURBULENT FLOW INSIDE NOZZLE

Turbulent fluid motion is an irregular flow in which the various quantities show a random variation with respect of time and space coordinates, so only statistically distinct average values can be observed. Fully developed turbulent motion is characterized by a large number of three-dimensional entangled eddies or vortex elements of varying size. It therefore involves a wide spectrum of length and time scales. The largest eddies are produced as a result of hydrodynamic instabilities in the mean flow field which extract kinetic energy from the flow. The exact detailed spatial and temporal evolution of a turbulent flow can never be replicated since turbulence is a stochastic phenomenon.

4.1 Equations of Turbulent Flow

Turbulent flow is thought of being composed of mean and fluctuating parts such as

$$\tilde{\phi} = \overline{\phi} + \phi' \tag{4.1}$$

where ϕ is generic flow variable and instantaneous quantity is the sum of mean and fluctuating quantities. The mean quantity is obtained by applying time or ensemble averaging. Time averaging is

$$\overline{\phi} = \frac{1}{T}\int_{t}^{t+T} \tilde{\phi} dt \tag{4.2}$$

Turbulent kinetic energy is defined by

$$k = \frac{\overline{u'^2} + \overline{v'^2} + \overline{w'^2}}{2} \tag{4.3}$$

The rate of viscous dissipation of turbulent kinetic energy is also defined as

$$\varepsilon = \frac{\mu}{\rho}\overline{\frac{\partial u_i'}{\partial x_j}\frac{\partial u_i'}{\partial x_j}} \tag{4.4}$$

By time averaging of the instantaneous flow equations, the following governing equations

Continuity:

$$\frac{\partial u_i}{\partial x_i} = 0 \tag{4.5}$$

Momentum:

$$\rho\left[\frac{\partial u_i}{\partial t} + u_j\frac{\partial u_i}{\partial x_j}\right] = -\frac{\partial p}{\partial x_i} + \rho f_i - \rho g_i\beta_\theta(\theta-\theta_0) - \rho g_i\beta_c(c-c_0) + \frac{\partial}{\partial x_j}\left[\mu\left(\frac{\partial u_i}{\partial x_j}+\frac{\partial u_j}{\partial x_i}\right) - \rho\overline{u_i'u_j'}\right] \tag{4.6}$$

In the above equations, u_i, p, θ and c are components of mean velocity vector, mean pressure, mean temperature and mean specie concentration respectively. The energy and specie equations are not shown here since the flow studied in this investigation is isothermal, incompressible and chemically homogeneous flow. The terms $\overline{u_i'u_j'}$, are statistical correlation govern the effects of turbulence on the mean flow process. These unknown correlations appear as a result of the non-linear advection terms in the momentum equations. The second moment correlation $\rho\overline{u_i'u_j'}$, is a second order symmetric tensor which is an additional stress term in the momentum equation conventionally known as the Reynolds stress tensor.

Reynolds Stress is determined by the equation

$$\rho\overline{u_i'u_j'} = \rho\begin{bmatrix} \overline{u'^2} & \overline{u'v'} & \overline{u'w'} \\ \overline{v'u'} & \overline{v'^2} & \overline{v'w'} \\ \overline{w'u'} & \overline{w'v'} & \overline{w'^2} \end{bmatrix} \tag{4.7}$$

Here the diagonal terms are the variance of the fluctuating components of normal stresses whereas the off-diagonal terms are covariance of shear stresses in the fluid.

4.2 Turbulence Modeling

Turbulence modeling requires additional equations which determine the temporal and spatial evolution of the turbulent fluxes $\overline{u_i'u_j'}$,. Thus once a turbulence model has been proposed, it can be solved simultaneously with the mean flow equations to produce a solution to the mean flow field. Based on eddy viscosity concept several models ranging from zero equation to two equation model (k-ε) were suggested (Launder et al., 1984 and Nallasamy, 1985). Boussinesq eddy viscosity/difussivity concept assumes turbulent fluxes:

$$-\rho\overline{u_i'u_j'} = \mu_t\left[\frac{\partial u_i}{\partial x_j} + \frac{\partial u_j}{\partial x_i}\right] - \frac{2}{3}\rho k\delta_{i,j} \tag{4.8}$$

Where, the eddy viscosity, μ_t typically varies significantly within the flow field and from one flow to another. For the purpose of modeling, it is assumed that

$$\mu_t \propto \rho u_l \delta_l \tag{4.9}$$

Depending upon the partial differential equations that are employed to describe u_l and δ_l the following models have been proposed.

- Zero-equation models
- One-equation models

- Two-equation models

Zero-equation models involve only algebraic expressions for determining u_l and δ_l whereas one and two equation models entail, respectively, the solution of one and two extra partial differential transport equations.

Two equations model has been applied in this simulation. In k-ε turbulence model, the characteristics turbulent velocity and length scales are expressed as follows:

$$u_l \infty k^{1/2} \tag{4.10}$$

$$\delta_l \infty \frac{k^{3/2}}{\varepsilon} \tag{4.11}$$

Substituting the above equations (4.10 and 4.11) in Boussinesq's eddy viscosity equation (4.9) yields the Kolmogorov-Prandtl equation:

$$\mu_t = c_\mu \rho \frac{k^2}{\varepsilon} \tag{4.12}$$

The values of k and ε are obtained from the following semi-empirical transport equations (Launder and Spalding 1972):

$$\rho \frac{Dk}{Dt} = \frac{\partial}{\partial x_j}\left[\frac{\mu_t}{\sigma_k}\frac{\partial k}{\partial x_j}\right] + \rho G + \rho B - \rho\varepsilon \tag{4.13}$$

$$\rho \frac{D\varepsilon}{Dt} = \frac{\partial}{\partial x_j}\left[\frac{\mu_t}{\sigma_\varepsilon}\frac{\partial \varepsilon}{\partial x_j}\right] + c_1 \rho \frac{\varepsilon}{k} G + c_1 (1 - c_3) \rho \frac{\varepsilon}{k} B - c_2 \rho \frac{\varepsilon^2}{k} \tag{4.14}$$

In the k equation, G is the shear generation term which represents the production of turbulent kinetic energy resulting from the interaction between the mean flow patterns and

the turbulence field, and B is the buoyancy generation/destruction term resulting from the fluctuating temperature and spices concentration fields. In k-ε turbulence model these terms are:

$$\rho G = \mu_t \left[\frac{\partial u_i}{\partial x_j} + \frac{\partial u_j}{\partial x_i} \right] \frac{\partial u_i}{\partial x_j} \tag{4.15}$$

$$\rho B = \beta_\theta \frac{\mu_t}{\sigma_t} \frac{\partial \theta}{\partial x_i} g_i + \beta_c \frac{\mu_t}{s_t} \frac{\partial c}{\partial x_i} g_i \tag{4.16}$$

In contrast to the k equation, modeling of the source/sink terms of ε is not based strongly on the corresponding terms of the exact ε equation. The terms $c_1(\varepsilon/k)\rho G$ and $c_2\rho(\varepsilon^2/k)$ represent respectively, the shear generation and viscous dissipation processes of ε, and c_1 and c_2 are empirical constants. The solution of equations (4.13 and 4.14) gives, in effect, the temporal and spatial evolution of the characteristic turbulent velocity and length scales. Since these variables are governed by mean advection and diffusion, by the local processes of turbulent generation and destruction, the value of μ_t is obtained from the viscosity equation is considerably more representative of the local state of turbulence at a point than that obtained from zero- or one-equation models.

4.3 Finite Element Formulation

The purpose of the finite element method is to reduce the description of a continuum system to a discrete problem described by a system of algebraic equations. The method requires division of the continuum region of interest into a number of simple shaped regions called elements. The dependent variables u_i, p, k and ε are interpolated by functions of compatible order in terms of values to be determined at a set of nodal points. For this purpose, an individual element is separated from the assembled system in order to

develop the equations for these nodal points unknown. Within each element, the velocity, pressure, kinetic energy and dissipation fields separated by,

$$\begin{aligned} u_i(x,t) &= \varphi^T U_i(t) \\ p(x,t) &= \psi^T P(t) \\ k(x,t) &= \varphi^T K \\ \varepsilon(x,t) &= \varphi^T E \end{aligned} \tag{4.17}$$

where U_i, P, K and E are column vectors of element nodal point unknowns and φ and ψ are column vectors of the interpolation functions. Herein same basis function is used for all components of velocity and kinetic energy and dissipation in order to make the solution cost effective. Typically, the application of the Galerkin finite element procedure to the governing flow equations when an implicit time integrator is employed, results in a set of nonlinear algebraic equations that may be expressed in matrix form as

$$K(X)X = F \tag{4.18}$$

where K is the global system matrix, X is the global vector of unknowns and F is a vector which includes the effects of body forces and boundary conditions.

4.3.1 Elements

The choice of finite element is an important condition of a representative converge solution. The fluid element is categorized by the combination of velocity-pressure approximation. It has been used 4 node quadrilateral two dimensional elements in this investigation. The shape function is expressed in terms of normalized or natural coordinates, r and s, which vary from -1 to +1. In 4 node quadrilateral element, the velocity components are approximated using bilinear interpolation functions.

$$\varphi = \begin{bmatrix} \frac{1}{4}(1-r)(1-s) \\ \frac{1}{4}(1+r)(1-s) \\ \frac{1}{4}(1+r)(1+s) \\ \frac{1}{4}(1-r)(1+s) \end{bmatrix} \tag{4.19}$$

Two forms of the pressure discretization are possible with this element: a bilinear continuous approximation with the pressure degrees of freedom located at the four corner nodes, or a piece wise constant discontinuous pressure approximation where pressure degrees of freedom located at the centroid of the element.

4.4 Near-Wall Modeling with k-ε Model

In wall-bound turbulent flows the so-called near-wall regions are of crucial importance, since they act as bridges across which momentum, heat and mass are exchanged between solid wall and the fully turbulent flow regions in the main body of the flow. In this model, the variation of the turbulence viscosity within the viscous layer is typically described by Van Driest's mixing length model with a transition to the standard high Reynolds-number variant of the k-ε turbulence model in the regions beyond the viscous sublayer where flow is fully turbulent. In FIDAP package, a one-element thick layer of special elements is employed in the near-wall region between the fully turbulent outer flow field and the physical boundary. In these special near-wall elements, specialized shape functions are used to accurately capture the sharp variations of the mean flow variables in the viscosity affected near-wall region.

The special elements (2 nodes in the y-direction) shape functions are defined as

$$\varphi_1(y) = 1 - A(y) \tag{4.20}$$

$$\varphi_2(y) = A(y) \tag{4.21}$$

where $A(y)$ is the expression based on the universal profiles. For velocity interpolation,

$$A(y) = A_1 / A_2 \tag{4.22}$$

$$A_1(y) = (1/\kappa)\ln[1 + 0.2\Delta_u^+(1+y)] + 7.8[1 - \exp(-\Delta_u^+(1+y)/22) - \Delta_u^+(1+y)\exp(-0.165\Delta_u^+(1+y)/22)] \tag{4.23}$$

$$A_2 = A_1(n=1) \tag{4.24}$$

where Δ_u^+ is dimensionless characteristic height of the element in the y-direction, defined by

$$\Delta_u^+ = \rho(c_\mu^{1/2}k)^{1/2}\Delta/\mu \tag{4.25}$$

where Δ is the actual height of the element above the wall and k, the turbulent kinetic energy at the top of the element i.e., y=1. Δ_u^+ is sometimes called characteristic element Reynolds number. A larger number represents a thinner viscous sublayer.

The Van Driest Mixing length approach is also used here in the form,

$$\mu_t = \rho l_m^2 [(\frac{\partial u_i}{\partial x_j} + \frac{\partial u_j}{\partial x_i})\frac{\partial u_i}{\partial x_j}]^{1/2} \tag{4.26}$$

where l_m, the mixing length is defined by

$$l_m = \kappa y[1 - \exp(-y_u^+ / A)] \tag{4.27}$$

In the above equation the dimensionless distance from the wall is defined as

$$y_u^+ = \rho(c_\mu^{1/2}k)^{1/2} y/\mu \tag{4.28}$$

where y_u^+= dimensionless distance from the wall, κ=0.41, the Von Karman constant and A=26, is an empirical coefficient.

In FIDAP's scheme, the computational domain for the mean flow equations encompasses the entire flow domain down to the solid boundary whereas the corresponding computation for the k and ε equations of the k-ε turbulence model only extends to the top of the special near-wall elements. The appropriate boundary conditions are applied for k and ε in near-wall methodology which are

$$\frac{\partial k}{\partial y} = 0 \tag{4.29}$$

and

$$\varepsilon = (c_{\mu}^{1/2} k)^{3/2} / \kappa y \tag{4.30}$$

These indicate the equilibrium turbulence conditions in the near-wall regions where k is a constant and the turbulence length scale, defined as $k^{3/2} / \varepsilon$, varies linearly with normal distance from the wall. The above Neuman boundary condition on k plays a pivotal role in the entire near-wall methodology. At the end of each iteration, the value of k is used to arrive at a characteristic turbulence velocity scale of near-wall region which determines the magnitudes of the local elemental Reynolds/Peclet numbers which in turn control the degree of skewing in the special basis functions for an accurate resolution of the local near-wall flow profiles. In order to use this method properly, it is required that viscous and transitional sublayers are fully contained within the special near-wall elements. Hence elemental Reynolds number Δ_u^+ in all special elements must not be significantly less than 30. If it is lower than 30 over significant portions of the computational boundary, then a further simulation must be attempted using a coarser grid in the direction normal to the wall.

4.5 Nozzle Flow Simulation Using k-ε Model

A set of nozzles used in experiments as well as some prudentially designed nozzles for improved coherence and mixing of the jets has been simulated using the k-ε turbulence model. The nozzles configurations and corresponding boundary conditions are listed in

Appendix A (Fig. A.1 and Tables A.1-A.6). As derived in Art. 4.1-4.2, the governing equations employed for two dimensional, incompressible, isothermal turbulent flow without body forces inside nozzle using k-ε turbulence model can be written as follows:

$$\rho u_j u_{i,j} = -p_{,j} + [\mu(u_{i,j} + u_{j,i}) - \rho\overline{u_i' u_j'}]_{,j} \tag{4.31}$$

$$u_{i,i} = 0 \tag{4.32}$$

$$\rho u_j k_{,j} = [\frac{\mu_t}{\sigma_k} k_{,j}]_{,j} + \mu_t (u_{i,j} + u_{j,i}) u_{i,j} \tag{4.33}$$

$$\rho u_j \varepsilon_{,j} = [\frac{\mu_t}{\sigma_\varepsilon} \varepsilon_{,j}]_{,j} + c_1 \frac{\varepsilon}{k} \mu_t (u_{i,j} + u_{j,i}) u_{i,j} - c_2 \rho \frac{\varepsilon^2}{k} \tag{4.34}$$

where $i, j = 1, 2$, $\mu = \mu_0 + \mu_t$ and $\mu_t = \rho c_\mu k^2 / \varepsilon$ as proposed by Kolmogorov-Prandtl.

The empirical constants used in the above equations (4.33 and 4.34) are chosen for axisymmetric confined turbulent flow which are c_μ =0.09, σ_k=1.00, σ_ε =1.30, c_1=1.44 and c_2=1.92 (Rodi 1980). Van Driest mixing length approach is used for the near wall to compute the turbulence viscosity as described in Art. 4.4.

The application of Galerkin finite element discretization to the governing equations results in a set of nonlinear algebraic equations which has the matrix form (Art. 4.3)

$$\boldsymbol{K(X)X=F} \tag{4.35}$$

where $\boldsymbol{K}$ is the global system matrix, $\boldsymbol{X}$ is the global unknown vectors and $\boldsymbol{F}$ is a vector of boundary conditions and body forces.

4.5.1 Boundary Conditions

It is required to provide appropriate boundary conditions for u, k and ε on the boundaries of the computational domain.

The inlet plane is positioned upstream of the regions of interest in an area where the flow field is unperturbed from any nearby obstacles. The boundary conditions for u is prescribed uniform at the inlet which is computed from the known flow rate. The turbulence quantities at the inlet section are empirically determined (FIDAP 1991) by the following equations.

$$k = 0.1u^2 \tag{4.36}$$

$$\varepsilon = k^{3/2} / 0.05r \tag{4.37}$$

The simulation is also performed with following expressions for k and ε as proposed by Launder and Spalding (1974) and found no significant difference of the results.

$$k = c_{\mu}^{1/2}[l_m \frac{du}{dy}]^2 \tag{4.38}$$

$$\varepsilon = c_{\mu} k^2 [l_m^2 \left|\frac{du}{dy}\right|]^{-1} \tag{4.39}$$

$$\frac{u}{u_r} = [\frac{y}{\delta}]^{1/n} \tag{4.40}$$

where, u is stream wise velocity component at the inlet plane, y is the normal coordinate axis to the nearest wall and n is Reynolds number dependent obtained from Schlicting (1979). The above profiles of k, ε and u are imposed as Dirichlet boundary conditions on the inlet boundary in FIDAP using the user-supplied subroutine.

At the outlet boundary, the Neumann i.e., the zero-gradient or zero flux boundary condition in the axial direction is applied for u, k and ε .

At the symmetry plane the gradients of all the variable are set to zero in the radial direction.

At the wall, the near-wall modeling methodology is applied along those portions of the computational boundary which coincide with the solid boundary. The boundary conditions for k and ε on thick element which contains the viscous and transitional sublayers are prescribed as follows.

$$\frac{\partial k}{\partial y} = 0 \tag{4.41}$$

$$\varepsilon = [c_{\mu}^{1/2} k]^{3/2} / \kappa y \tag{4.42}$$

On the solid wall u, k and ε are prescribed zero.

4.5.2 Initial Conditions

Non-zero initial guess for u, k and ε improves the convergence characteristic. In general the constant values of u, k and ε are used which have obtained from the above equations. For profiles, the intermediate values are used as the initial guess.

4.5.3 Solution Algorithm

A segregated implicit algorithm is employed for the numerical solution of the set of discretized equations resulted from the application of the Galerkin finite element method to the flow governing equations. In this approach, the global matrix system is never directly constructed. Instead, the discretized implicit equations associated with each primary flow variables are assembled in smaller sub-matrices. It uses mixed velocity-pressure formulation. At the beginning of an iteration, an approximation to the pressure is obtained from the solution of the Poison type pressure matrix using latest available values

of the field variables. The various components of the momentum equations and any other conservation equations present in the flow problem are then solved in a sequential manner using the most recent field variables. Finally, at the end of each iteration the velocity field is mass adjusted via an irrotational projection onto a divergence free sub-space. This last step involves the solution of a further Poisson type matrix equation for a pressure corresponding vector Δp.

The finite element package FIDAP 6.01 has been used for the numerical solution of the discretized equations. Two program listing are given in Appendix F.

4.5.4 Convergence Criteria

When this iterative method is applied to solve the equations, an appropriate criteria is used to terminate the iteration. Two obvious variables for use in the selection of termination criteria are solution vector u_i (at iteration i) and the residual vector $R(u_i)$. It is desired that the solution vector at the end of each iteration be within a certain tolerance, ε_u, of the true solution vector u, then, a convergence criterion, base on relative error, is defined as

$$\frac{\|\Delta u_i\|}{\|u\|} \leq \varepsilon_u \; ; \quad \Delta u_i = u_i - u \tag{4.43}$$

where $\|.\|$ is an appropriate norm. However, u is not known a priori and must be approximated, and the usual choice being $\|u_i\|$ for $\|u\|$ and u_{i-1} for u in $\Delta u_i = u_i - u_{i-1}$.

Another convergence criterion is also checked in this iterative solution which is based on the residual vector, tending to zero as u_i tends to u. This criterion requires

$$\frac{\|R(u_i)\|}{\|R_0\|} \leq \varepsilon_F \tag{4.44}$$

where R_0 is a reference vector, typically $R(u_0)$. Combination of these two criteria provides an effective overall convergence criterion for all possible solutions. In this simulation, the solution is taken as converged when sum of the normalized residuals fall below 0.001.

4.5.5 Solution Strategy

The implicit segregated algorithm used in numerical solution requires a relaxation (dumping) factor (0.5) for flow equations of mean velocities, k and ε. Mesh density of the computational domain are varied to produce grid independent solution. If there is spurious spatial oscillations in the flow variables due to the large grid Reynolds numbers then mesh density is adjusted accordingly to avoid the so-called "wiggles".

There are three main sources of instability that if left untreated will seriously plague typical k-ε simulations. These are non-realizable k and ε and highly unrealistic turbulence time and length scale.

The first of these instabilities is associated with the dissipation (or sink) term in the k and ε equations. During the course of the numerical solution, while the interim solution field is significantly different from the fully converged solution, the dissipation terms may strongly overweight the generation terms and can momentarily produce de stabilizing negative nodal values of k and ε. The source and sink terms will change polarity.

The second source of instability is associated with the advection terms in the k and ε equations. For large Reynolds number it produces the stream wise oscillations in the corresponding flow variables. If these oscillations are large compared to the local values of k and ε, negative nodal values of k and ε could therefore result.

The third source of instability ensues when k-ε model is used in the prediction of flows containing both turbulent and laminar regions. Since terms involved k and ε in equations are indeterminate in laminar flow regions, these ratios become ultra sensitive to noise level variations in k and ε and begin to oscillate violently from one nodal point to another.

In order to suppress these three kinds of instability, streamline upwinding and clipping are employed.

Streamline upwinding is a numerical technique which introduces stabilizing false numerical diffusion along the stream wise direction. The upwinding factors used for mean velocities are 1 and for k and ε are 5 respectively.

By clipping we can avoid first and third types of instability which ensures not falling below preassigned lower bound positive values. The lower bound values below which nodal values of k and ε are clipped are set by default to be fifty thousand times smaller than the maximum nodal values of k and ε.

Since streamline upwinding and clipping are the artificial stability enhancing measures which interface with the course of the numerical solution, the technique used in this computation is to obtain at first a stable solution with moderately large values of the upwinding factors, and then to cut back to the point where stream wise oscillations begin to appear in the solution.

CHAPTER 5

RESULTS AND DISCUSSIONS

In the investigation of jet formation, velocities and forces of WJ and AWJ were determined by experiments and qualitative behaviors of jets were visualized by high speed filming. A numerical prediction of turbulent water flow inside various nozzles was also performed to determine the effect of nozzle parameters on jet structure.

5.1 Accuracy of Measurement

5.1.1 Laser Transit Anemometer (LTA)

The accuracy of LTA measurement was first verified with the constant velocity of a rotating wheel as discussed in Art. 3.3.3. The variation was found only ±1.5% of actual velocity. The reading of LTA was also checked by computing velocity from independently recorded travel time of a particle in the oscilloscope. Again the variation of two velocities were in the range of 2%. The results are listed in Table 5.1.

Table 5.1 Accuracy of LTA Measurement

Wheel Velocity (m/s)	LTA Velocity (m/s)	LTA % Variation	Oscilloscope (m/s)	Oscilloscope % Variation
20.20	20.50	-1.48	19.98	1.089
30.50	31.00	-1.64	31.50	-3.28
105.80	107.20	-1.32	106.30	-0.47
232.70	235.40	-1.16	228.90	1.63
510.80	519.30	-1.66	505.80	0.98

5.1.2 Piezoelectric Force Transducer

The accuracy of piezoelectric force transducer measurement was checked by putting on known weights on its platform and recording the corresponding responses. The variation

of piezoelectric force and weight force is found in the range of 1.5%. The piezoelectric force was also verified by the voltage change of the signal stored in the oscilloscope. The variation is found only ±2%. The results are listed in Table 5.2.

Table 5.2 Accuracy of Piezoelectric Force Transducer Measurement

Weight Force (N)	Piezo. Trans. (N)	Piezo. Trans. % Variation	Oscilloscope (N)	Oscilloscope % Variation
5.20	5.12	1.53	5.07	2.50
10.13	9.97	1.58	10.01	1.18
15.40	14.98	2.72	15.10	1.95
20.63	21.05	-2.03	21.30	-3.24
30.30	31.10	-2.64	30.90	-1.98
40.50	41.10	-1.48	39.80	1.72

5.1.3 Numerical Simulation

In numerical simulation, the iteration was terminated when the convergence tolerance (Art. 4.5.4) had been less than 0.001. The higher tolerance 0.0001 changes the solution vector only 1% but increases the computational time significantly. The accuracy of the numerical solution of the governing equations (Art. 4.5) was also checked by increasing the number of elements in the solution domain. When elements independent solution reached, stability enhancing factor, upwinding, was tuned to the lower values until stream wise oscillations began to appear in the solution. A typical result for the nozzle NZ5.1 is listed in Table 5.3. It is found that the upwinding factor 2 gives stream wise oscillation.

Table 5.3 Accuracy of Numerical Simulation for Nozzle NZ5.1

No. of Elements	Solution Vector u (m/s)	Iteration reqd. for convgd. soln.	Upwinding Factor
6574	911.82	866	5
7210	913.56	1208	5
7210	914.09	1232	3
7210	957.30	1288	2

5.2 Experimental Results

The figures referred to the experimental results are given in Appendix B.

5.2.1 Velocity Investigation

LTA was used principally for investigation of the jet velocity. The validity of the measurement was checked by measuring the known velocity field of a low pressure jets. In Fig. B.1, a comparison is depicted with the velocity obtained from Bernoulli's equation. The LTA measured velocities follow Bernoulli's type of flow but there is a loss of energy which increases with the increase of the supply pressure. In Fig. B.2, a typical output of oscilloscope which was parallel connected with the LTA is shown. The velocities calculated from these oscillograms are approximately 770 m/s for sapphire WJ, 710 m/s for sapphire-carbide WJ and 420 m/s for AWJ. The velocities measured by LTA are compared with oscillograms output and the observed variation did not exceed ±2%. This also validates the experimental results. A typical velocity probability recorded in LTA measurement is shown in Fig. B.3. The velocity probability shifts to the left to a lower velocity with the increase of stand off distances. It also shows that the noise level is within the 2% which is in the acceptable range of experimental error. Figs. B.4 and B.5 depict the velocity probability of WJ and AWJ respectively for different nozzles. After carefully averaging, the WJ velocity was found in the range of 740- 790 m/s while AWJ velocity range was 350 - 470 m/s. The addition of abrasive in water flow stream drags the WJ velocity tremendously causing the reduction of the overall velocity. The AWJ velocity also depends on the abrasive feeding rate and corresponding size and specific weight of particles.

The velocity distributions for sapphire WJ, sapphire carbide WJ and AWJ along the axis of the jet are presented in Figs. B.6, B.7 and B.8. Velocity from sapphire nozzles do not change substantially within the chosen stand off distances. The effect of carbide nozzle on WJ is not significant as shown in Fig. B.7. The velocity decay for AWJ is much

faster than WJ because air drag causes the jet diffused and consequently reduces the flow kinetic energy. Fig. B.8 also shows that the bigger carbide tube produces higher exit velocity of AWJ. It indicates that the frictional loss to the kinetic energy is less in bigger carbide tube than the smaller carbide tube. The velocity distributions across the jet are presented in Figs. B.9, B.10 and B.11 for different stand off distances. The plots show that gaussian type of velocity distribution in the radial direction and also indicate the domain of the jet core. With this current LTA setup, it is not possible to measure velocity at the region remote from the centerline since the noise level is high and the probability of a single particle to pass through the two spots is very low.

5.2.2 Sapphire Area Effects on Exiting WJ Velocity

Various nozzles (Fig. B.12) are used to investigate the exiting jet. It is shown that the normal behaviors of the developed jets are similar to conventional turbulent jets (Abramovich, 1963). A smaller orifice provides higher centerline velocity. The axial velocities are found to be in the range of 700-800 m/s.

5.2.3 Force Investigation

The calibrations of piezoelectric force transducer about x and y directions are depicted in Fig. B.13. It is noticed that the measured forces in the test coordinates are fairly constant. The measured forces at various stand off distances are depicted in Figs. B.14, B.15 and B.16. It is found that increase of the sapphire nozzle diameter causes increase of forces. It is also noticed that addition of abrasive decreases the force in the selected experimental matrix. At the stand off distances below 8 mm the forces remain constant and then decrease at a slower rate.

5.2.4 Comparison of LTA Measured Velocity with the Mean Velocity from Stagnation Pressure

In Fig. B.17, the jet spreading with stand off distances is depicted. It indicates that the effective area of the jet which has higher kinetic energy. Using piezoelectric forces with stagnation pressures (equation 3.1) and the jet area obtained from Fig. B.17, the average axial velocity was computed. The result is shown in Fig. B.18. It is noticed that the velocity at the tip agrees well with the LTA measured velocity which validates the turbulent nature of the jet profile. In the down stream velocity decays very fast due to the diverging of the jet and probably area used in computation might be the total the area of the core, bubbles and mist.

5.2.5 Comparison of Velocities and Forces at the Exit of the Nozzles

The exit velocities and forces of sapphire WJ are listed in Table 5.4.

Table 5.4 Axis Velocity and Force for Sapphire WJ
(Stand off distance, x= 1 mm)

Type	d (mm) 0.102	d (mm) 0.127	d (mm) 0.178	d (mm) 0.254	d (mm) 0.305	d (mm) 0.356
u (m/s)	805	782	779	770	757	709
Av. u (m/s)	-	-	750	729	716	-
Force (N)	-	-	12.72	24.11	32.21	-

It is found that sapphire nozzle has a profound effect on both velocities and forces. The average velocities are close to the central line velocities which indicate the complete turbulent nature of the jets.

The exit velocities and forces of sapphire-carbide WJ and AWJ are listed in Table 5.5. The low velocity ratio (0.4-0.6) of abrasive to water indicates inefficient mixing process.

Table 5.5 Axis Velocity and Force for Sapphire-Carbide WJ and AWJ
(Stand off distance, x= 1 mm)

Measurement Type	d=0.178 mm D=0.762 mm	d=0.178 mm D=1.092 mm	d=0.178 mm D=1.600 mm
WJ u (m/s)	764	762	756
AWJ u_a (m/s)	431	459	497
WJ Force (N)	10.71	10.99	11.10
AWJ Force (N)	9.66	11.26	11.55

The carbide diameters do not have significant effect on velocities and forces. The addition of abrasive decreases forces due to the abrasive particles friction with carbide tube.

5.2.6 Results of High Speed Filming

The figures referred to the high speed filming are given in Appendix C. The visualization of WJ and AWJ were carried out by high speed filming. Figs. C.1 and C.2 show the structure of sapphire WJ. The core, mist, droplets and circulation vortex around the jet are well depicted in these photographs. The increase of the nozzle diameters results in increase of core diameters and pulsing nature of the jet as depicted in Fig. C.2. The sapphire-carbide WJ is shown in Fig. C.3. It depicts the behavior similar to that of sapphire WJ. The picture also shows the cavities around the core of the jet.

Figs. C.4-C.6 depict the AWJ behaviors. The effect of carbide tube diameters is shown in Figs. C.4a,b. The bigger the carbide tube diameters causes bigger pulse and core diameters. It also reveals the discontinuity of the AWJ. The effect of abrasive particle sizes is demonstrated in Figs. C.4c,d. The bigger particle size produces violent pulsing jet (Fig. C.4c).

In Fig. C.5, a sequential AWJ is shown where only variable is carbide tube diameter. Both jets show pulse, discontinuity and cavity formation. In Fig. C.6, a series of AWJs are shown by changing the abrasive particles. It shows the pulse and discontinuity of jets are quite random in nature.

5.3 Computational Results

Five typical nozzles named as NZ1, NZ2, NZ3, NZ4 and NZ5 (Appendix A, Fig. A.1) are used for computational analysis. Primarily the geometrical shapes are changed to investigate the fluid dynamics characteristics of the nozzle flow. The parameters and boundary conditions used for those nozzles are given in the Tables A.1-A.6 (Appendix A). Two typical programs are listed in Appendix F out of about thirty programs used in this numerical computation.

5.3.1 Results of Nozzle NZ1

The results of different sapphire nozzles with varying converging angles are shown in Figs. D.1-D.12 (Appendix D). Nozzle NZ1 is named as converging type nozzle. Various converging angles with different orifices has been simulated in this analysis.

5.3.1.a Effect of Converging Angles

The streamline, pressure and eddy viscosity contour plots for three different angles are depicted in Fig. D.1-D.3. It is noticed that flow is almost parallel and a little separation at the converging angle. The pressure contour plots show that the static pressure at the orifice entry is about 440 MPa. The maximum viscosity occurred at the boundary near the orifice exit.

The centerline velocities for different nozzles are plotted in Fig. D.4. It is found that the velocity reaches maximum just after the orifice. It also indicates that the friction of the inner surface of the orifice with flow causes reduction of centerline velocity. Again it shows that smaller diameter of the orifice provides highest velocity in the orifice. The different converging angles do not affect the flow substantially. The flow is completely developed within the distance of 4-6 times the orifice diameter.

The exit velocity distribution across flow is depicted in Fig. D.5. The velocity on the axis is in the range of 720-980 m/s. In Fig. D.5a, the 90^0 converging angle nozzle

shows maximum velocity at the exit since this nozzle has shorter orifice length which indicates less frictional loss. The 60^0 converging angle nozzle provides the higher velocity on the axis. For other angles velocity is about 820 m/s which is quite similar to our experimental results (780 m/s). The radial velocity (v) and turbulent kinetic energy (k) profiles at the nozzle exit are shown in Figs. D.6 and D.7. From velocity (v) plot, it follows that the tendency of flow separation in the orifice is insignificant. The turbulent kinetic energy plot indicates that the turbulent fluctuation increases in the radial direction.

5.3.1.b Effect of Orifice Diameters

The effect of orifice diameters on numerical simulation for flow in nozzle NZ1 are studied in this section by using constant converging angle 60^0. The angle is chosen on the basis of previous solutions and the nozzle geometry used in the experiments. The streamline, pressure and eddy viscosity contour plots are depicted in Fig. D.8. The flow pattern, pressure distribution and the viscosity level for all the cases are quite similar. Only changes are found in their numerical values. In Fig. D.9 the axial velocity distribution is demonstrated. It indicates that a larger the orifice corresponds to a smaller the maximum velocity. Fig. D.10 depicts the velocity distribution across flow at the nozzle exit. The velocity ranges from 700 to 950 m/s. The highest velocity is found for an orifice diameter of 0.127 mm (the smallest one in this analysis). The radial velocity (v) and turbulent kinetic energy profiles at the exit are shown in Figs. D.11 and D.12. The velocity (v) plot indicates that the flow like stream lined type. The kinetic energy increases in the radial direction but in a very slow rate which indicates that there is less velocity fluctuation at the exit of the nozzle.

5.3.2 Results of Nozzle NZ2

In Appendix D, Figs. D.13-D.19 are referred to the results of nozzle NZ2. Three different types of NZ2 has been investigated in computation. Basically NZ2 is similar to NZ1 type.

The only difference is the inlet of the orifice which entails two steps. The stream line (Fig. D.13) pattern is smooth and parallel but there is a minor separation at the corner of the step change. The pressure contours and turbulent viscosity are depicted in Figs. D.14 and D.15. The maximum pressure drop occurred across the orifice. The distribution pattern is quite similar with NZ1.

5.3.2.a Effect of Two Steps Converging and Orifice Length

Fig. D.16 shows the centerline axial velocity distribution. The maximum velocity is noticed after orifice is higher than NZ1. The spatial velocity distribution at nozzle exit is shown in Fig. D.17. The centerline velocity is about 1220 m/s and 1360 m/s for NZ2.1 and NZ2.2 respectively. The NZ2.3 is of longer orifice than NZ2.1 and axial velocity 850 m/s is much smaller than that of the nozzle NZ2.1. This indicates that the velocity decays beyond the jet development length. The velocity (v) and turbulent kinetic energy distributions at nozzle exit are shown in Figs. D.18 and D.19. Fig. D.18 shows that the tendency of velocity vector rotation is less in NZ2.2 in comparison with other two nozzles. It indicates that the converging nozzles with two converging steps (NZ2.2) are more efficient than steep change in terms of kinetic energy at the exit of the nozzle. The orifice length 4-6 times of orifice diameter shows complete development of the jet. Further increase of orifice length just decreases the axial velocity of the jet.

5.3.3 Results of Nozzle NZ3

In this simulation the effects of upstream nozzle shape and the diverging angle are discussed. The sapphire nozzle is connected to the pipe under different geometrical configurations. In Appendix E, Figs. E.1-E.6 depict the results of nozzle NZ3. The streamline, pressure and eddy viscosity contours are depicted in Figs. E.1-E.3. The stream line is separated in the diverging section and forms a vortex. Again the eddy viscosity and pressure are of maximum value at the orifice.

5.3.3.a The Effect of Upstream Geometry and Down Stream Diverging Angle

In Fig. E.4, the velocity distribution just before the orifice exit is shown. It is found that the NZ3.1 provides higher velocity. It also shows developed turbulent velocity profile and minimal flow separation inside the orifice. The behaviors of flow variables at the nozzle exit section are depicted in Figs. E.5-E.6. Fig. E.5 indicates that the nozzle with converging up stream and small diverging down stream provides higher momentum at the exit. Fig. E.6 shows that the circulation generates from the diverging portion of the nozzle travels all the way to the exit.

5.3.4 Results of Nozzle NZ4

In this simulation upstream of the nozzle is same for all four nozzles configurations. The effect of expansion ratio, diffuser angle and nozzle length are presented in Figs. E.7-E.13. Flow separation is noticed in the diverging section of the nozzle for all cases (Fig. E.7). Fig. E.8 shows the maximum pressure occurs at the entry of the orifice. The eddy viscosity contour plots are depicted in Fig. E.9.

5.3.4.a The Effect of Expansion Ratio

The axial and transversal velocity distributions are shown in Figs. E.10-E.12. It depicts that the velocity is higher for low expansion ratio (NZ4.2 & NZ4.3) than for ones with high expansion ratio. The nozzle with high expansion ratio (NZ4.1) also provides stronger circulation in the orifice as shown in Fig. E.13 since the velocity (v) shows higher fluctuation at nozzle exit.

5.3.4.b The Effect of Diverging Angle

The effect of diverging angle on exit velocity is also shown in Fig. E.12 for the nozzles NZ4.2 (30^0) and NZ4.3 (90^0). The smaller diverging angle provides a little higher velocity

at the exit which does not change significantly for this low expansion ratio. But NZ4.3 produces larger circulation vortexes inside orifice as depicted in Figs. E.7 and E.13.

5.3.4.c The Effect of Nozzle Length

The effect of diffuser length of the nozzle on exiting velocity is depicted in Fig. E.12 NZ4.1 and NZ4.4. It depicts that the shorter length (NZ4.4) assures a higher momentum at the exit of the orifice. This is due to the circulation vortexes generated after expansion which do not have sufficient time to absorb energy from the main stream of the flow.

5.3.5 Results of Nozzle NZ5

In Appendix E, the Figs. E.14-E.21 are referred to the results of nozzle NZ5. In this simulation the effect of two steps diverging as well as the diameter of orifice on flow field are analyzed. The stream line, pressure and eddy viscosity contours are depicted in Figs. E.14-E.16. It is noticed that eddy formation is very strong for two steps diverging and the separation spreads all the way to the exit of the nozzle. The maximum pressure drop occurred at the entrance of the orifice. In Fig. E.17, the centerline velocity distribution is shown. It shows similar nature for the velocity distribution. Fig. E.18 depicts the velocity distribution just before the orifice exit. The velocity at the axis is 900-1000 m/s. The velocity distributions after expansion and nozzle exit are shown in Figs. E.19 and E.20. By comparing NZ4.1 (one step diverging) and NZ5.1 (two steps diverging) it is found that nozzle with two expansions provides a little higher momentum at the exit (Fig. E.20).

The effect of orifice diameters is analyzed for NZ5.1 and NZ5.2. Fig. E.19 shows a little higher velocity for smaller orifice (NZ5.2). This minor variation of orifice diameters does not affect the exit velocity significantly (Fig. E.20). The transversal velocity (v) distribution at nozzle exit are presented in Fig. E.21. From this figure, it is clear that the core portion of the flow do not have strong fluctuating components and the flow exits the

nozzle like a jet surrounded by the highly fluctuating eddies. These results also agree with the high speed filming of the jet where the jet is covered by mist and vortexes.

5.4 Comparison of Numerically Computed Velocities at the Exit of the Nozzles

The velocity on the axis of NZ1 is listed in Table 5.6. It is noticed that 30-60^0 converging angle nozzles provide higher velocities at the exit. The smaller orifice shows higher exit velocity.

Table 5.6a Axis velocity u (m/s) of NZ1 at the Exit

d (mm)	10^0	15^0	30^0	60^0	90^0
0.254	830.10	835.00	829.46	797.03	968.50
0.127	771.35	-	855.31	950.16	907.90

Table 5.6b Axis Velocity of NZ1 (Converging Angle 60^0) at the Exit

d (mm)	0.127	0.178	0.254	0.305	0.356
u (m/s)	950.16	810.05	797.03	714.20	710.09

The velocities at the nozzles exit for NZ2 and NZ3 are listed in Table 5.7. It shows that two steps converging nozzle with a small diverging angle provides higher center line velocity (NZ2.2 and NZ3.3).

Table 5.7 Axis Velocity u (m/s) of NZ2 and NZ3 at the Exit

NZ2.1	NZ2.2	NZ2.3	NZ3.1	NZ3.2	NZ3.3
1268.3	1390.20	854.14	681.33	1011.80	1120.10

The center line velocities at the exit of nozzles NZ4 and NZ5 are listed in Table 5.8. It shows that low expansion ratio (NZ4.2 and NZ4.3) provides higher velocity on the axis. Two steps expansion do not have significant effect on exit velocities (NZ5).

Table 5.8 Axis Velocity u (m/s) of NZ4 and NZ5 at the Exit

NZ4.1	NZ4.2	NZ4.3	NZ4.4	NZ5.1	NZ5.2
768.00	1120.20	1091.80	891.36	919.68	889.96

5.5 Comparison of Experimental And Numerical Results

The converging nozzle NZ2.1 used in numerical simulation was employed for velocity measurement with the LTA. Both experimental and computational results for this nozzle are depicted in Fig. 5.1. An experimental result of Trupel (Abramovich, 1963) for a submerged jet is also plotted in this figure. The similarity of velocity profile is found near the core section of the jet which validates the conventional turbulent pattern of the jet.

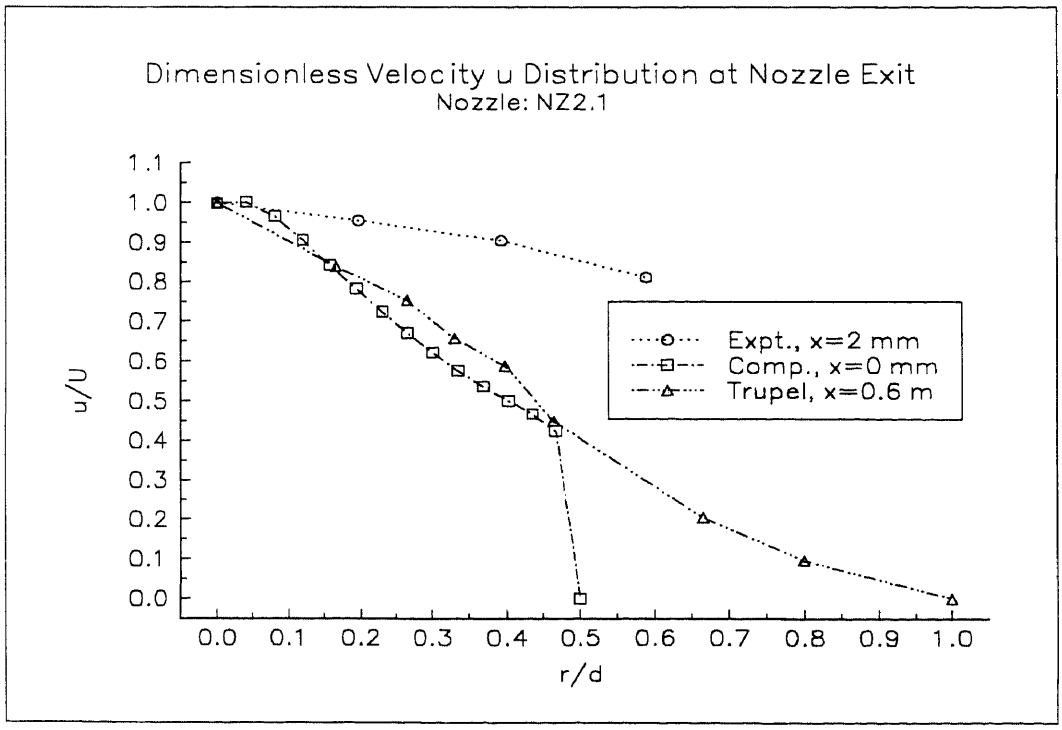

Figure 5.1 Comparison of Experimental and Numerical Results of the Nozzle NZ2.1

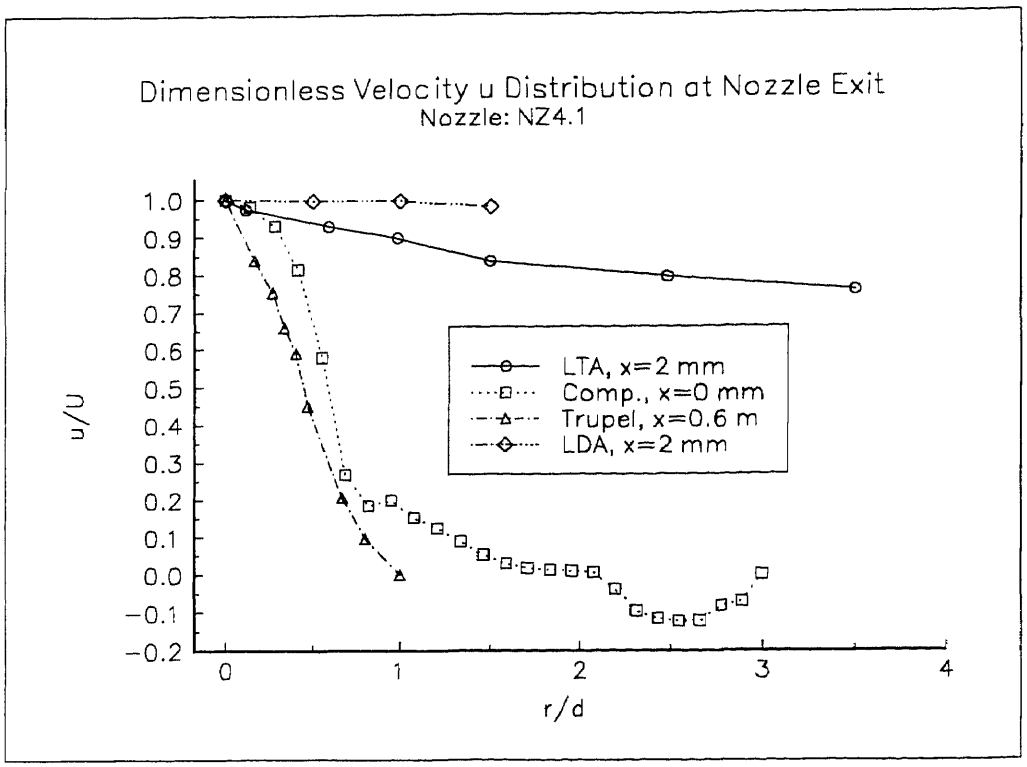

Figure 5.2 Comparison of Experimental and Numerical Results of the Nozzle NZ4.1

The nozzle NZ4.1 used in numerical simulation was also applied in experimental investigation with both LTA and LDA. The dimensional velocity distribution in the transversal direction is compared with the submerged jet (Abramovich, 1963) in Fig. 5.2. It shows the dimensional similarity of the turbulent jet. The velocity distribution shows that numerical prediction agrees well in the core section of the jet. Due to the violent circulation vortexes, the k-ε model under-estimates the spatial velocity distribution.

CHAPTER 6

CONCLUSIONS AND RECOMMENDATIONS

6.1 Concluding Remarks

The mechanism of formation of highly turbulent WJ and AWJ is established in this investigation. A comprehensive experimental technique for the investigation of WJ and AWJ by LTA, piezoelectric force transducer and high speed filming is established and validated by numerical results. A practical numerical technique for finite element simulation by the use of the k-ε turbulence model for flow analysis in sapphire water jet nozzles has been developed. Numerically the parameter optimization of sapphire nozzles allows construction of a knowledge base for the selection of the nozzle geometry in the course of the water jet nozzle design.

The velocity distributions along and across jet and the forces generated by jet workpiece interaction are determined. Sapphire nozzle area has profound effect on jet dynamics. The velocity distribution along and across jet shows the normal turbulent behavior of the jet at the macro level. WJ velocities are in the range of 750-800 m/s. Abrasive velocities (300-500 m/s) significantly depend on the alignment of carbide tube and sapphire nozzle. The present mixing process is not efficient since abrasive fed from the side port by gravity resulted in a very low velocity of abrasive particles with respect to water particles.

The high speed filming reveals the dynamics and instantaneous behaviors of the jets. At the micro level the high speed jet is a sequence of disintegrated slugs. Flow discontinuity caused particle accumulation resulted in sudden expansion and contraction of the jet. Segregated flow of abrasive particles creates cavities inside jet.

The numerical prediction of the flow inside nozzle generally complies well with the experimental data. The converging nozzles produce concentrated high energy jet which

can be used for conventional cutting operations whereas the nozzles with diverging section produce cavities and circulation around jet which can be used for cleaning and polishing purposes.

Converging nozzle ($30\text{-}60^0$) with orifice length 4-6 times of orifice diameter produces higher velocity at the exit of the nozzle. Flow is separated in the diverging section of the nozzle and it forms circulation which in turn produces pulse jet. Enhancement of in-nozzle circulation is achieved by 60^0 diverging angle with expansion ratio of 3-6 which enables percussive jet. Nozzle with two steps diverging produces enhanced pulsing jets.

The mechanism of formation of high Reynolds water and abrasive-water jets and the effect of the nozzle design on the jet anatomy is well established in this investigated span of process conditions. The integration of experimental and numerical results provide a knowledge base for nozzle design in various industrial applications.

6.2 Recommendations for Future Studies

To have a complete understanding of the mechanism of WJ and AWJ formation, the following studies are necessary:

- It is required to investigate velocity and pressure fields experimentally inside nozzles.
- Numerical prediction of AWJ is to be developed.
- Model needs to consider three dimensional turbulence in the recirculation regions and two phase (water and air) flow.
- Existing mixing chamber of water-abrasive is to be redesigned to have higher abrasive particle velocity.
- A model demonstrates stress developed during metal-jet interaction.

APPENDIX A

NOZZLES CONFIGURATIONS AND BOUNDARY CONDITIONS

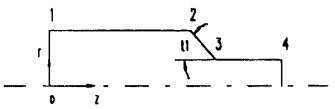

NZ1

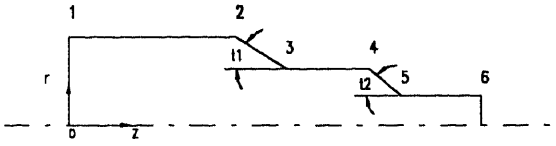

NZ2

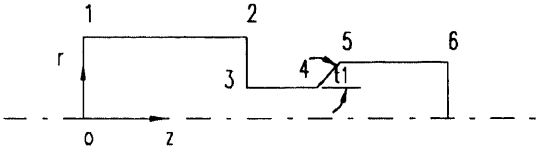

NZ3.1

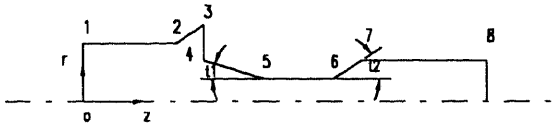

NZ3.2

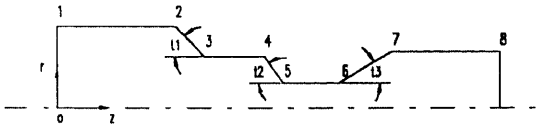

NZ3.3

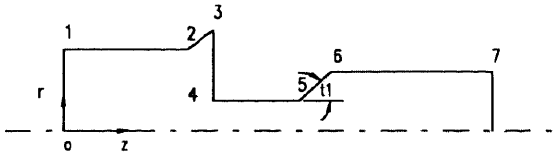

NZ4

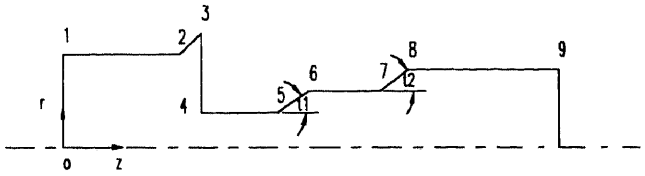

NZ5

Figure A.1 Schematics and Dimensions of the Nozzles used in Numerical Simulations

Table A.1a Geometrical Parameters of the Nozzle NZ1
(r1=r2=1.598 mm, r3=r4=0.127 mm)

Nozzle NZ1	Angle t1 (deg)	z2 (mm)	z3 (mm)	z4 (mm)
NZ1.1	10	15.980	24.322	26.872
NZ1.2	15	15.980	21.750	24.300
NZ1.3	30	15.980	18.528	21.078
NZ1.4	60	15.980	16.829	19.379
NZ1.5	90	24.300	24.300	25.570

Table A.1b Geometrical Parameters of the Nozzle NZ1
(r1=r2=1.598 mm, r3=r4=0.0635 mm)

Nozzle NZ1	Angle t1 (deg)	z2 (mm)	z3 (mm)	z4 (mm)
NZ1.1	10	15.980	24.680	27.23
NZ1.2	30	15.980	18.640	21.19
NZ1.3	60	15.980	16.866	19.46
NZ1.4	90	15.980	15.98	18.53

Table A.1c Geometrical Parameters of the Nozzle NZ1
(t1=60 deg., r1=r2=0.1598 mm)

Nozzle NZ1	r3=r4 (mm)	z2 (mm)	z3 (mm)	z4 (mm)
NZ1.1	0.089	15.980	16.85	19.40
NZ1.2	0.152	15.980	16.81	19.36
NZ1.3	0.178	15.980	16.80	19.35

Table A.2 Geometrical Parameters of the Nozzle NZ2
(r1=r2=1.598 mm, r5=r6=0.127 mm)

Nozzle NZ2	Angle t1(deg)	Angle t2(deg)	r3=r4 (mm)	z2 (mm)	z3 (mm)	z4 (mm)	z5 (mm)	z6 (mm)
NZ2.1	90	45	1.016	15.98	15.980	24.435	25.324	26.594
NZ2.2	45	45	1.016	15.398	15.980	24.435	25.324	26.594
NZ2.3	90	45	1.016	15.98	15.98	24.435	25.324	31.25

Table A.3 Geometrical Parameters of the Nozzle NZ3
(NZ3.1: r1=r2=1.598, r3=r4=0.127, r5=r6=0.762 mm
NZ3.2: r1=r2=1.598, r3=2.13, r4=1.09, r5=r6=0.127, r7=r8=0.762 mm
NZ3.3: r1=r2=1.598, r3=r4=1.016, r5=r6=0.127, r7=r8=0.762 mm)

NZ3 mm	t1 deg	t2 deg	z2 mm	z3 mm	z4 mm	z5 mm	z6 mm	z7 mm	z8 mm
NZ3.1	30	-	15.98	15.98	17.28	18.37	26.68	-	-
NZ3.2	15	60	2.54	3.45	3.45	6.78	8.05	8.41	14.05
NZ3.3	45	30	15.40	15.98	24.44	25.32	26.59	27.68	35.99

Table A.4 Geometrical Parameters of the Nozzle NZ4
(r1=r2=1.598 mm, r3=2.13 mm, r4=r5=0.127 mm)

NZ4 mm	t1 deg	r6=r7 mm	z2 mm	z3=z4 mm	z5 mm	z6 mm	z7 mm
NZ4.1	30	0.762	2.54	3.45	4.75	5.84	14.15
NZ4.2	30	0.381	2.54	3.45	4.75	5.19	14.15
NZ4.3	90	0.381	2.54	3.45	4.75	4.75	14.15
NZ4.4	30	0.762	2.54	3.45	4.75	5.84	7.00

Table A.5 Geometrical Parameters of the Nozzle NZ5
(r1=r2=1.60, r3=2.13, r6=r7=0.292, r8=r9=0.793 mm and t1=t2=60 deg)

NZ5 mm	z2 mm	z3=z4 mm	z5 mm	z6 mm	z7 mm	z8 mm	z9 mm
NZ5.1 r4=r5=0.127	2.54	3.45	4.53	4.62	6.13	6.46	14.06
NZ5.2 r4=r5=0.089	2.54	3.45	4.53	4.62	6.13	6.46	14.02

Table A.6 Inlet Boundary Conditions for the Numerical Simulations

Orifice d (mm)	Flow Q (lit/min)	u (cm/s)	k (cm^2/s^2)	ε (cm^2/s^3)
0.127	0.385	110.00	1.694e3	1.089e8
0.178	0.836	210.0	6.174e3	5.45e8
0.254	1.486	400.00	2.24e4	2.64e9
0.305	1.558	495.00	3.43e4	4.18e9
0.356	1.935	500.00	3.50e4	3.679e9

APPENDIX B

FIGURES SHOWING EXPERIMENTAL RESULTS

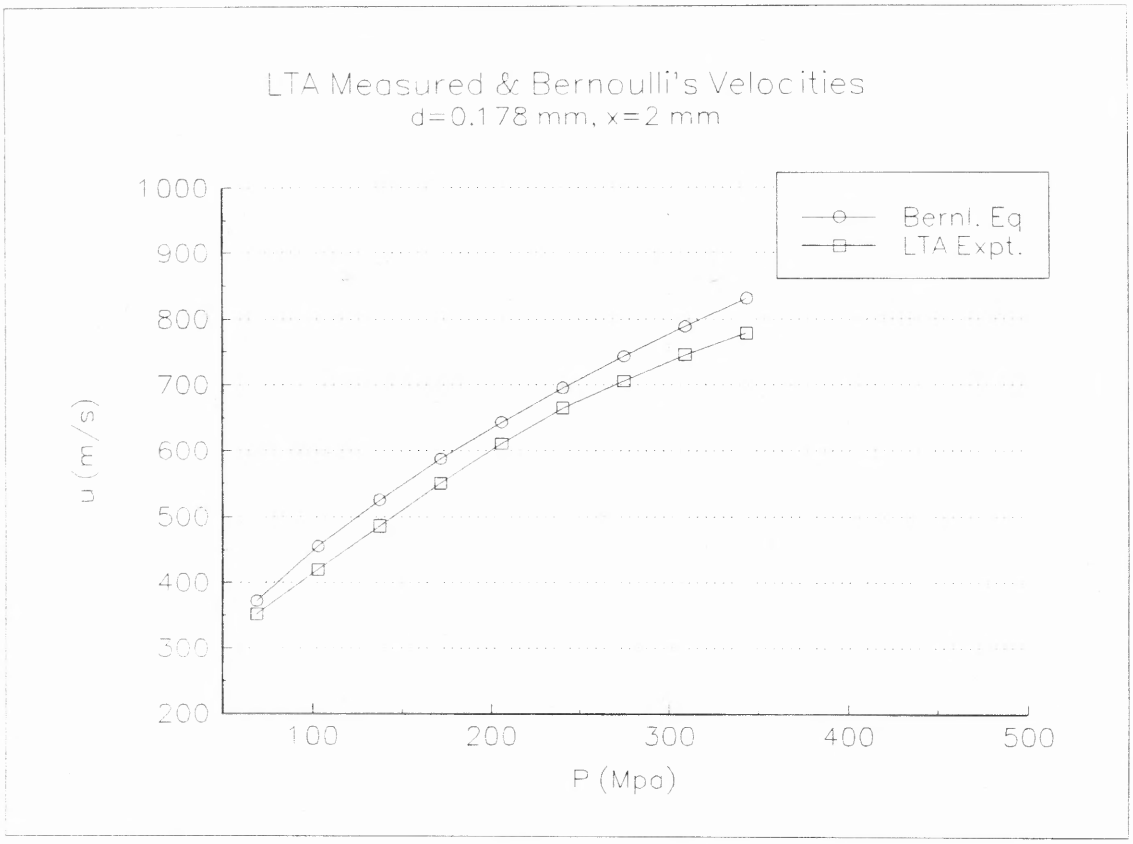

Figure B.1 Comparison of Velocities obtained from LTA and Bernoulli's Equation

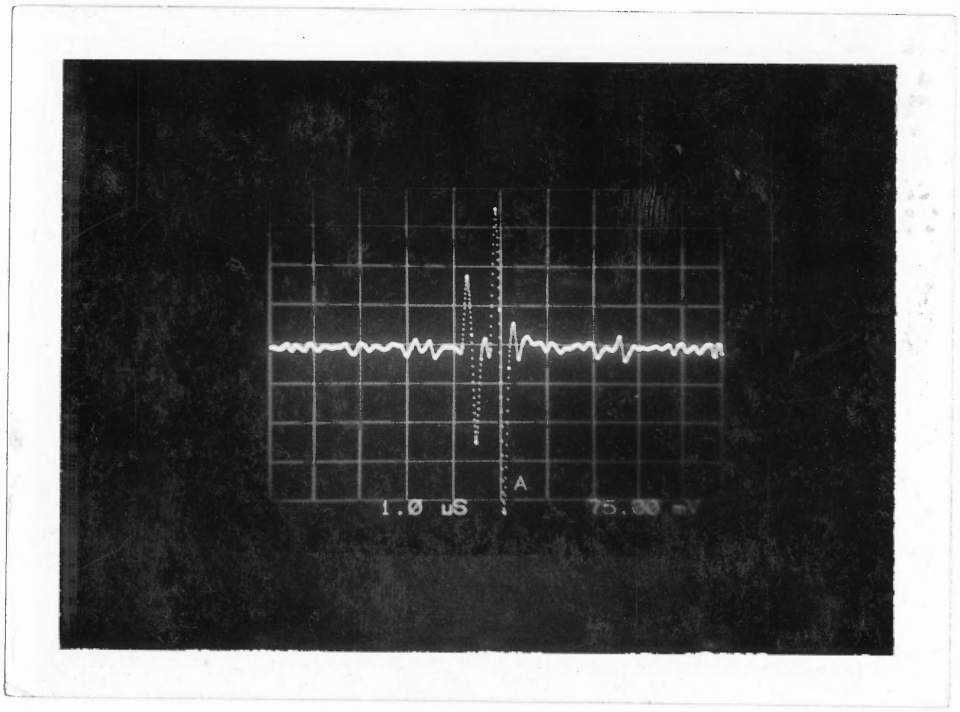

(a) Sapphire WJ (d=0.178mm, x=2.0 mm)

Figure B.2 Caption is in the next page

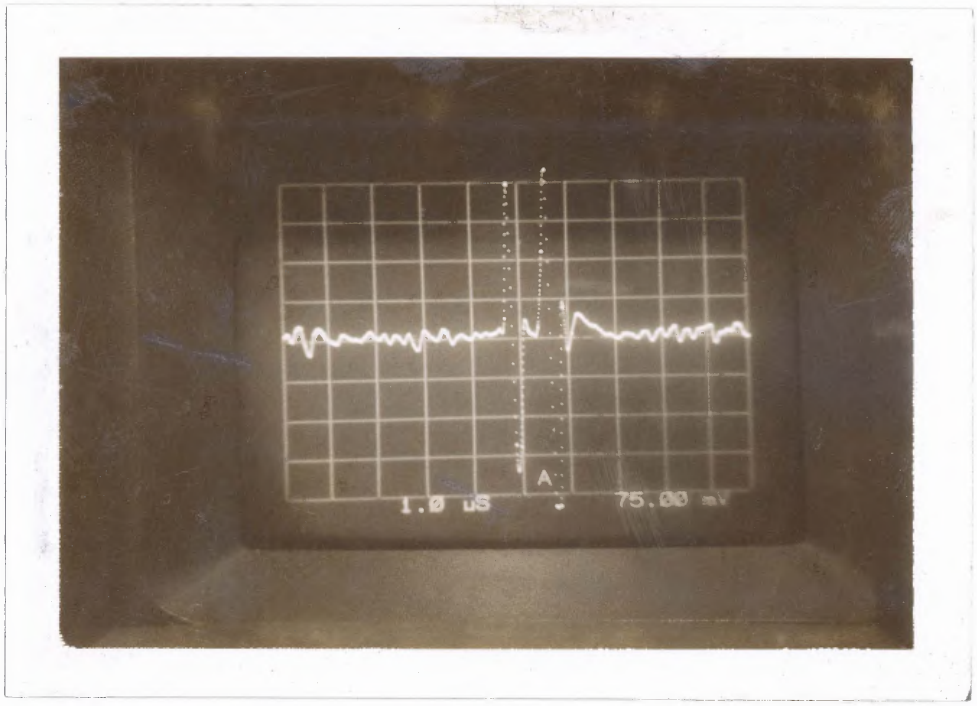

(b) Sapphire-Carbide WJ (d=0.178, D=1.600 mm, x=2.0 mm)

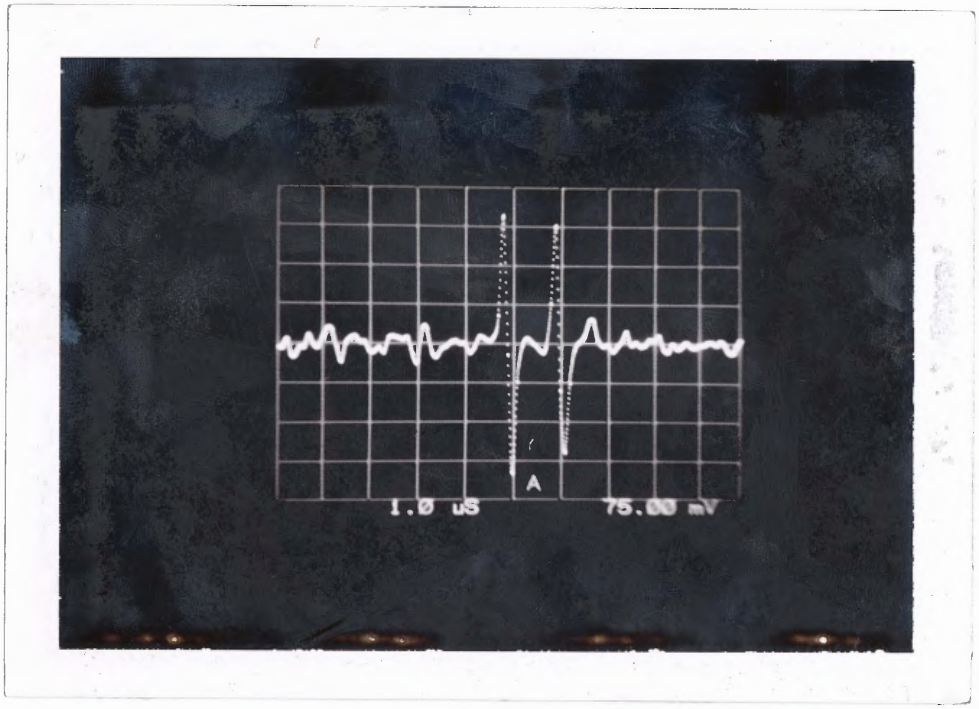

(c) AWJ (HP 50 with flow rate 76 g/min, d=0.178, D=1.600 mm, x=2.0 mm)

Figure B.2 Oscillograms of LTA Signals

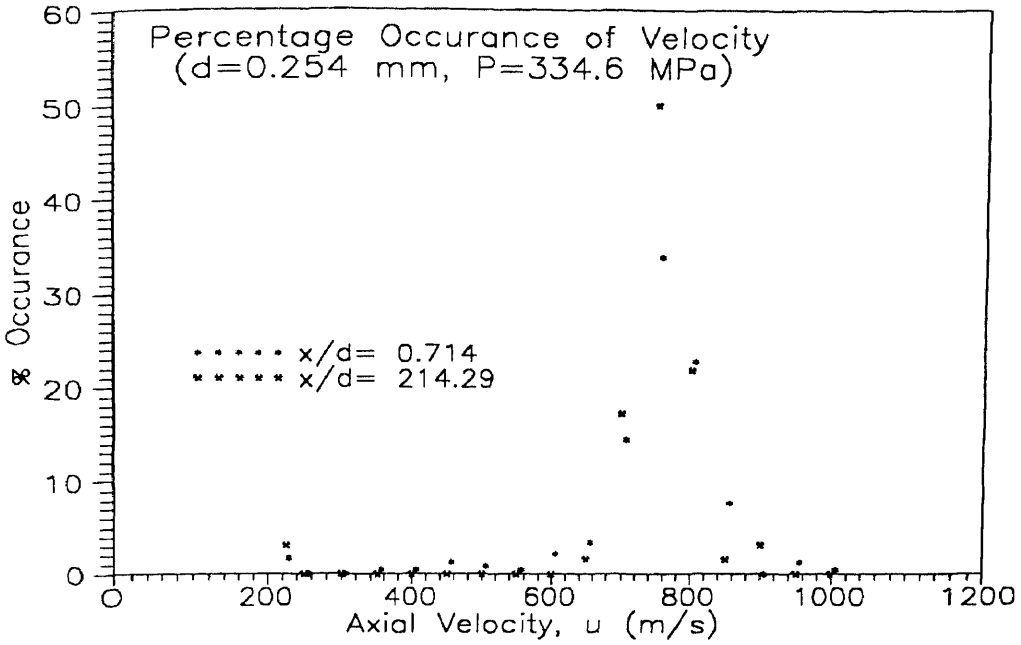

Figure B.3 Velocity Probability Distribution of Sapphire WJ obtained by LTA

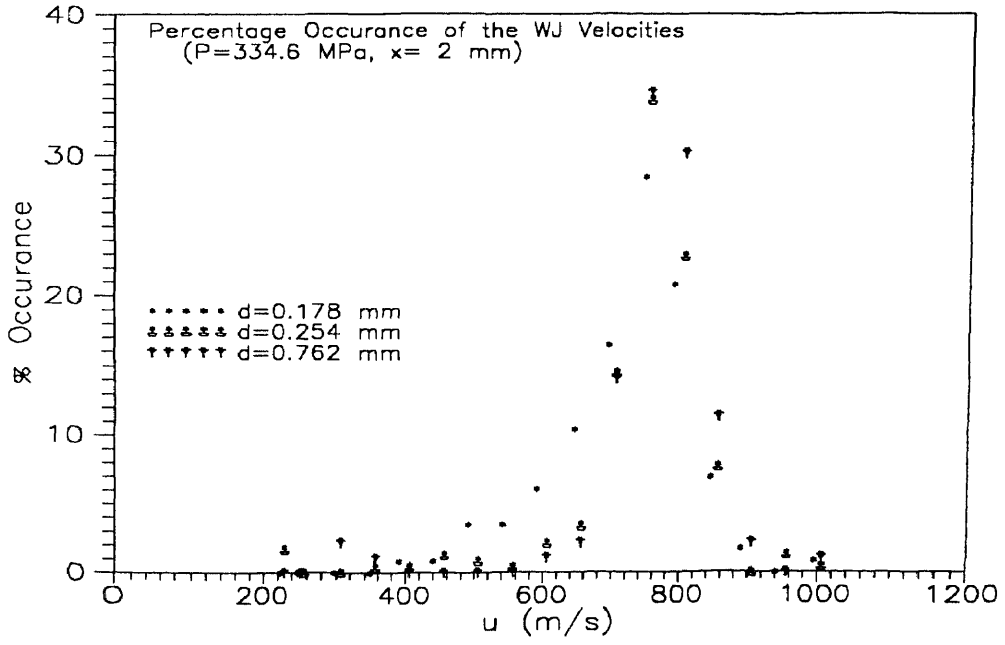

Figure B.4 Velocity Probability Distribution of Sapphire WJ obtained by LTA

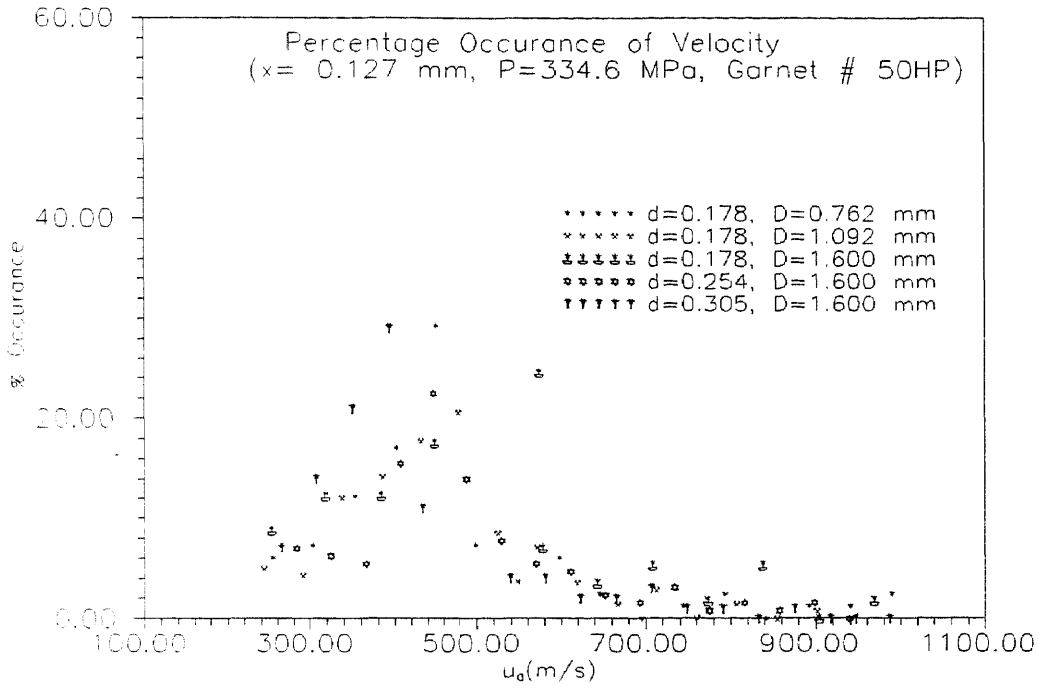

Figure B.5 Probability Distribution of AWJ Velocities obtained by LTA

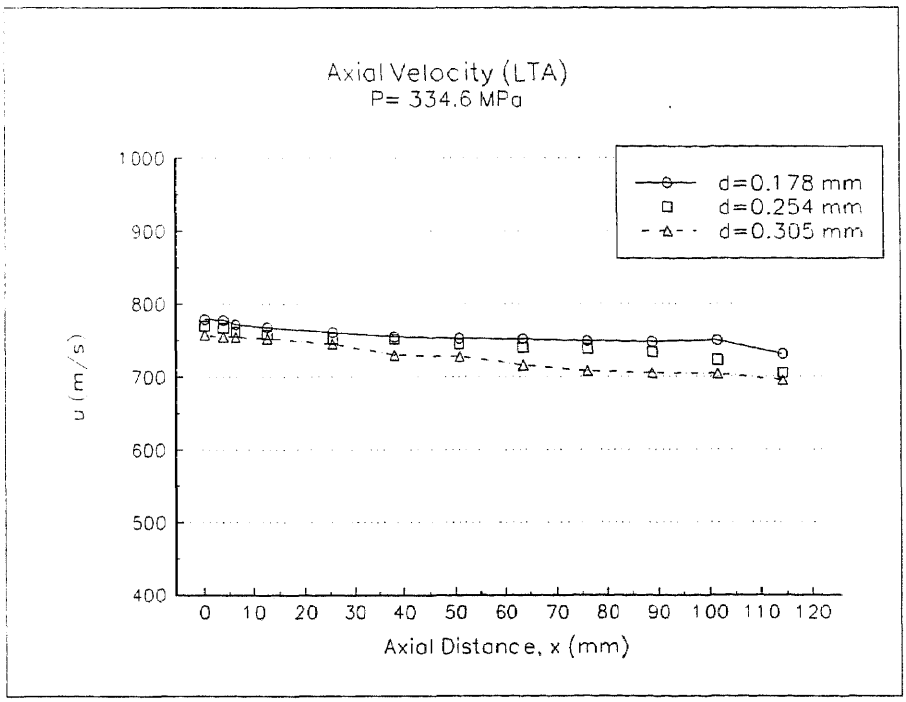

Figure B.6 Centerline Velocity Distribution of Sapphire WJ

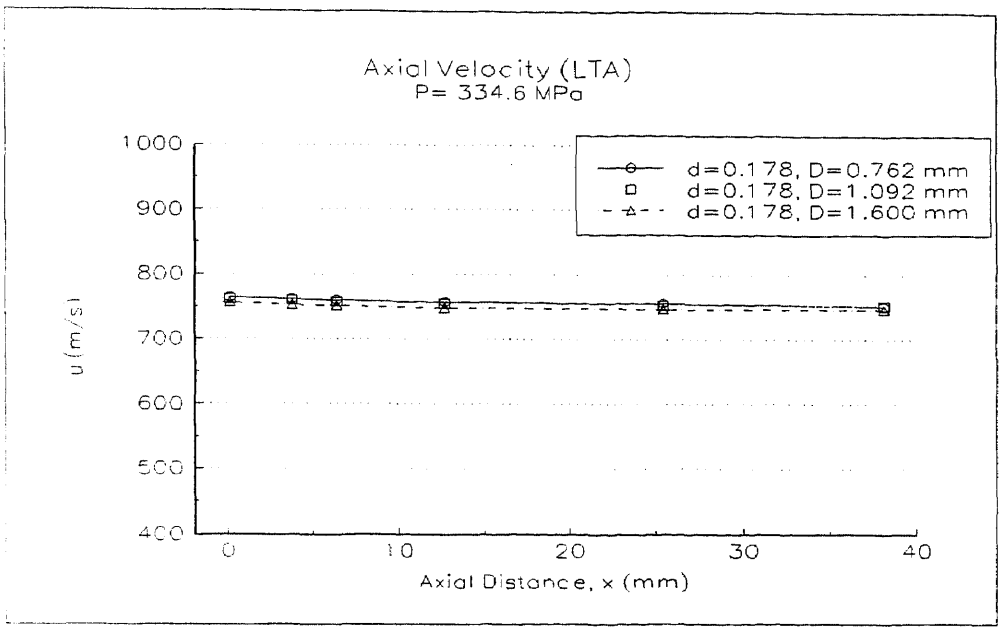

Figure B.7 Centerline Velocity Distribution of Sapphire-Carbide WJ

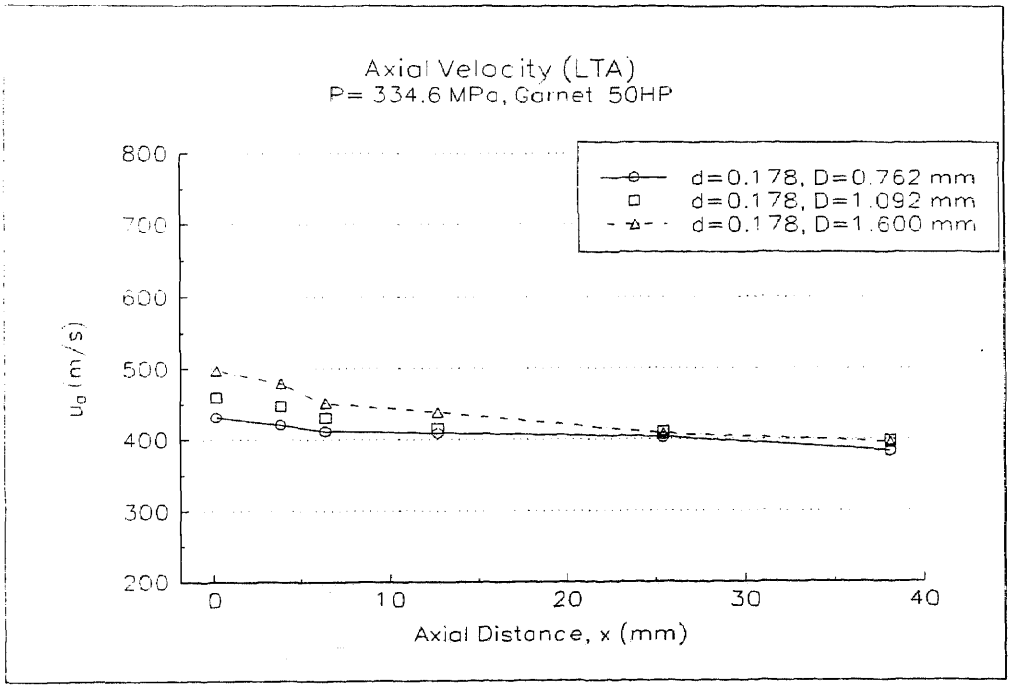

Figure B.8 Centerline Velocity Distribution of AWJ

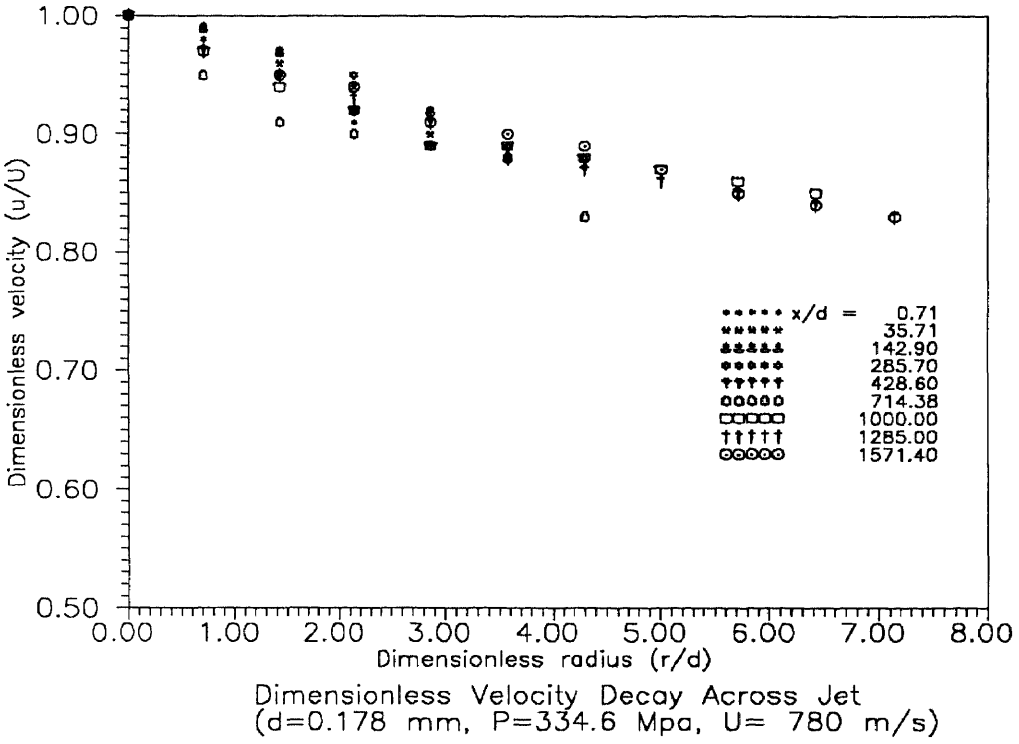

Figure B.9 WJ (Sapphire Nozzle) Velocity Distribution Across Jet

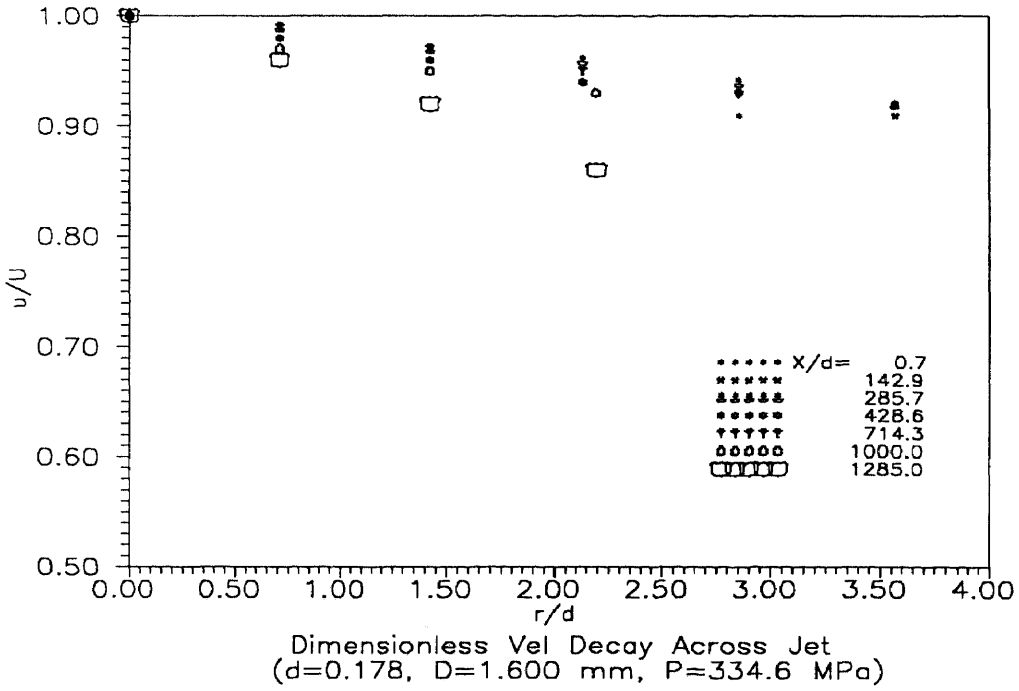

Figure B.10 WJ (Sapphire-Carbide Nozzle) Velocities Distribution Across Jet

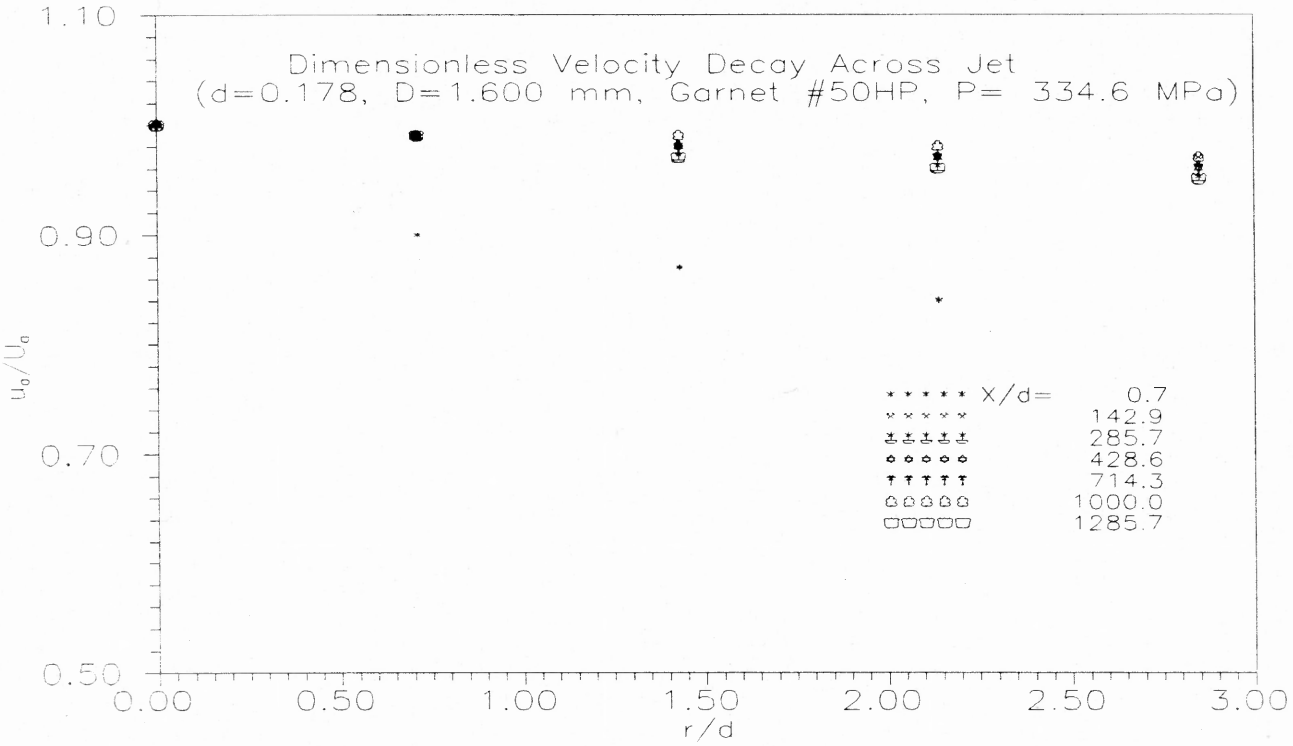

Figure B.11 AWJ Velocity Distribution Across Jet

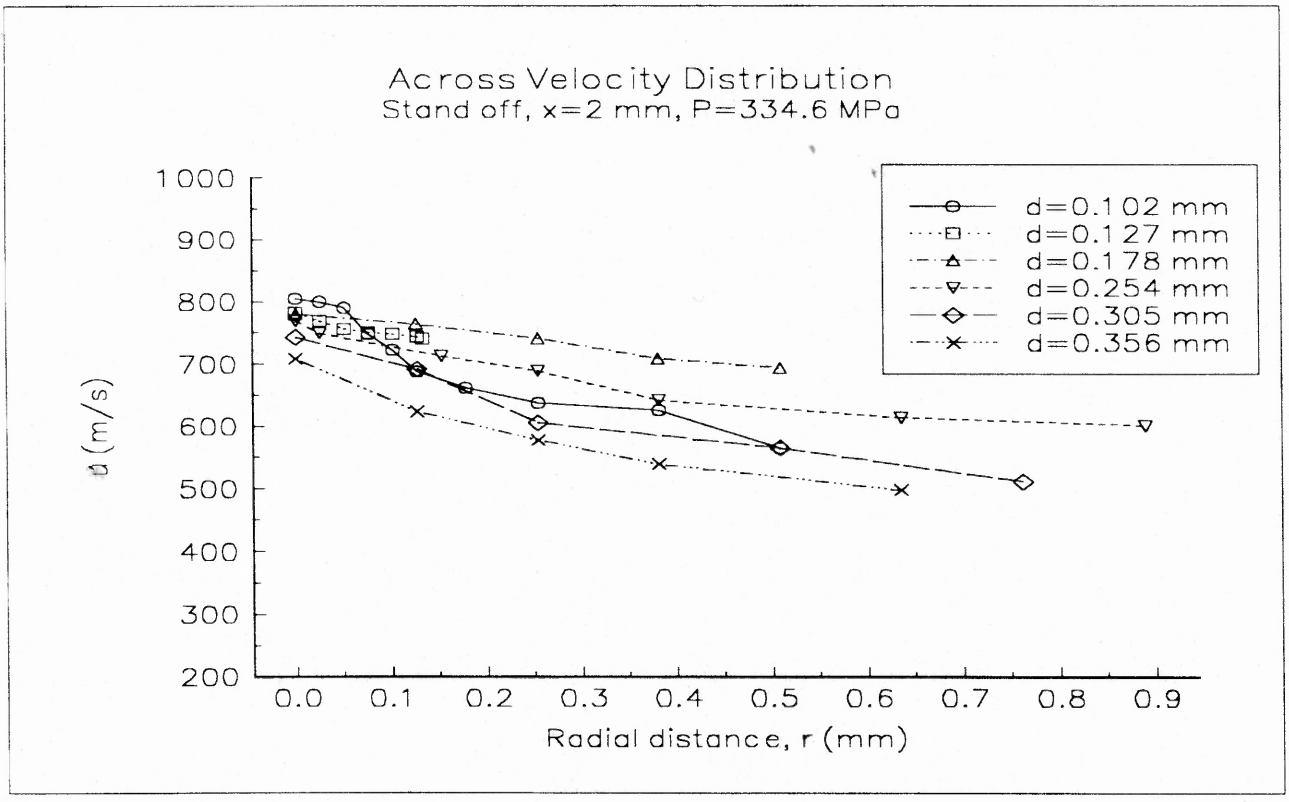

Figure B.12 WJ (Sapphire Nozzle) Velocities Across Jet

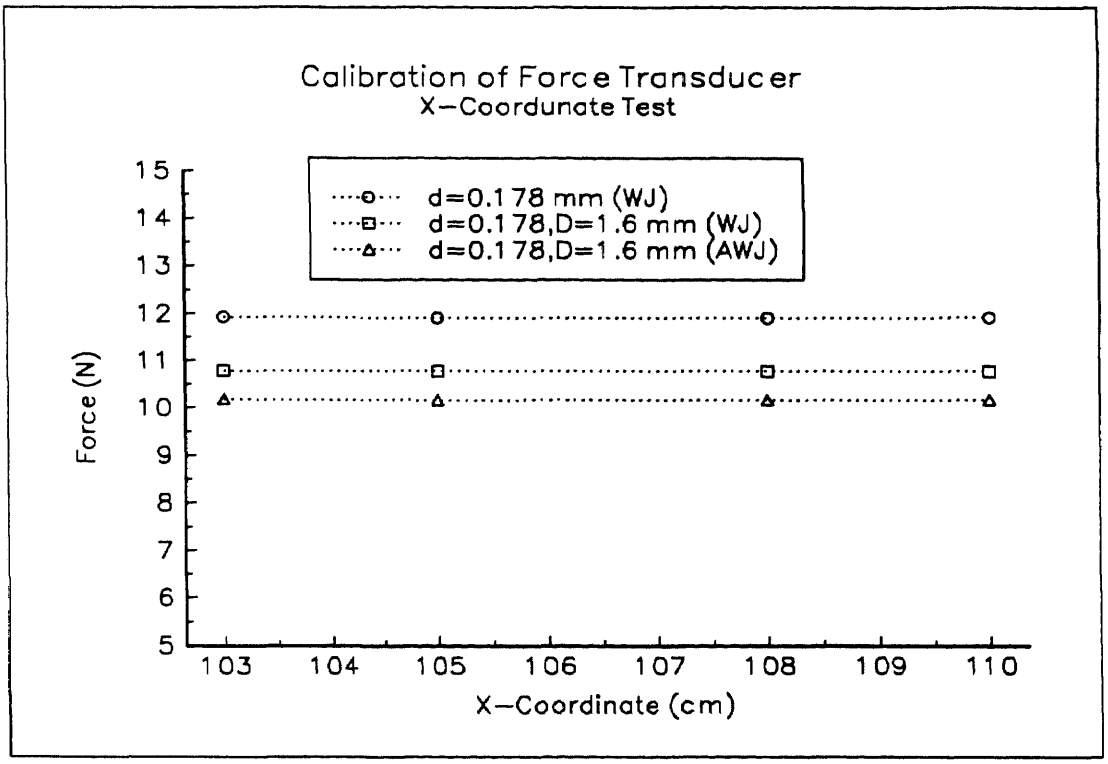

(a)

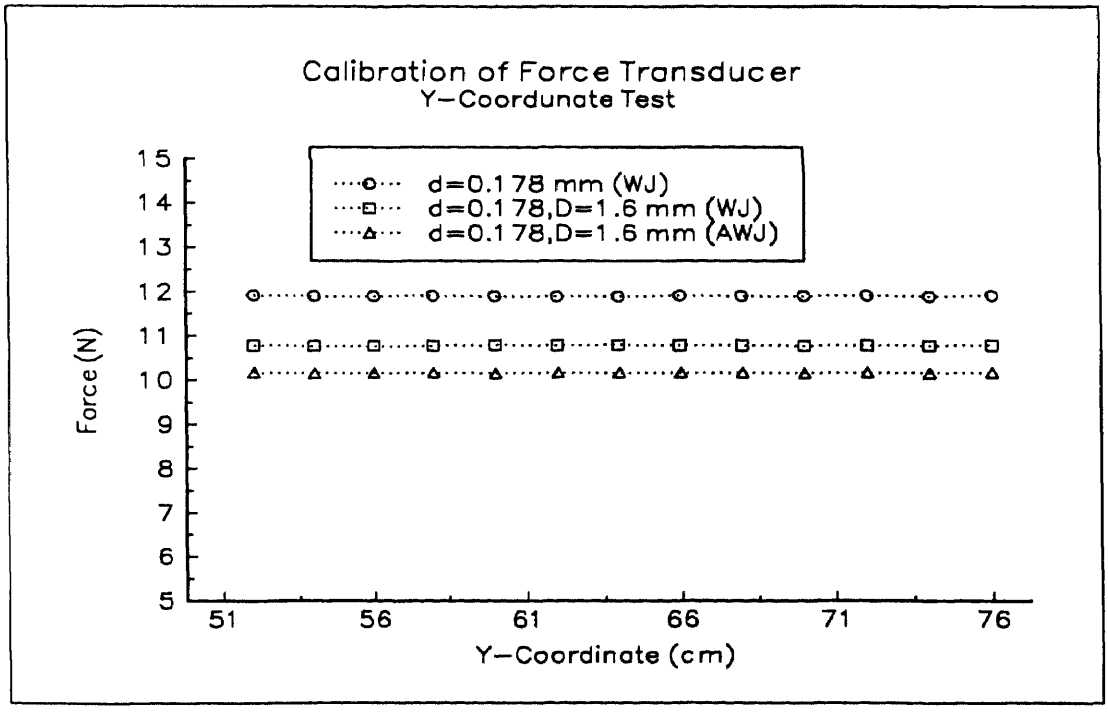

(b)

Figure B.13 Calibration of Force Transducer (Stand off Distance, x= 25.4 mm)

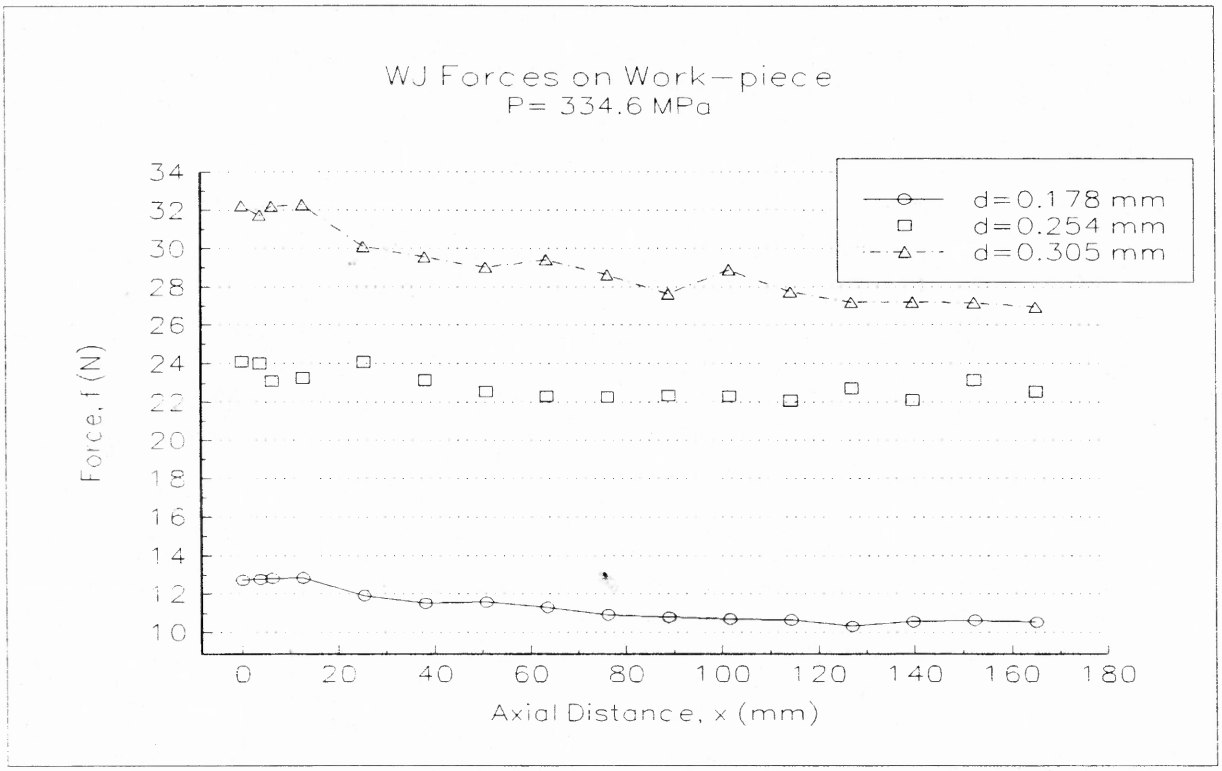

Figure B.14 WJ Forces (Sapphire Nozzle) Distribution Along Axis of the Jet

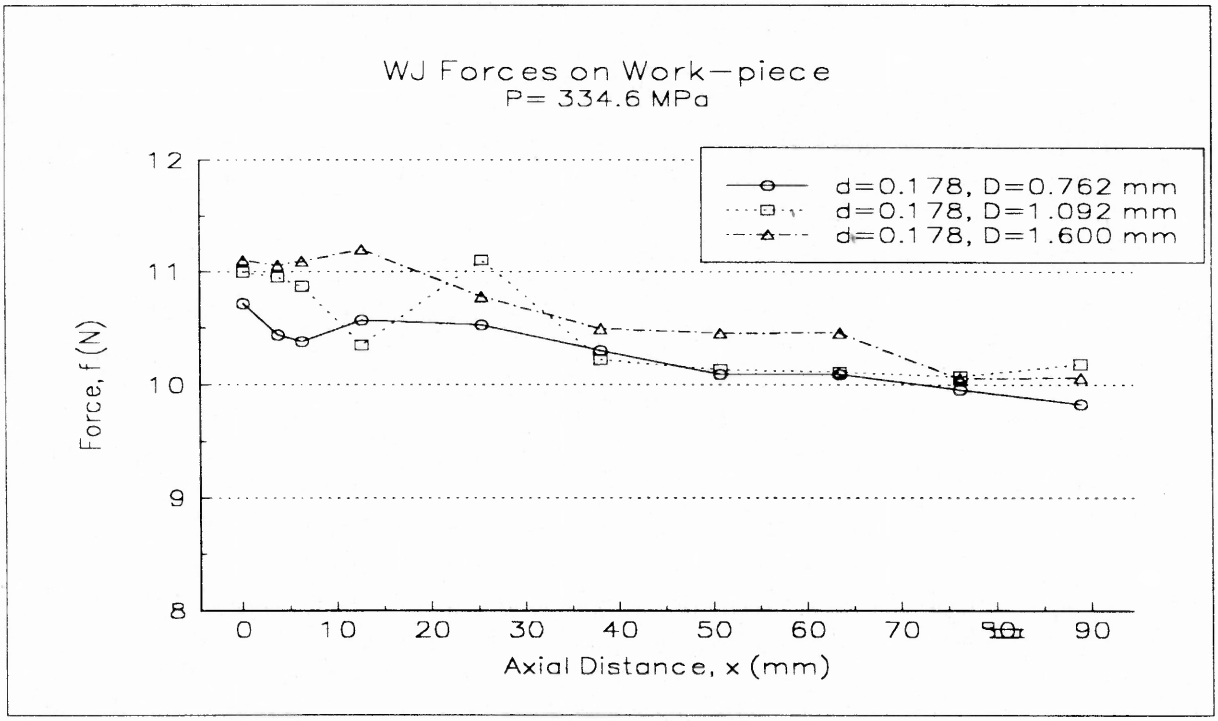

Figure B.15 WJ Forces (Sapphire-Carbide Nozzle) Distribution Along Axis of the Jet

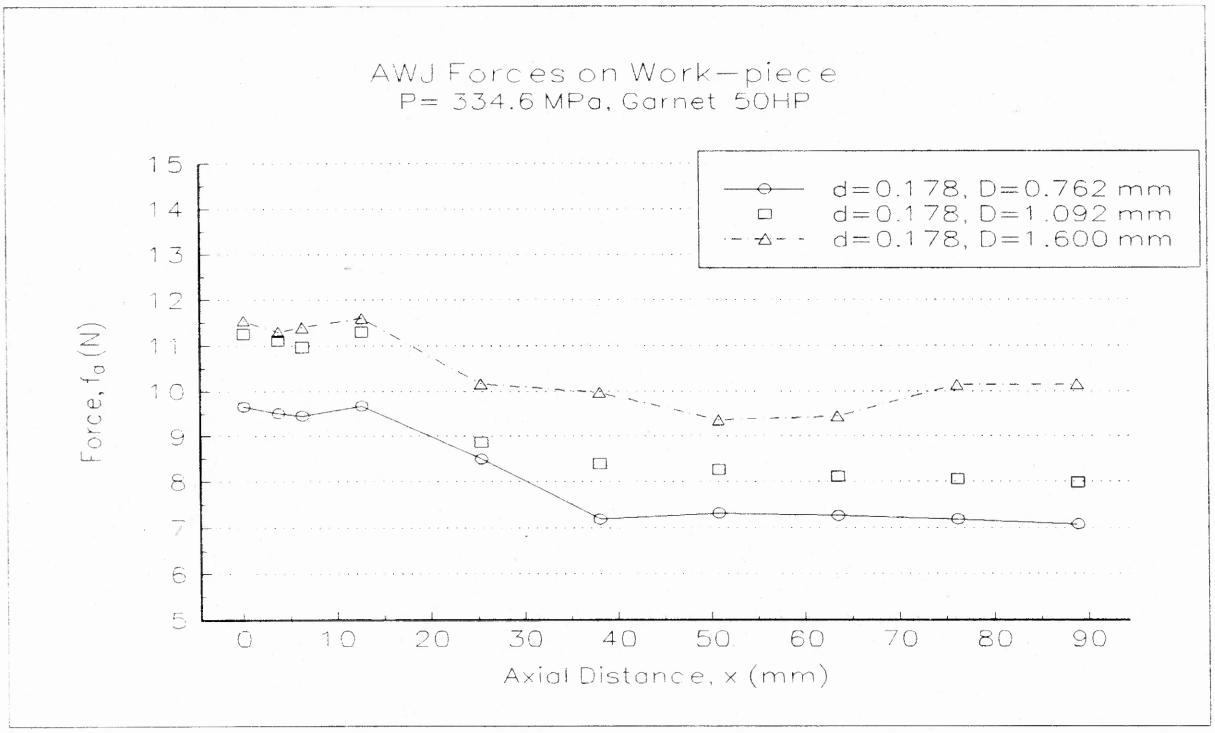

Figure B.16 AWJ Forces Distribution Along Axis of the Jet

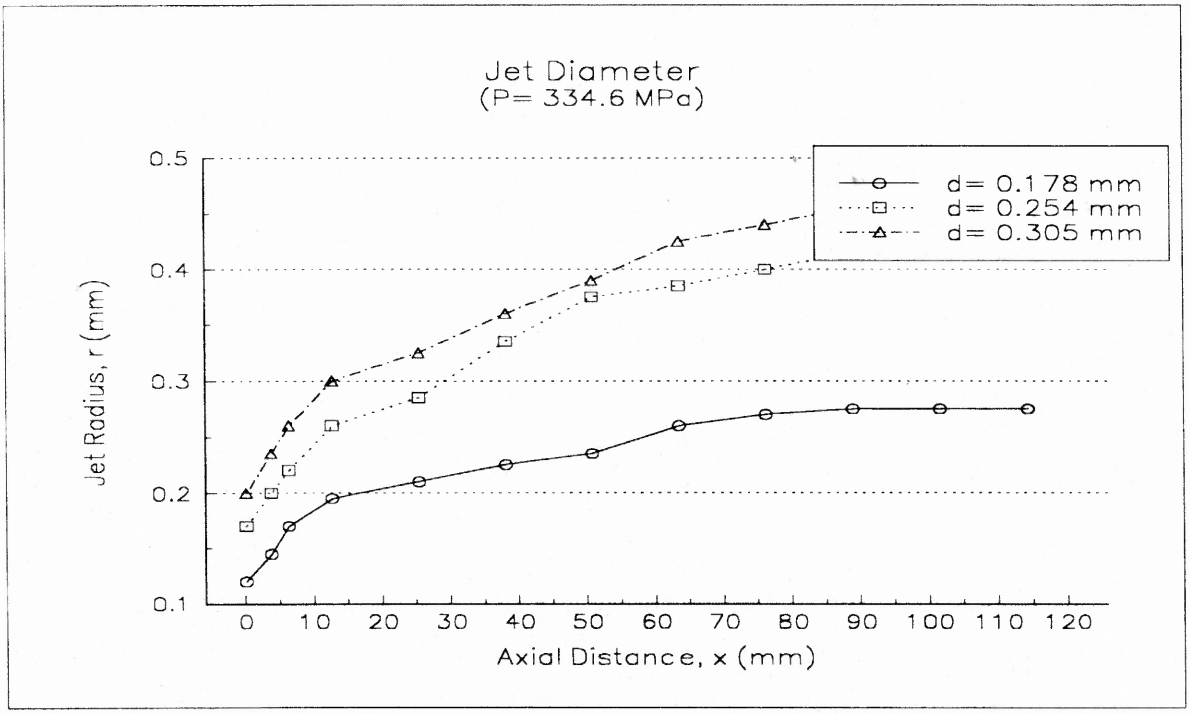

Figure B.17 WJ Spreading Along Axis of the Jet for Different Sapphire Nozzles

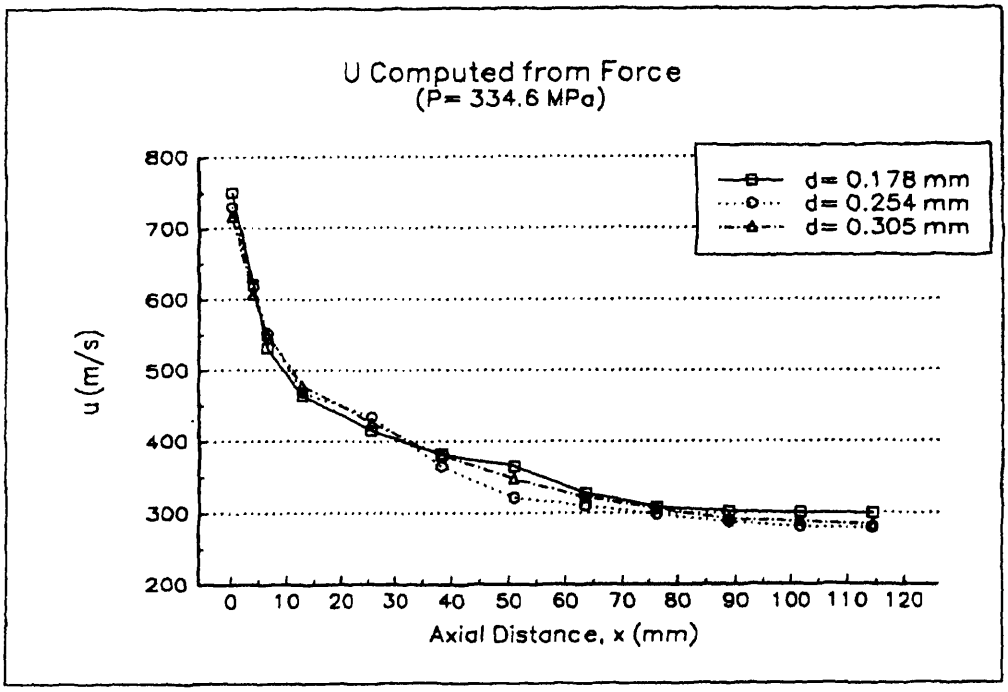

Figure B.18 Average Sapphire WJ Velocities Distribution Along Axis of the Jet

APPENDIX C

FIGURES SHOWING HIGH SPEED FILMING

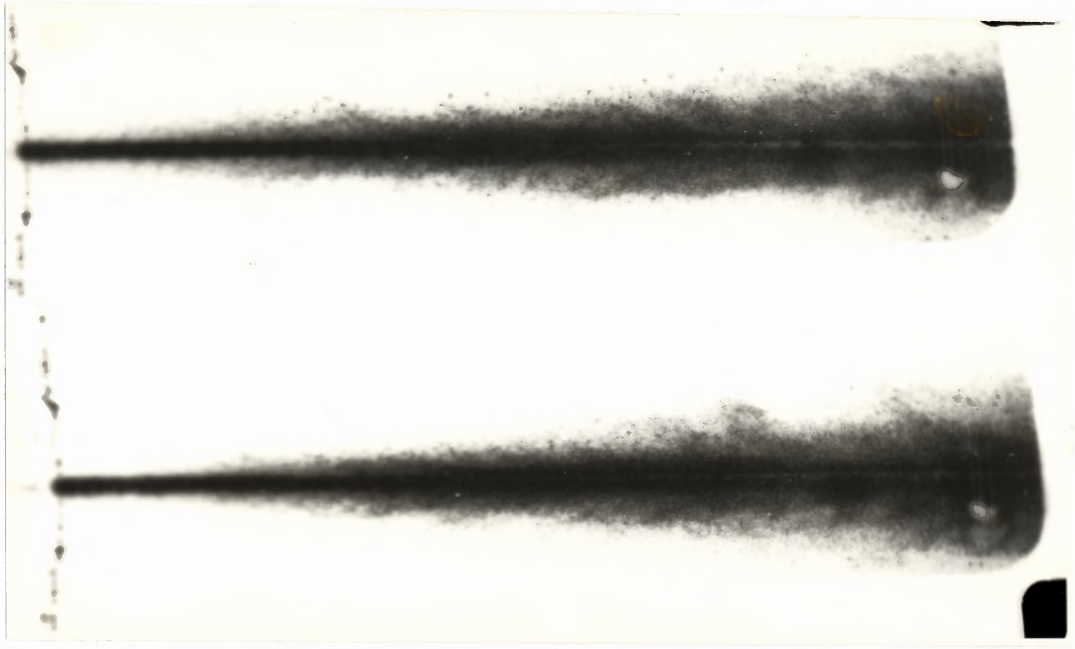

(a) Nozzle d=0.127 mm

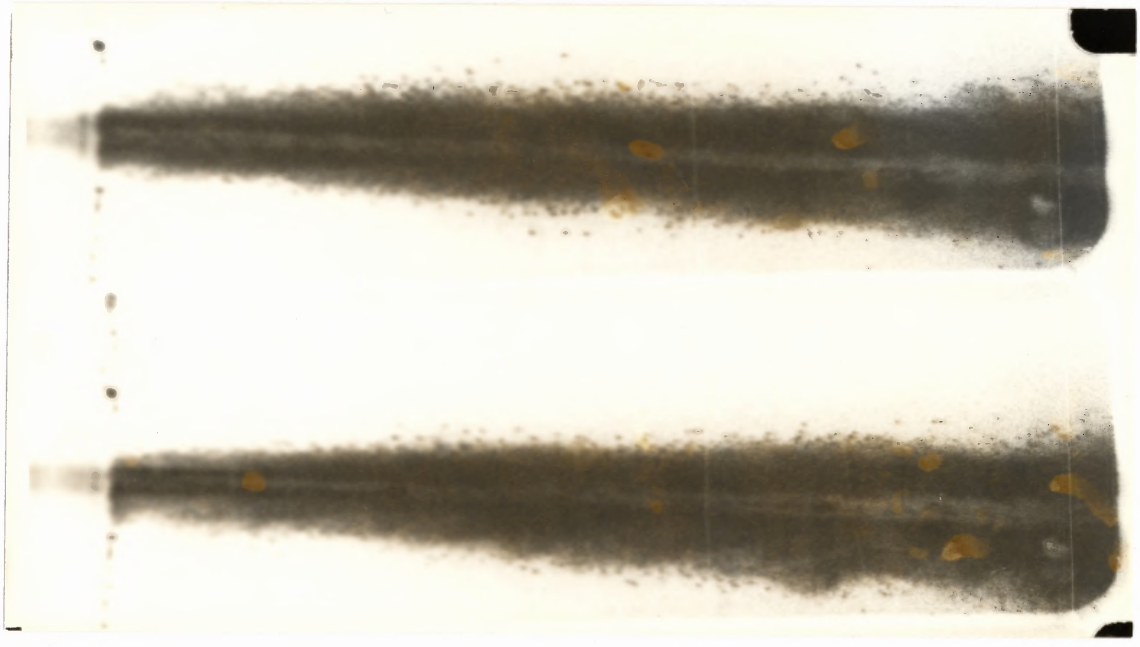

(b) Nozzle d=0.254 mm

Figure C.1 WJ Shows the Core, Mist and Droplet Regions

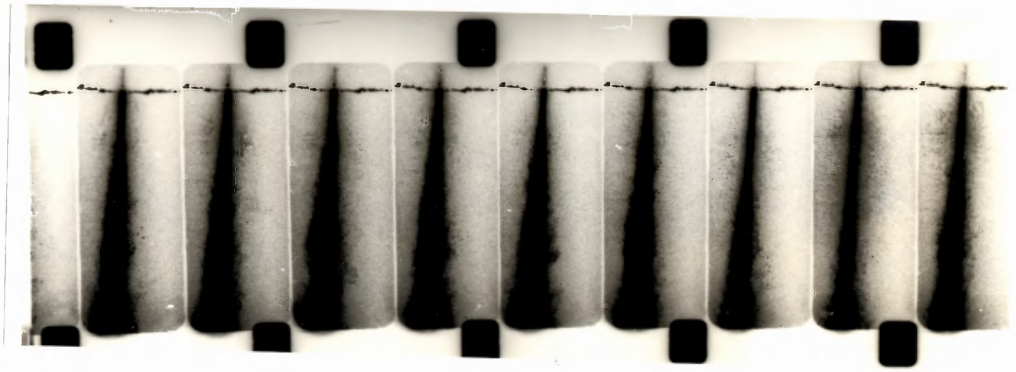

(a) Nozzle d=0.127 mm

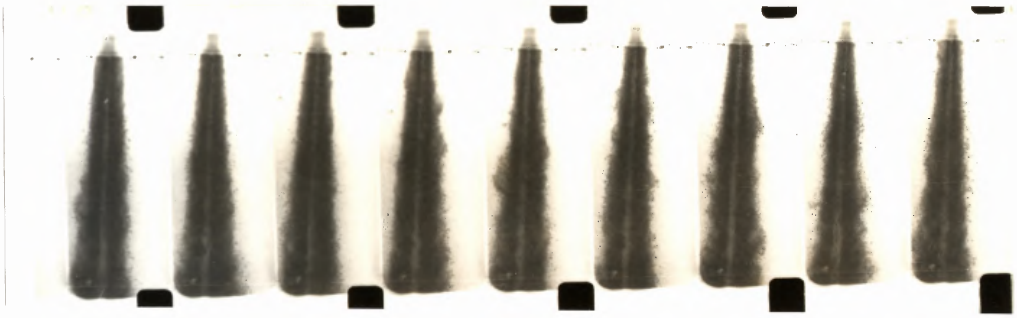

(b) Nozzle d=0.254 mm

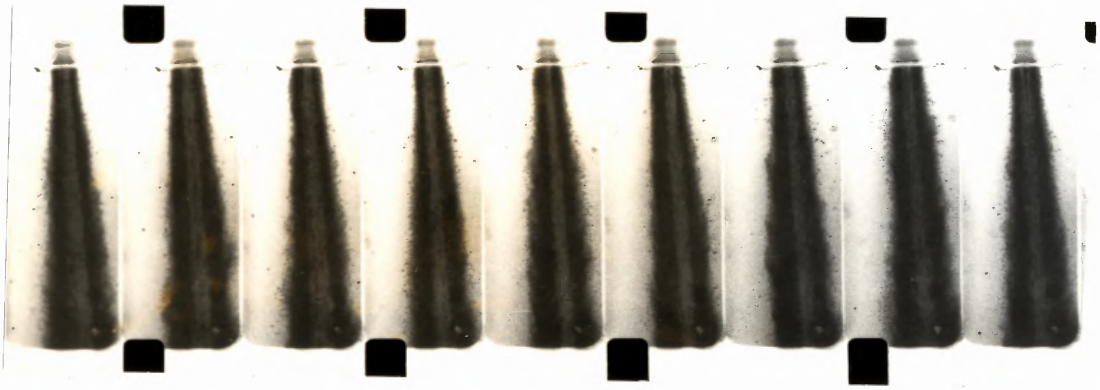

(c) Nozzle d=0.356 mm

Figure C.2 Sequential WJ Apart by the Time 0.125 Milliseconds

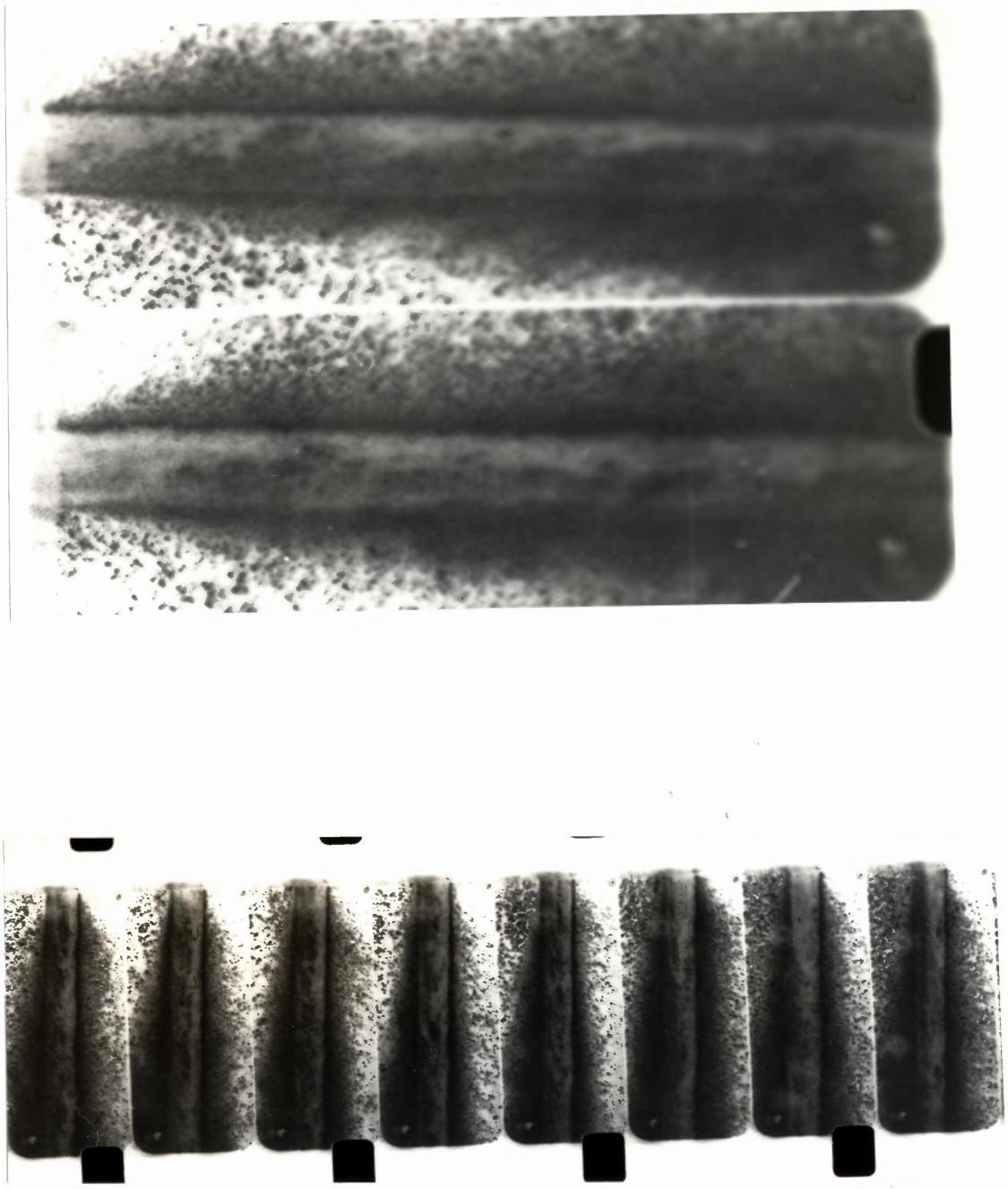

Figure C.3 WJ from Sapphire-Carbide Nozzle (d=0.254, D=0.762 mm)

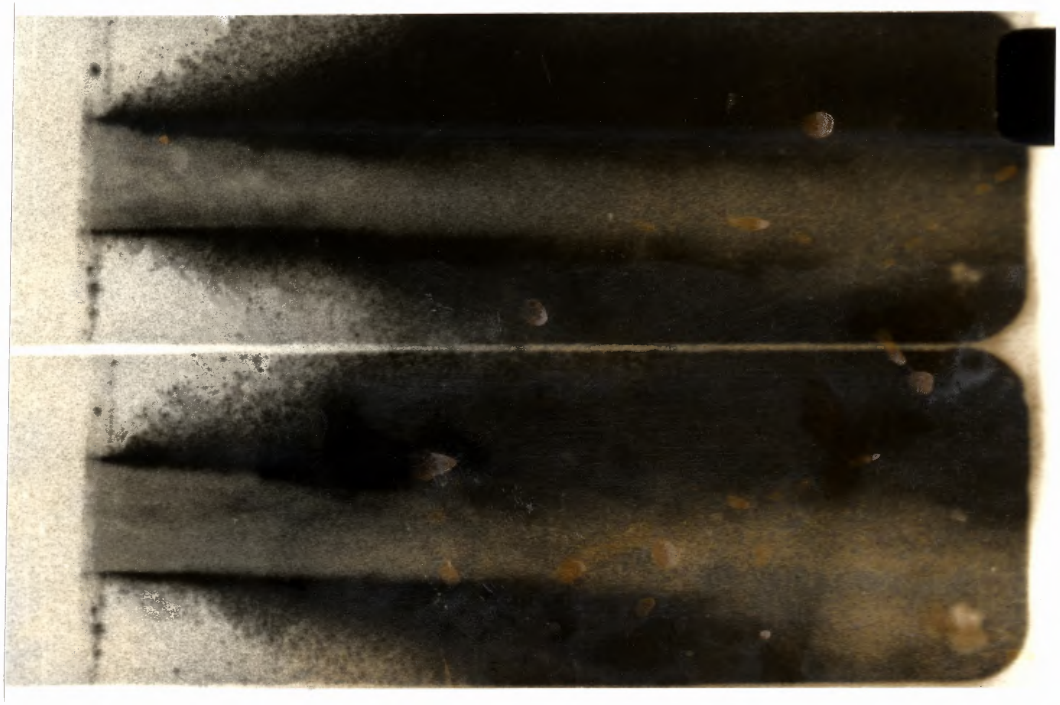

(a) Nozzle d=0.254, D=2.362 mm, HP50, flow rate 540.8 g/min

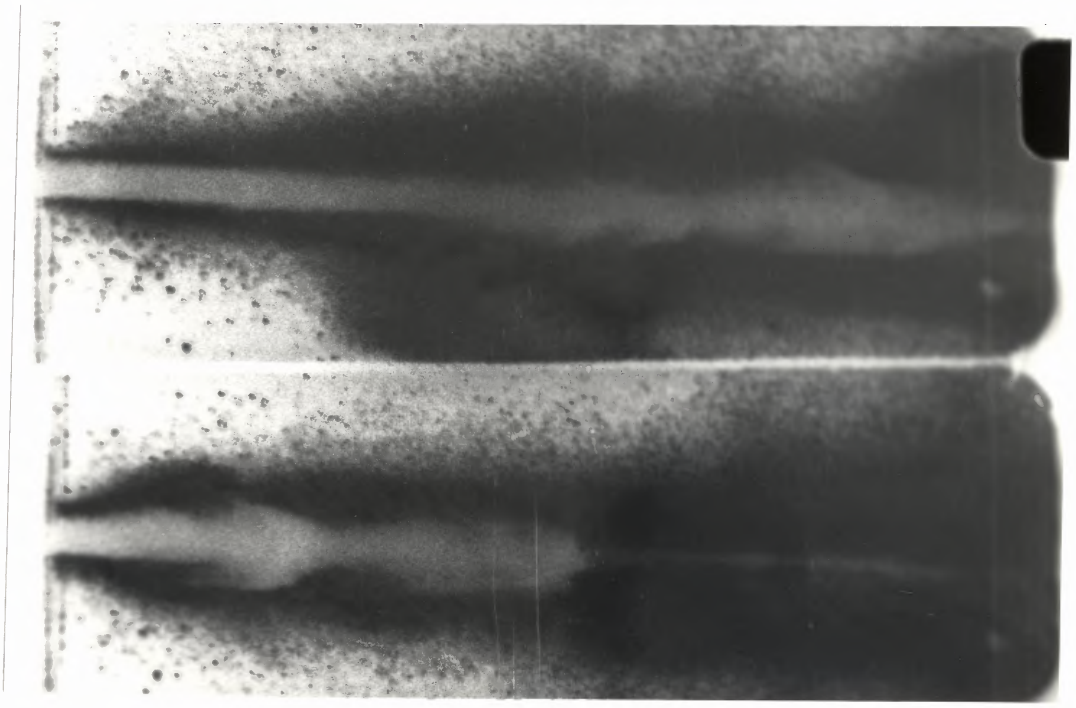

(b) Nozzle d=0.254, D=0.762 mm, HP50, flow rate 540.8 g/min

Figure C.4 For caption please see the next page

(c) Nozzle d=0.254, D=2.362 mm, HP50, flow rate 540.8 g/min

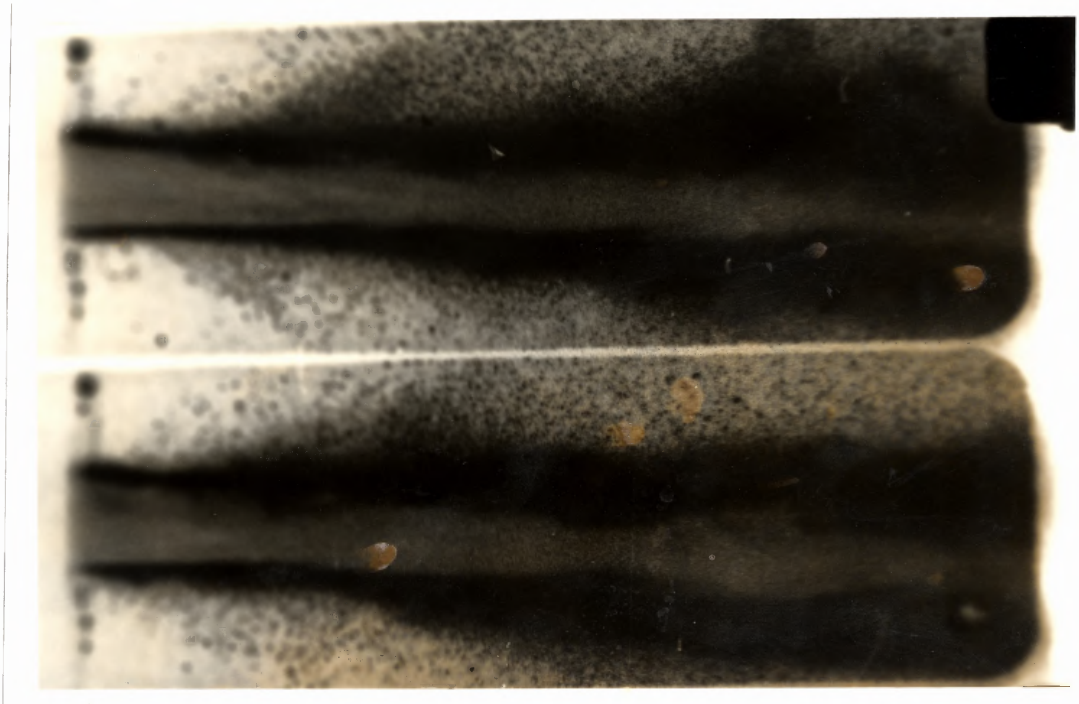

(d) Nozzle d=0.254, D=2.362 mm, HP220, flow rate 318.5 g/min

Figure C.4 AWJ Shows the Particles Accumulation and the Effect of Abrasive on the Jet

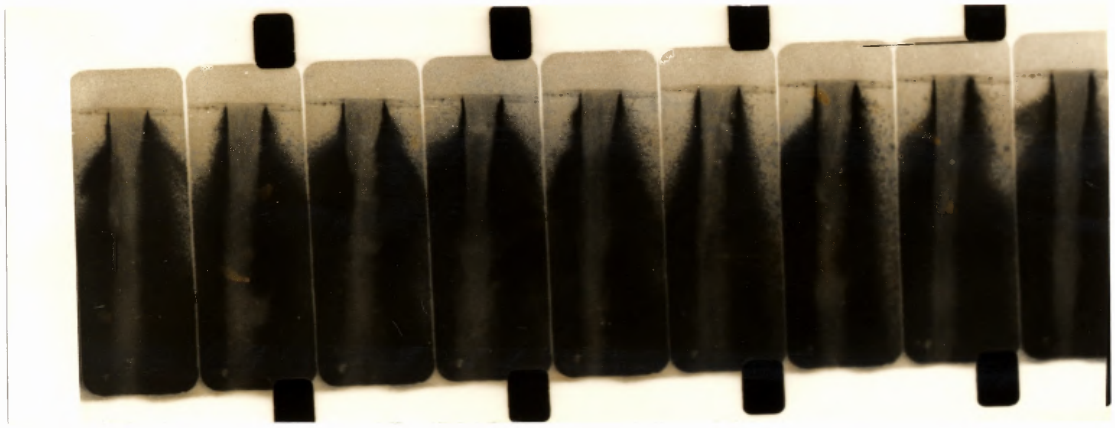

(a) Nozzle d=0.254, D=2.362 mm, HP50, flow rate 540.8 g/min

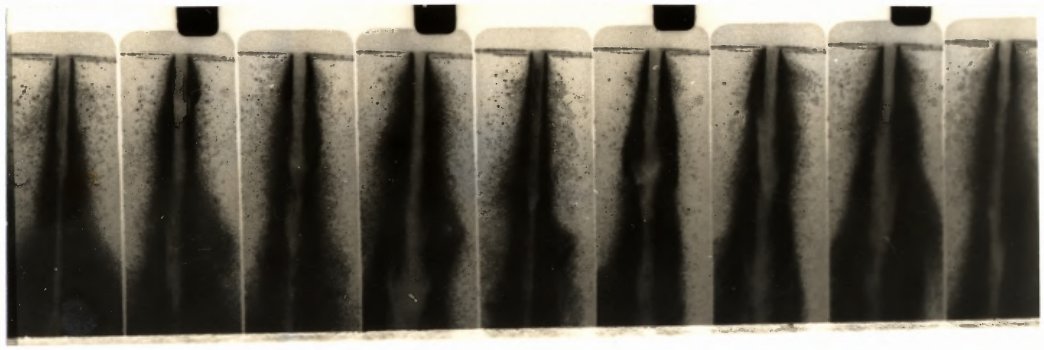

(b) Nozzle d=0.254, D=0.762 mm, HP50, flow rate 540.8 g/min

Figure C.5 Sequential AWJ Apart by the Time 0.125 Milliseconds

Figure C.6 Sequential AWJ Shows the Pulse, Jet Discontinuity and Sudden Expansion

(a) Nozzle d=0.254, D=2.362 mm, HP50, flow rate 540.8 g/min

(b) Nozzle d=0.254, D=2.362 mm, HP220, flow rate 318.5 g/min

Figure C.6 (a)

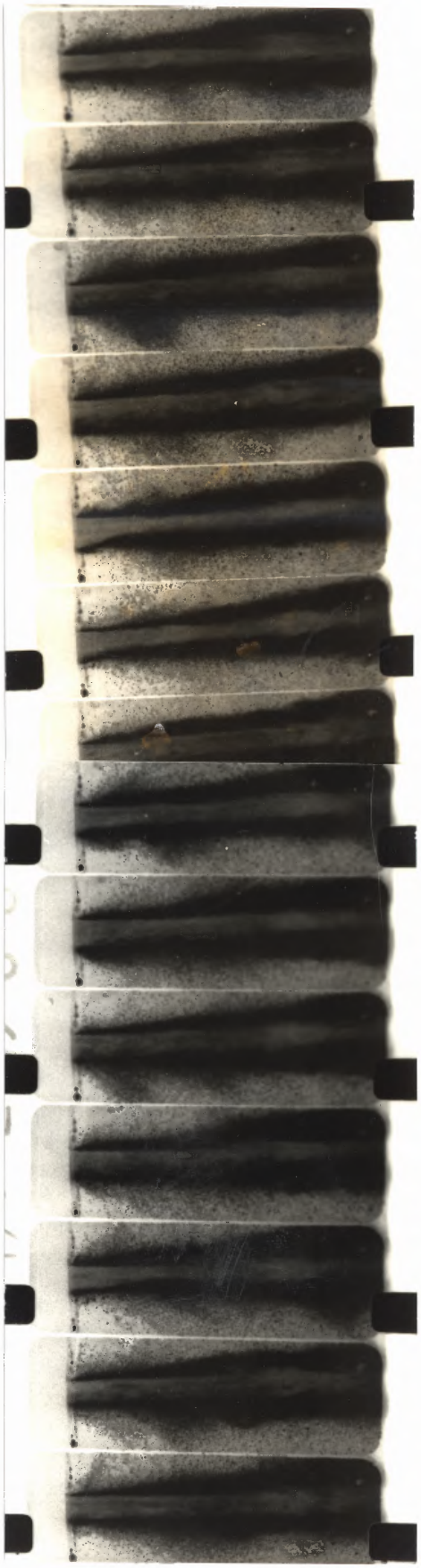

Figure C.6 (b)

APPENDIX D

FIGURES SHOWING COMPUTATIONAL RESULTS OF THE NOZZLES NZ1 and NZ2

Angle t1=10^0 (ψ=0~29.3 cm^2/sec)

Angle t1=30^0 (ψ=0~29.58 cm^2/sec)

Angle t1=60^0 (ψ=0~32.03 cm^2/sec)

Figure D.1a Stream Line Contour (NZ1, d=0.254 mm).
Highest ψ occurs near to the wall.

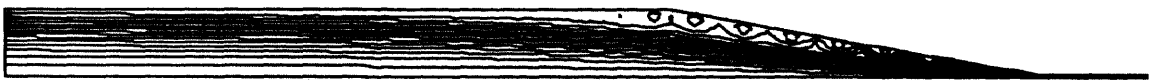

Angle t1=10^0 (ψ=0~8.36 cm^2/sec)

Angle t1=30^0 (ψ=0~8.87 cm^2/sec)

Angle t1=60^0 (ψ=0~10.8 cm^2/sec)

Figure D.1b Stream Line Contour (NZ1, d=0.127 mm).
Highest ψ occurs near to the wall.

Angle t1=10^0 (p=0.106e9~0.651e10 gm/cm-sec^2)

Angle t1=30^0 (p=0.948e8~0.708e10 gm/cm-sec^2)

Angle t1=60^0 (p=-0.273e9~0.667e10 gm/cm-sec^2)

Figure D.2a Pressure Contour (NZ1, d=0.254 mm). Highest p occurs at orifice entrance.

Angle t1=10^0 (p=0.549e8~0.13e11 gm/cm-sec^2)

Angle t1=30^0 (p=0.267e9~0.1641e11 gm/cm-sec^2)

Angle t1=60^0 (p=0.589e9~0.197e11 gm/cm-sec^2)

Figure D.2b Pressure Contour (NZ1, d=0.127 mm). Highest p occurs at orifice entrance.

Angle t1=10^0 (μ_t=0.5e-3~8.15 gm/cm-sec)

Angle t1=30^0 (μ_t=0.5e-3~8.89 gm/cm-sec)

Angle t1=60^0 (μ_t=0.48e-3~8.007 gm/cm-sec)

Figure D.3a Eddy Viscosity Contour (NZ1, d=0.254 mm). Highest μ_t occurs before exit.

Angle t1=10^0 (μ_t=0.26e-6~4.02 gm/cm-sec)

Angle t1=30^0 (μ_t=0.608e-7~5.82 gm/cm-sec)

Angle t1=60^0 (μ_t=0.5e-3~7.84 gm/cm-sec)

Figure D.3b Eddy Viscosity Contour (NZ1, d=0.127 mm). Highest μ_t occurs before exit.

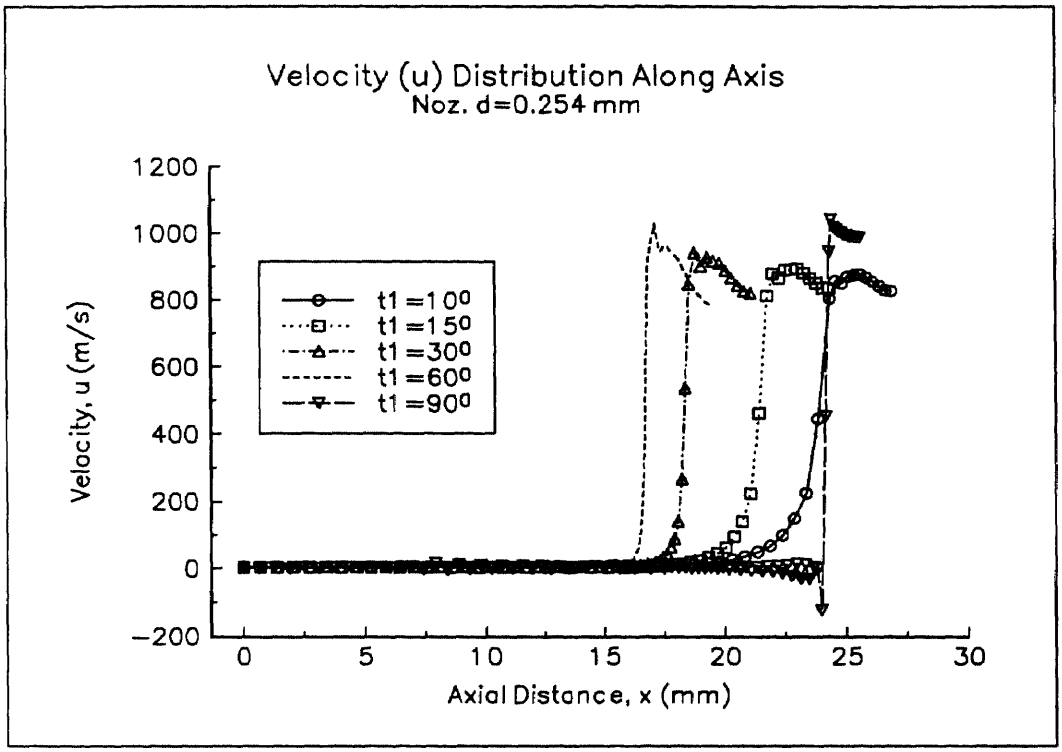

(a)

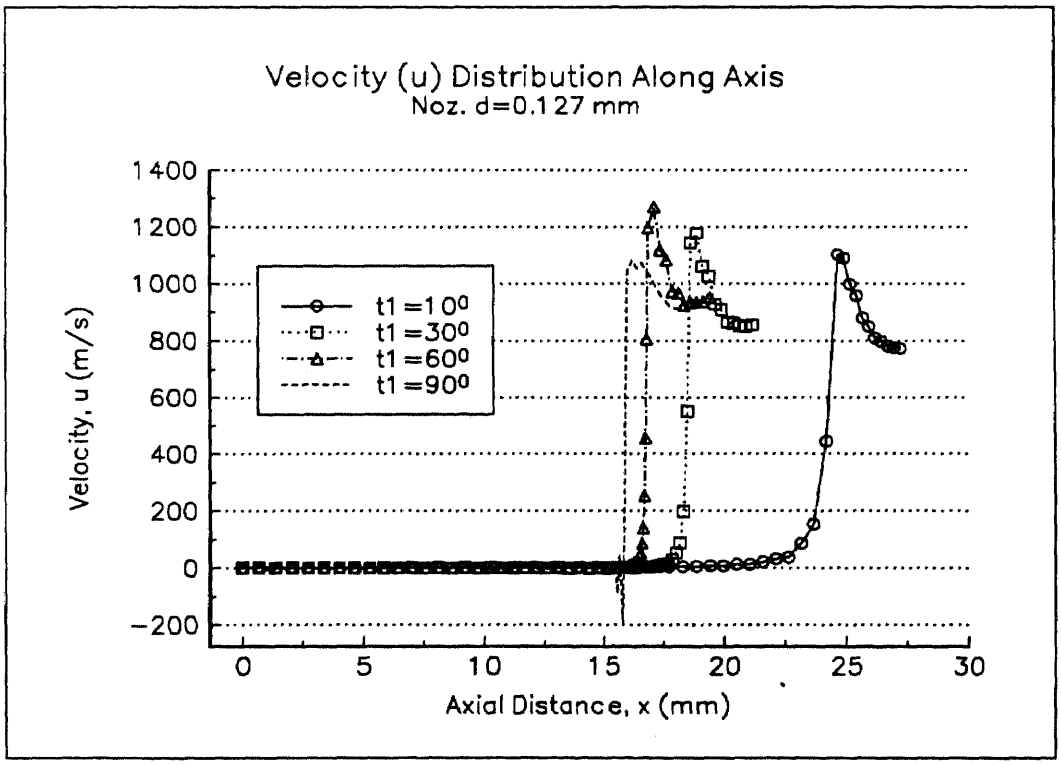

(b)

Figure D.4 Centerline Velocity Distribution of the Nozzle NZ1

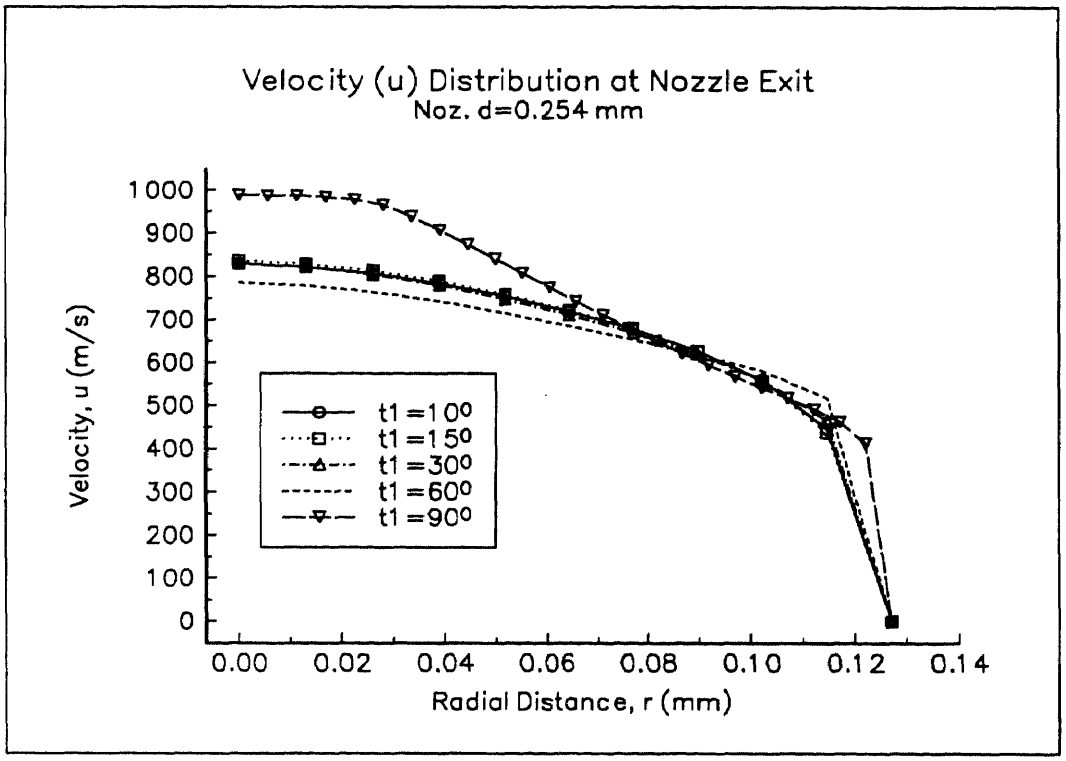

(a)

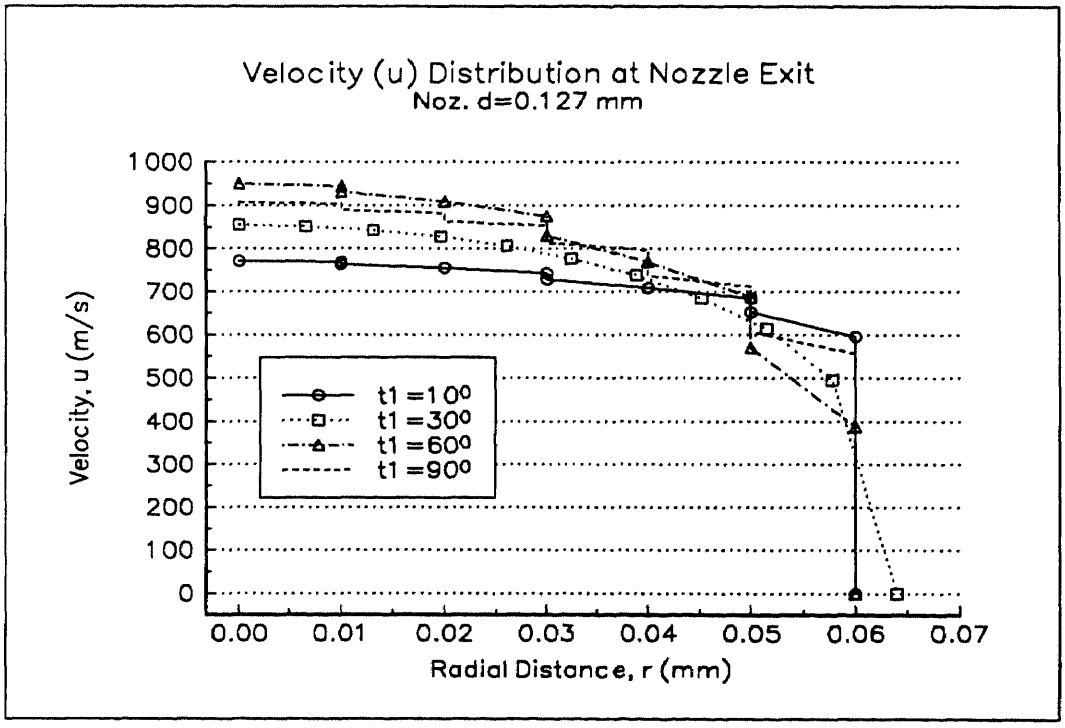

(b)

Figure D.5 Velocity Distribution at the Exit of the Nozzle NZ1

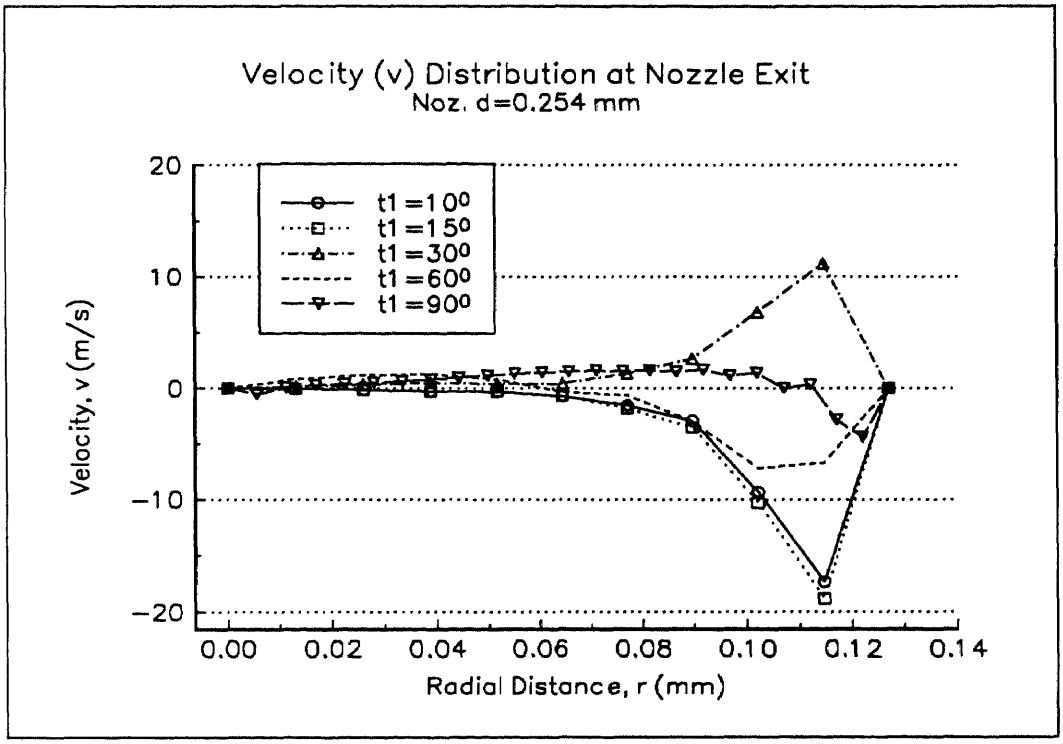

(a)

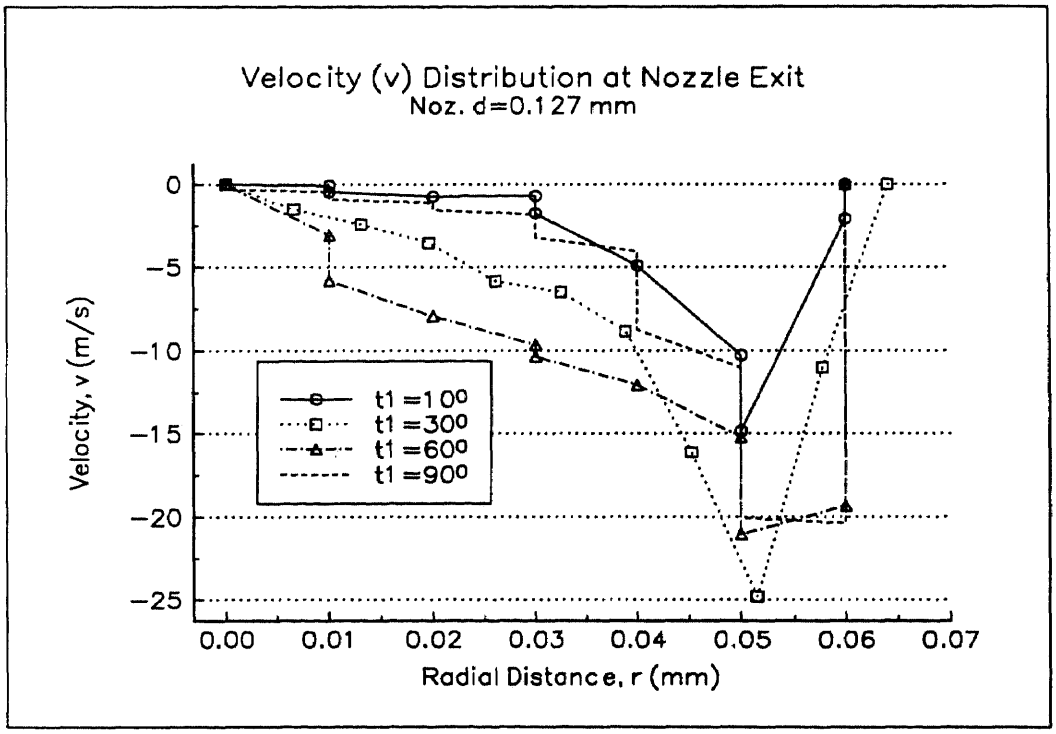

(b)

Figure D.6 Velocity (v) Distribution at the Exit of the Nozzle NZ1

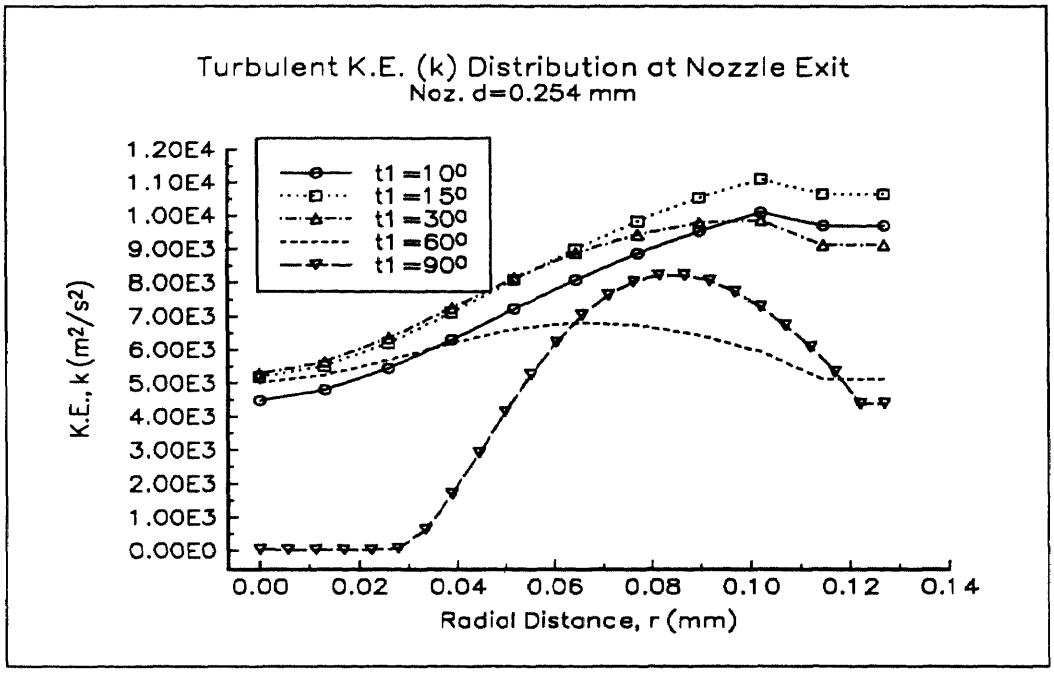

(a)

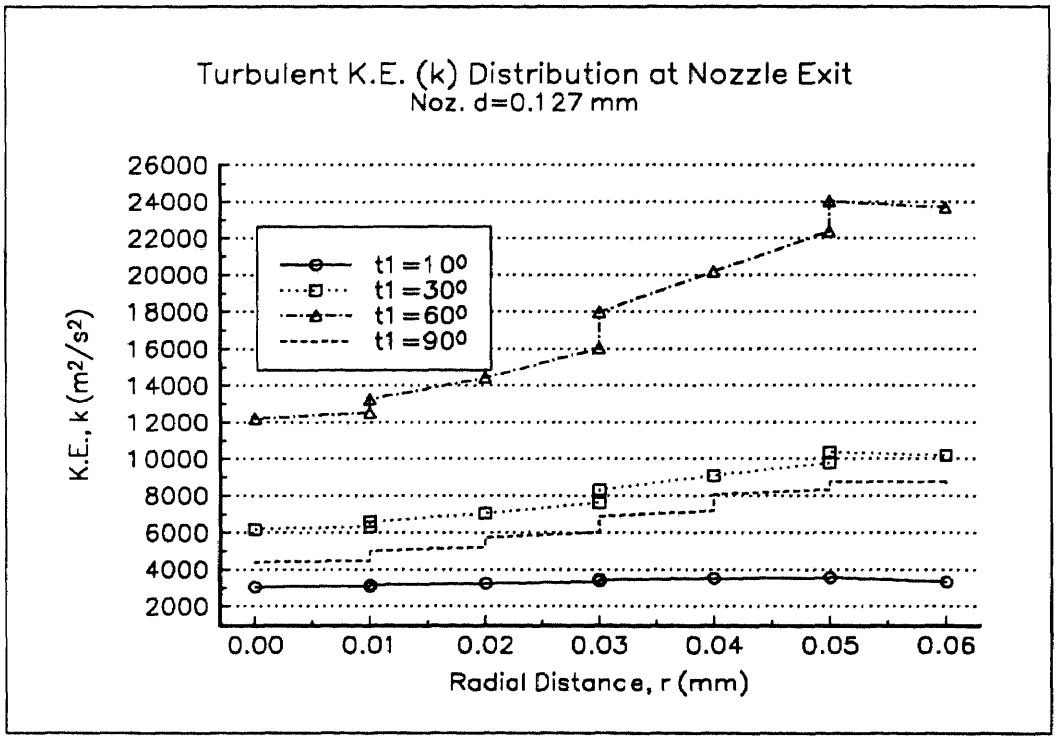

(b)

Figure D.7 Turbulent Kinetic Energy Distribution at the Exit of the Nozzle NZ1

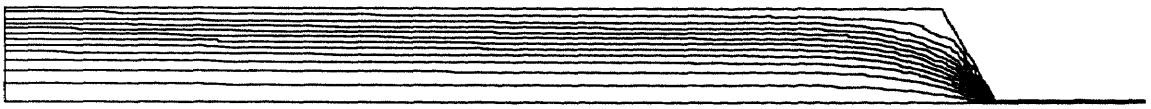

Nozzle d=0.127 mm (ψ=0~10.8 cm^2/s)

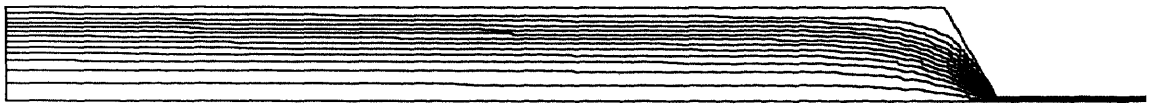

Nozzle d=0.178 mm (ψ=0~18.5 cm^2/s)

Nozzle d=0.254 mm (ψ=0~32.03 cm^2/s)

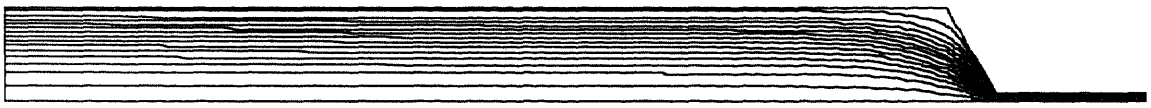

Nozzle d=0.305 mm (ψ=0~38.66 cm^2/s)

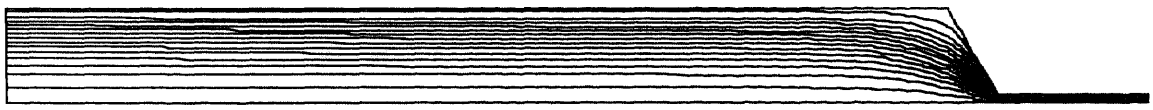

Nozzle d=0.356 mm (ψ=0~39.06 cm^2/s)

Figure D.8a Stream Line Contour (NZ1, Angle t1= 60^0).
Highest ψ occurs near to the wall.

Nozzle d=0.127 mm (p=0.589e9~0.197e11 gm/cm-s^2)

Nozzle d=0.178 mm (p=0.12e9~0.108e11 gm/cm-s^2)

Nozzle d=0.254 mm (p=-0.273e9~0.667e10 gm/cm-s^2)

Nozzle d=0.305 mm (p=-0.282e9~0.442e10 gm/cm-s^2)

Nozzle d=0.356 mm (p=-0.289e9~0..451e10 gm/cm-s^2)

Figure D.8b Pressure Contour (NZ1, Angle t1= 60^0).
Highest p occurs before orifice entrance.

Nozzle d=0.127 mm (μ_t=0.5e-3~7.84 gm/cm-s)

Nozzle d=0.178 mm (μ_t=0.31e-3~7.516 gm/cm-s)

Nozzle d=0.254 mm (μ_t=0.48e-3~8.007 gm/cm-s)

Nozzle d=0.305 mm (μ_t=0.4415e-3~9.66 gm/cm-s)

Nozzle d=0.356 mm (μ_t=0.417e-3~9.69 gm/cm-s)

Figure D.8c Eddy Viscosity Contour (NZ1, Angle t1= 60^0).
Highest μ_t occurs before the exit of the nozzle.

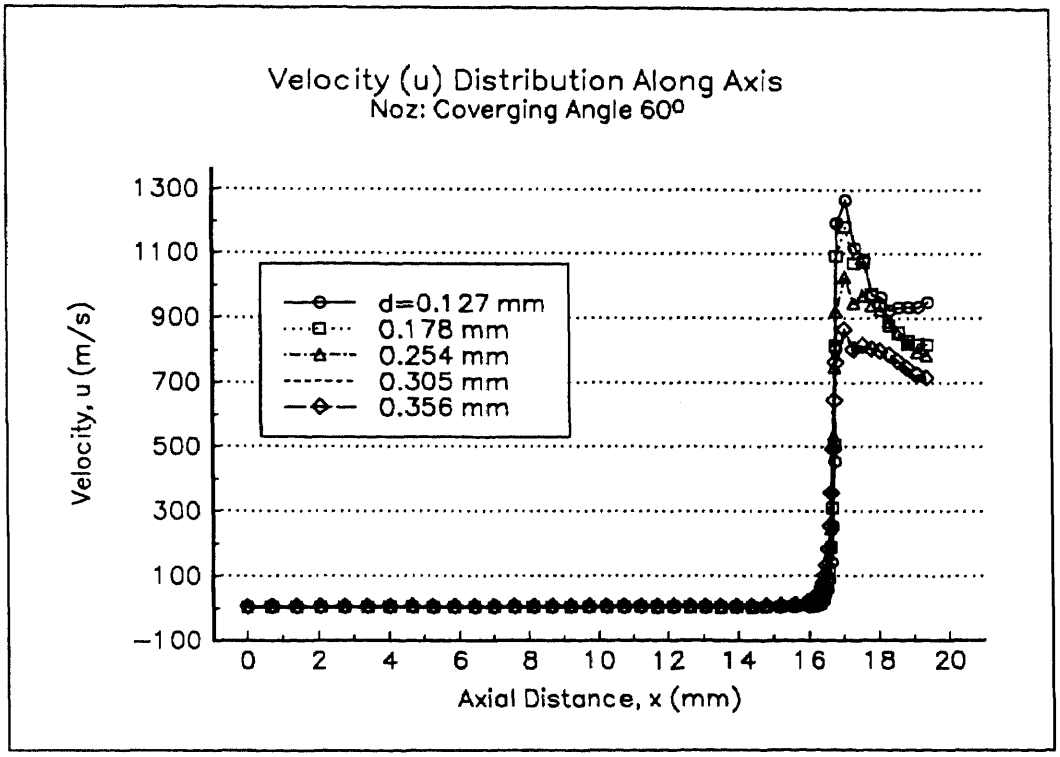

Figure D.9 Centerline Velocity (u) Distribution of the Nozzle NZ1 ($t1=60^0$)

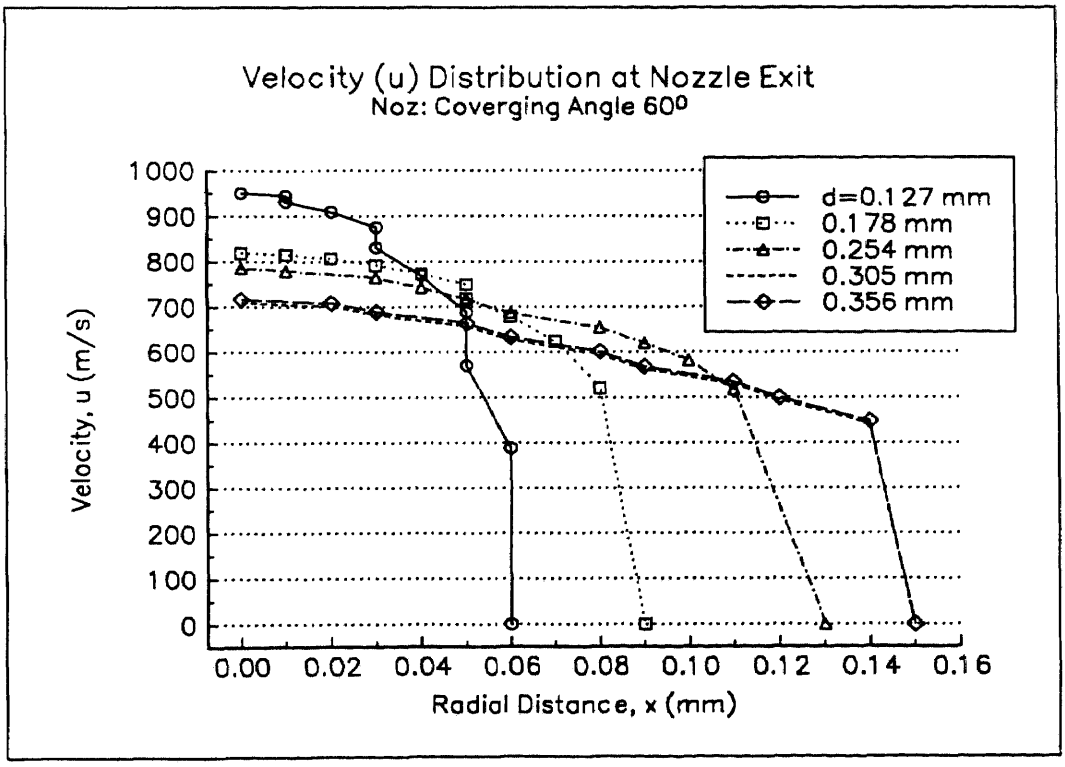

Figure D.10 Velocity (u) Distribution at the Exit of the Nozzle NZ1 ($t1=60^0$)

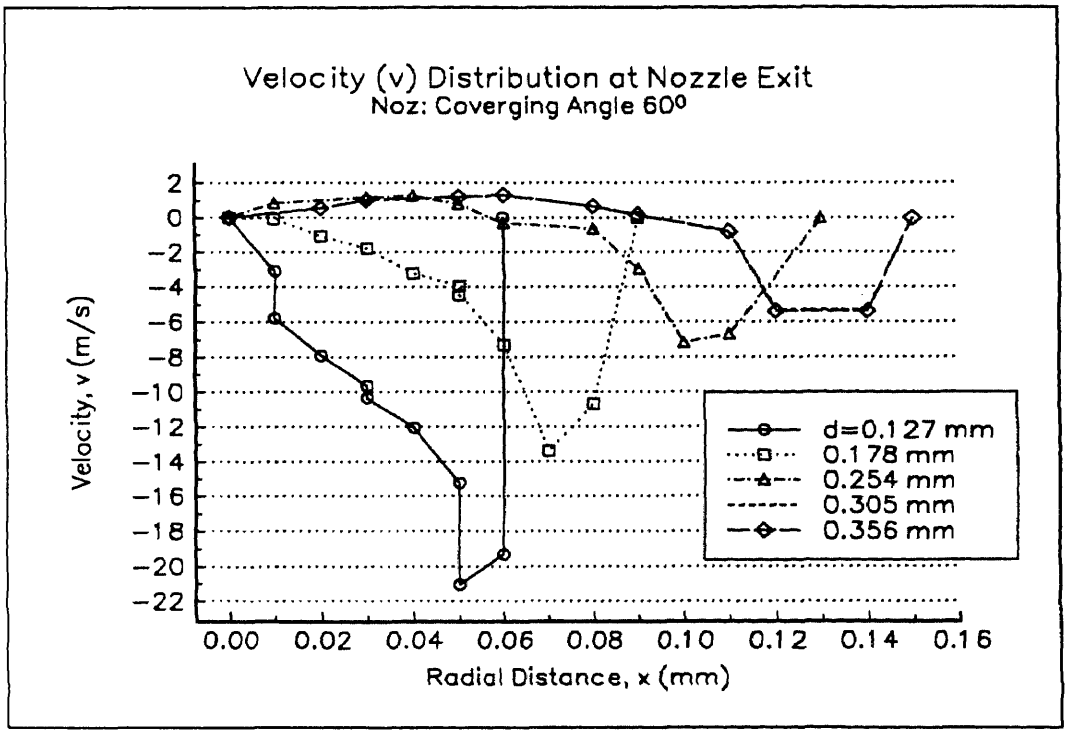

Figure D.11 Velocity (v) Distribution at the Exit of the Nozzle NZ1 ($t1=60^0$)

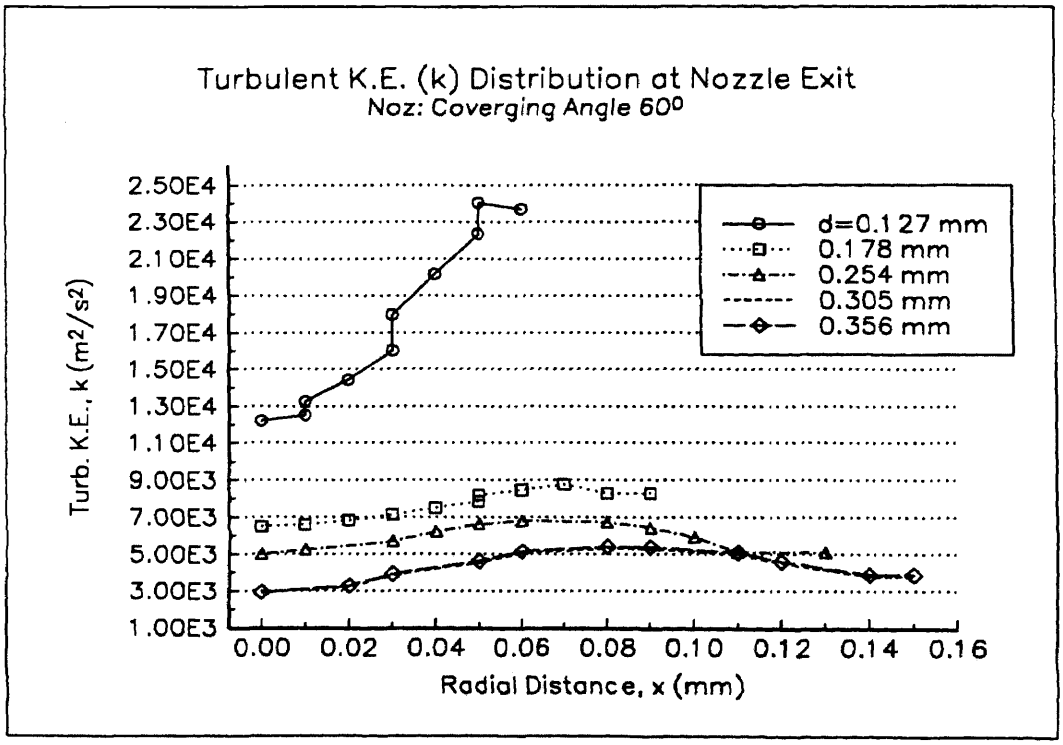

Figure D.12 Turbulent Kinetic Energy Distribution at the Exit of the Nozzle NZ1 ($t1=60^0$)

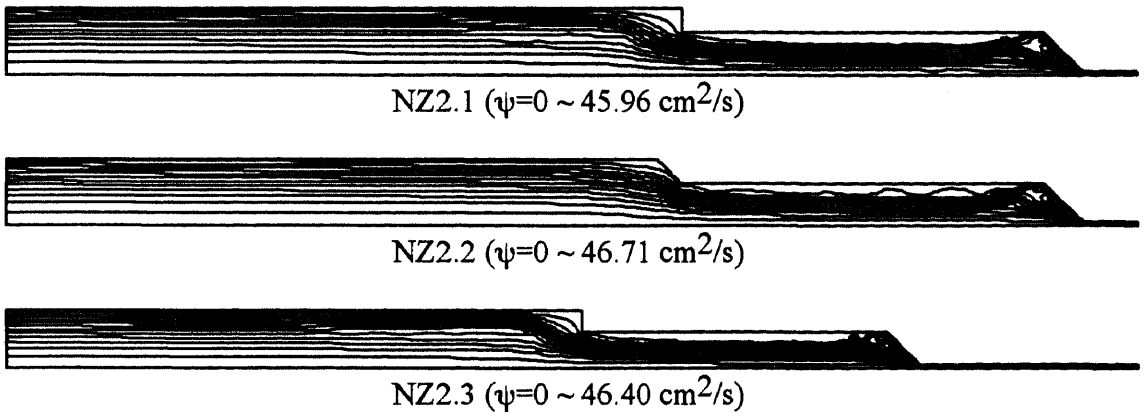

Figure D.13 Streamline Contour (Nozzle NZ2). Highest ψ occurs near to the wall.

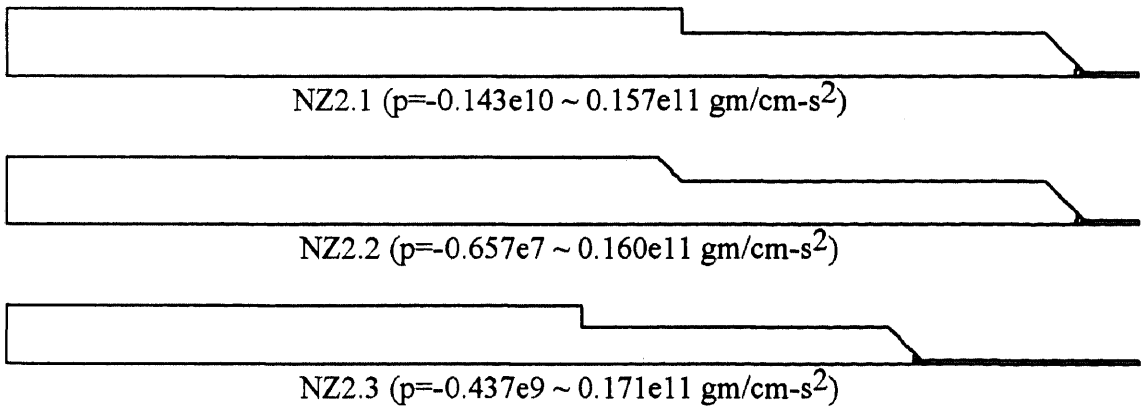

Figure D.14 Pressure Contour (Noz. NZ2). Highest p occurs at the orifice entrance.

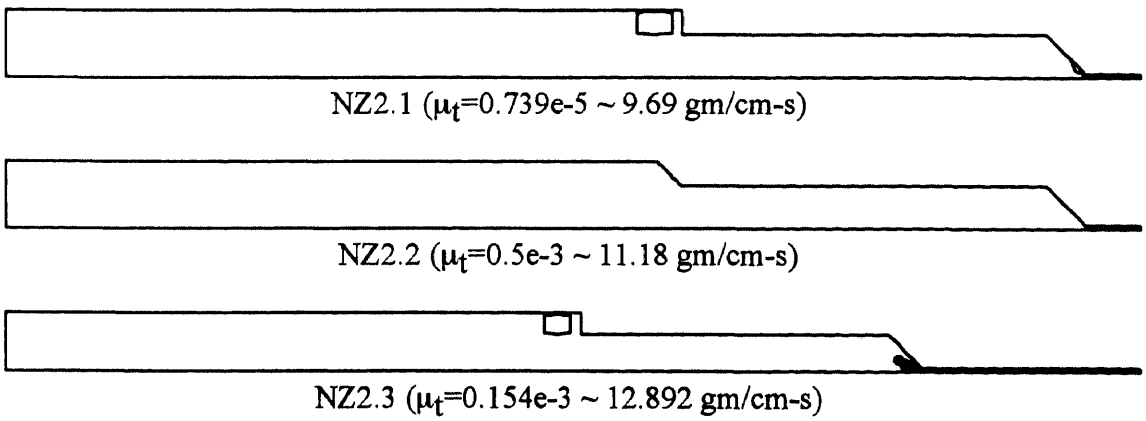

Figure D.15 Eddy Viscosity Contour (Nozzle NZ2).
Highest μ_t occurs at the exit of the nozzle.

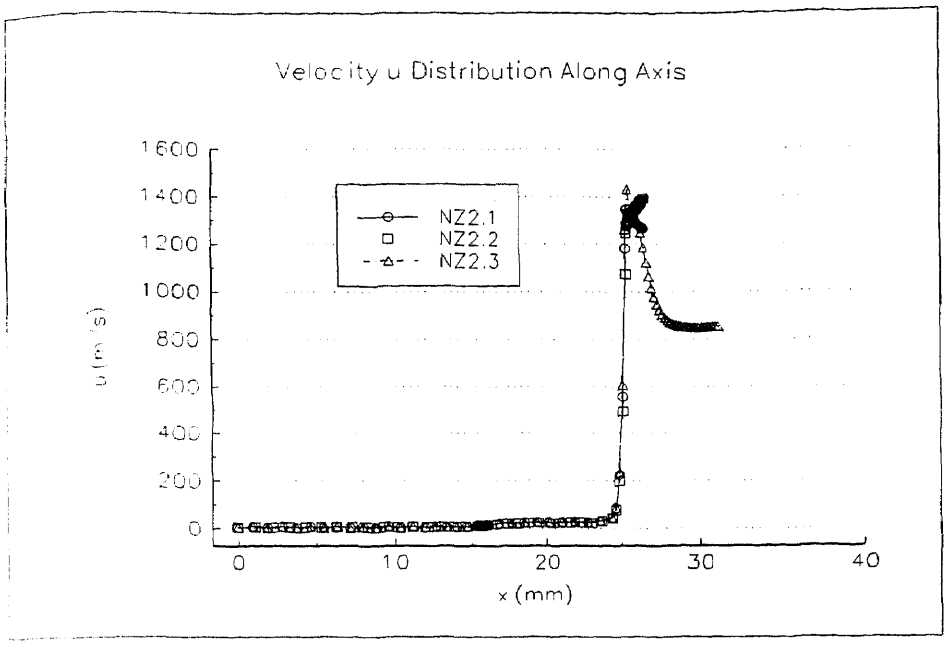

Figure D.16 Centerline Velocity (u) Distribution of the Nozzle NZ2

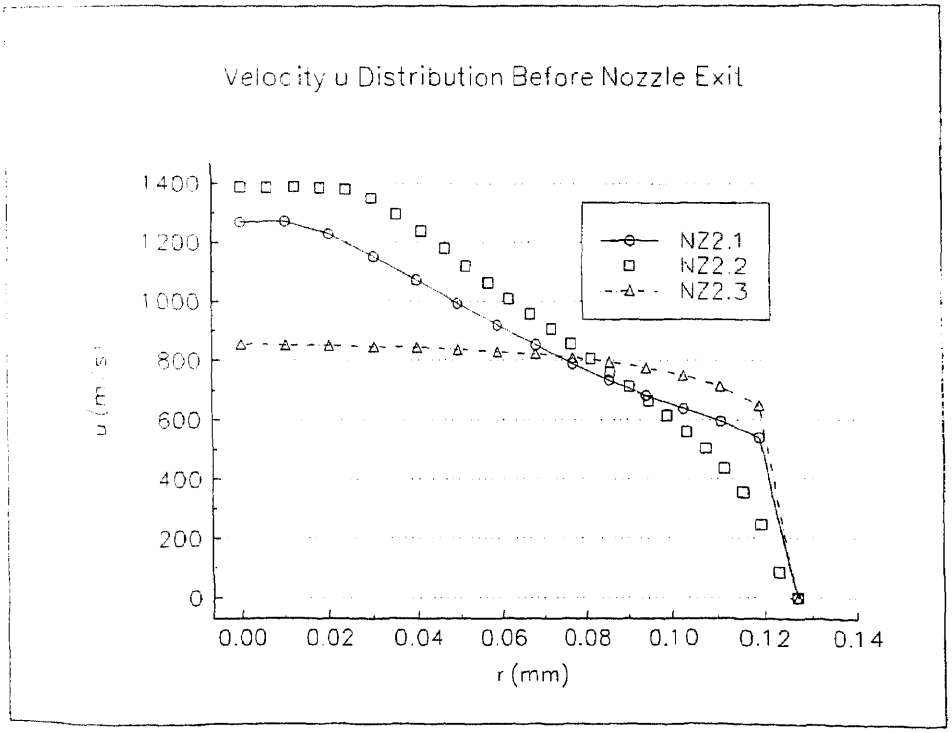

Figure D.17 Velocity (u) Distribution at the Exit of the Nozzle NZ2

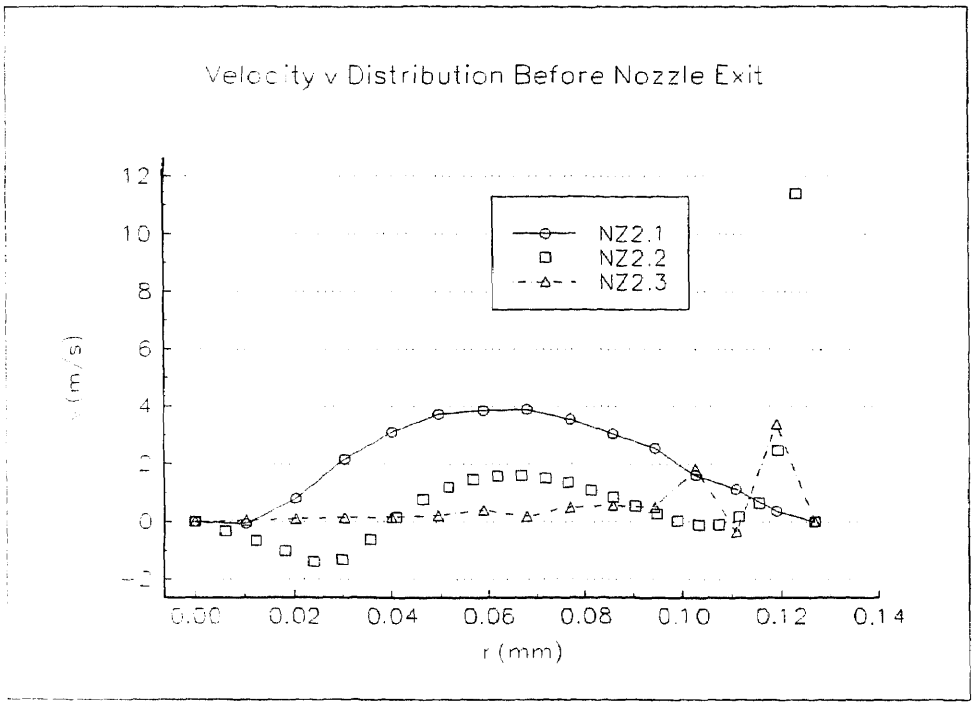

Figure D.18 Velocity (v) Distribution at the Exit of the Nozzle NZ2

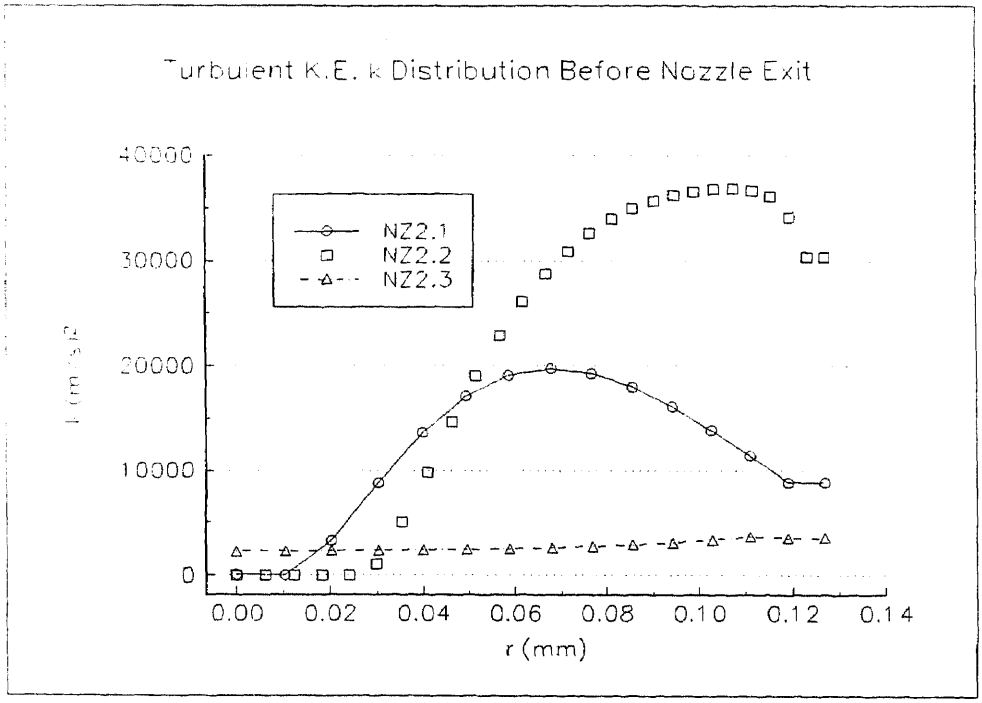

Figure D.19 Turbulent Kinetic Energy Distribution at the Exit of the Nozzle NZ2

APPENDIX E

FIGURES SHOWING COMPUTATIONAL RESULTS OF THE NOZZLES NZ3, NZ4 and NZ5

NZ3.1 (ψ= -0.071 ~ 109.27 cm^2/s)

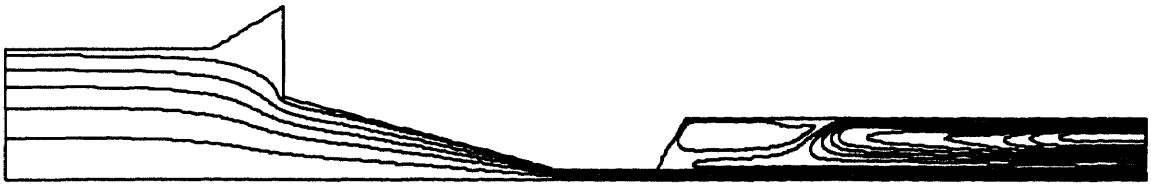

NZ3.2 (ψ= 0 ~ 99.35 cm^2/s)

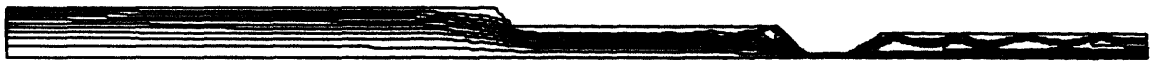

NZ3.3 (ψ= 0 ~ 60.93 cm^2/s)

Figure E.1 Stream Line Contour (Nozzle NZ3).
Highest ψ occurs at the eye of circulation.

NZ3.1 (p=-0.75e8 ~ 0.763e10 gm/cm-s^2)

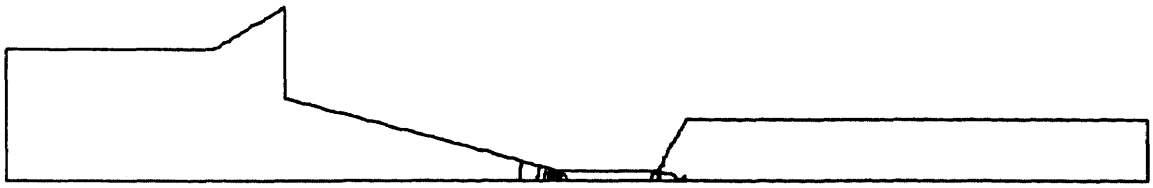

NZ3.2 (p=-0.605e8 ~ 0.412e10 gm/cm-s^2)

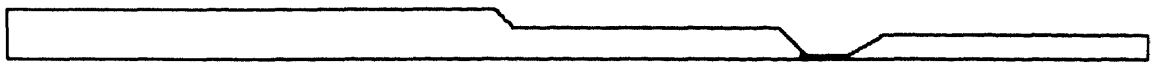

NZ 3.3 (p=-0.311e9 ~ 0.154e11 gm/cm-s^2)

Figure E.2 Pressure Contour (Nozzle NZ3). Highest p occurs at orifice entrance.

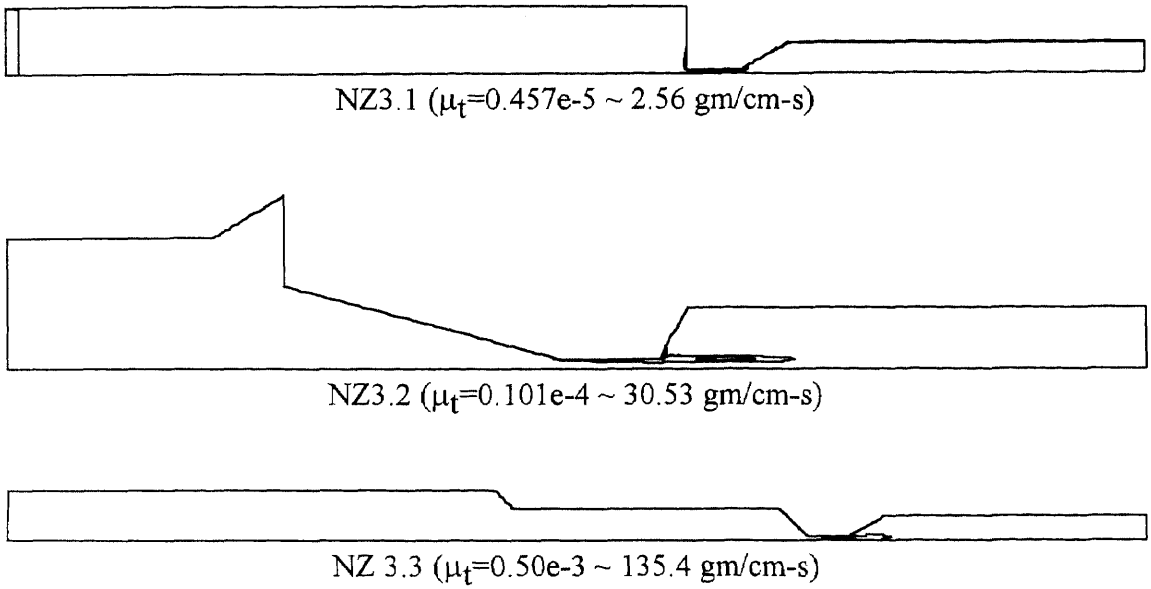

Figure E.3 Eddy Viscosity Contour (Nozzle NZ3).
Highest μ_t occurs at the eye of circulation.

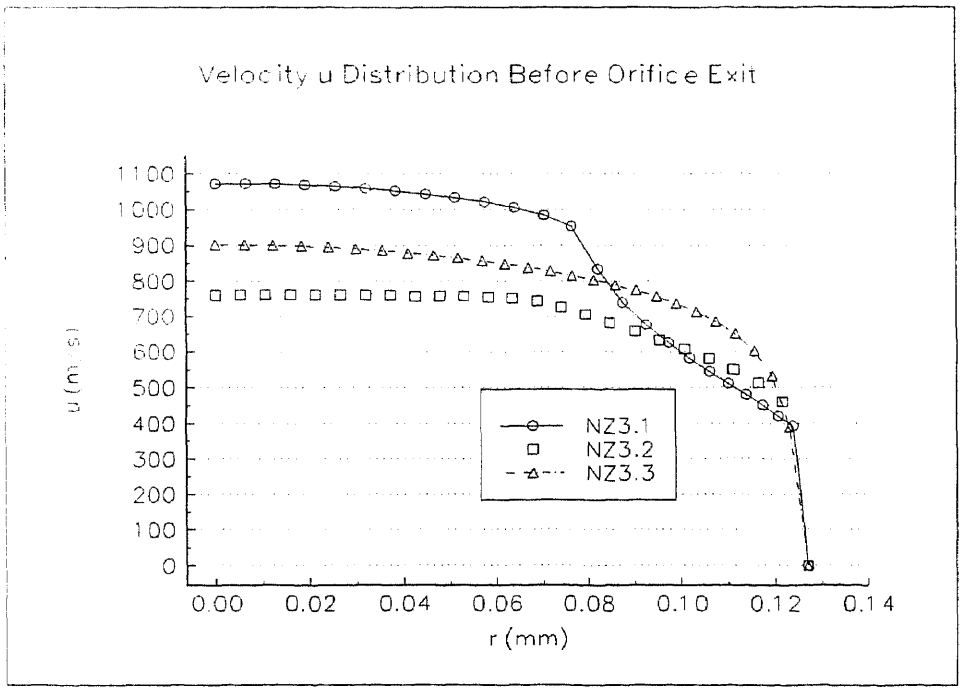

Figure E.4 Velocity (u) Distribution at the Orifice Exit of the Nozzle NZ3

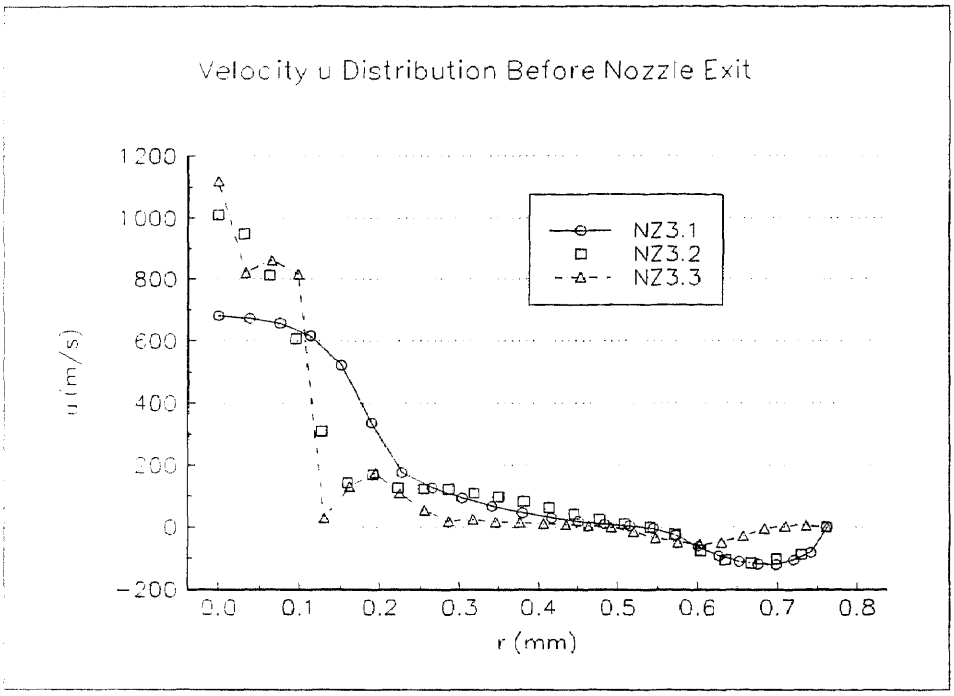

Figure E.5 Velocity (u) Distribution at the Exit of the Nozzle NZ3

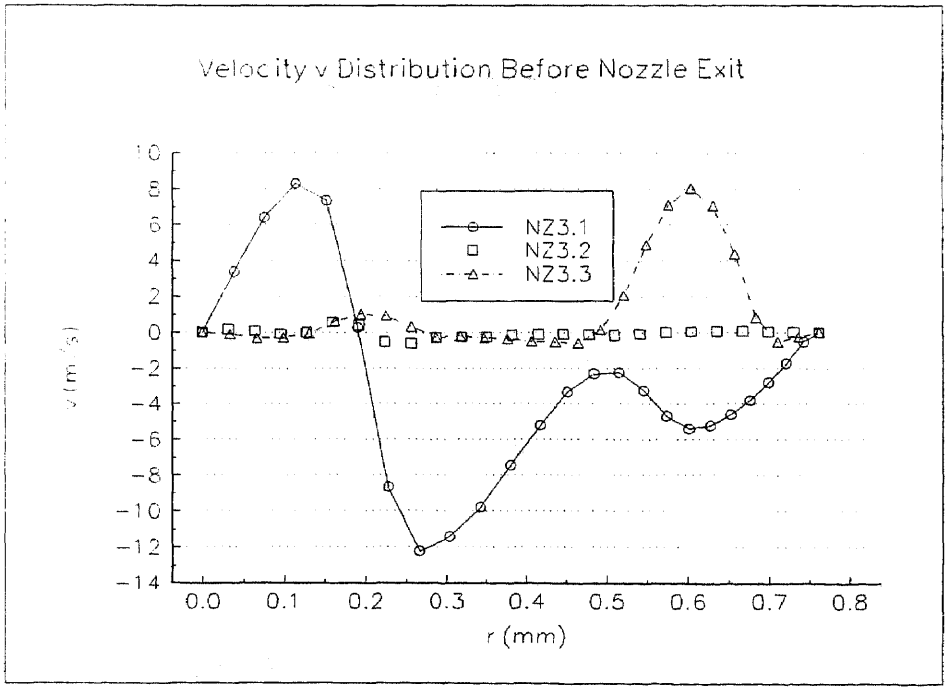

Figure E.6 Velocity (v) Distribution at the exit of the Nozzle NZ3

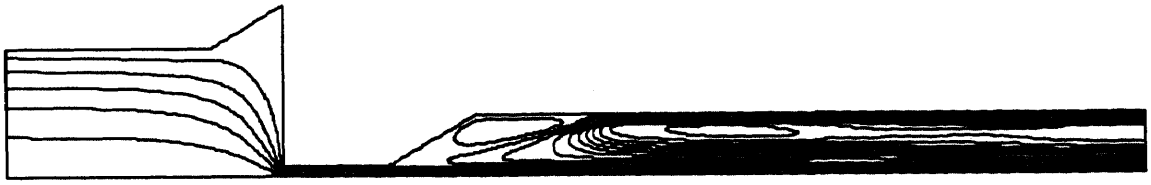

NZ4.1 (ψ=0 ~ 93.5 cm^2/s)

NZ4.2 (ψ=0 ~ 48.5.5 cm^2/s)

NZ4.3 (ψ=0 ~ 54.07 cm^2/s)

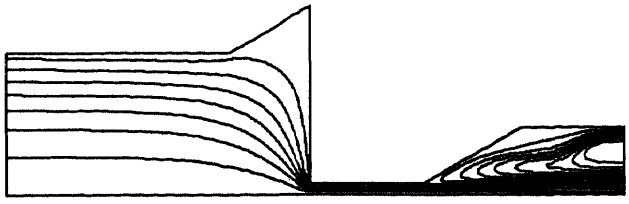

NZ4.4 (ψ=0 ~ 68.48 cm^2/s)

Figure E.7 Stream Line Contour (Nozzle NZ4).
Highest ψ occurs at the eye of circulation.

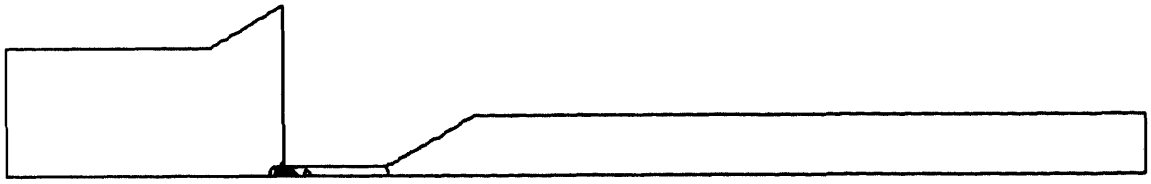

NZ4.1 (p= -0.40e8 ~ 0.57e10 gm/cm-s^2)

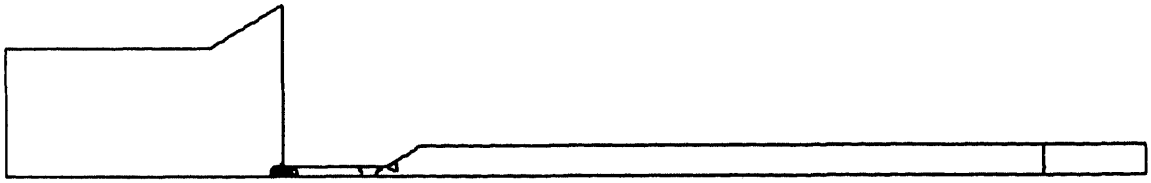

NZ4.2 (p= -0.225e9 ~ 0.724e10 gm/cm-s^2)

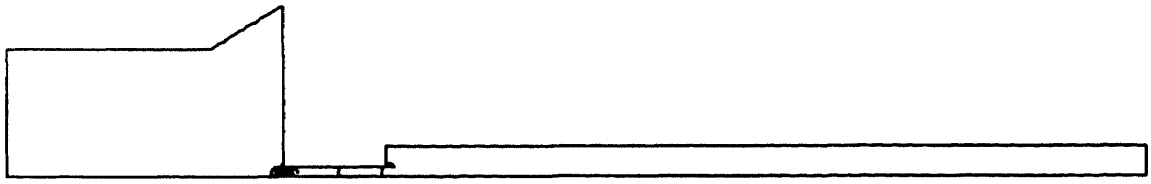

NZ4.3 (p= -0.442e9 ~ 0.702e10 gm/cm-s^2)

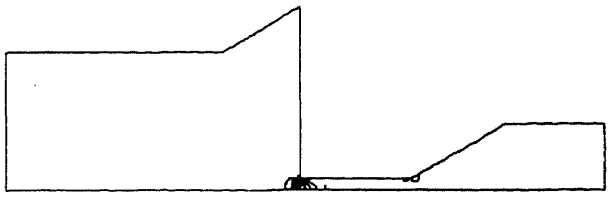

NZ4.4 (p= -0.227e9 ~ 0.553e10 gm/cm-s^2)

Figure E.8 Pressure Contour Plot (Nozzle NZ4).
Highest p occurs at the entrance of the orifice.

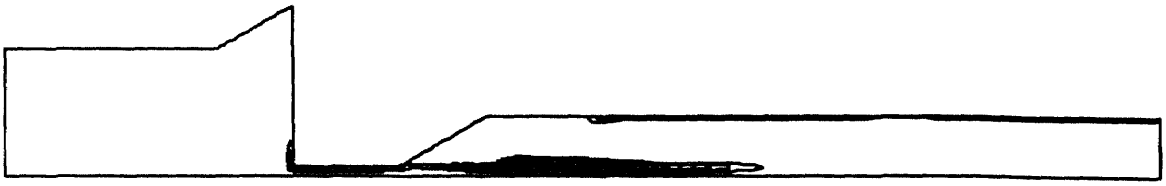

NZ4.1 (μ_t= 0.225e-5 ~ 6.90 gm/cm-s)

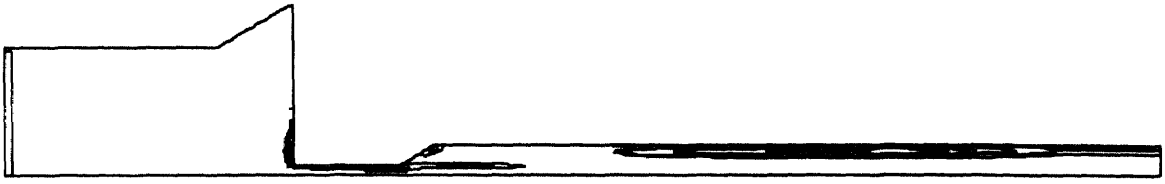

NZ4.2 (μ_t= 0.985e-5 ~ 3.95 gm/cm-s)

NZ4.3 (μ_t= 0.115e-4 ~ 32.04 gm/cm-s)

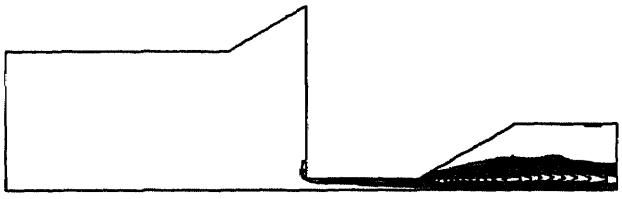

NZ4.4 (μ_t= 0.5e-3 ~ 16.20 gm/cm-s)

Figure E.9 Eddy viscosity Contour Plot (Nozzle NZ4).
Highest μ_t occurs at the exit of orifice.

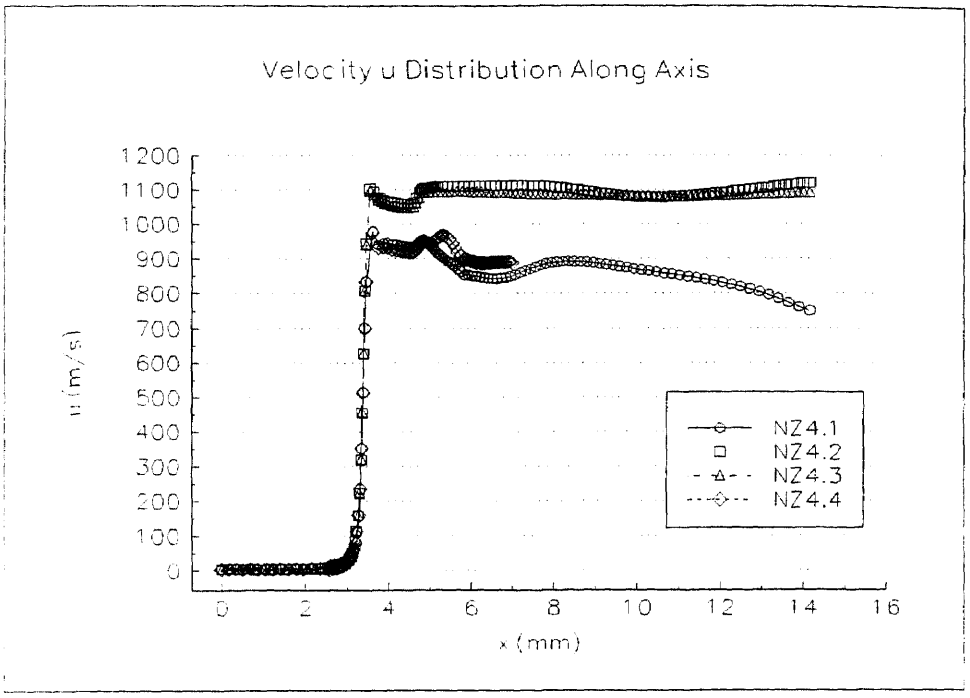

Figure E.10 Centerline Velocity (u) Distribution of the Nozzle NZ4

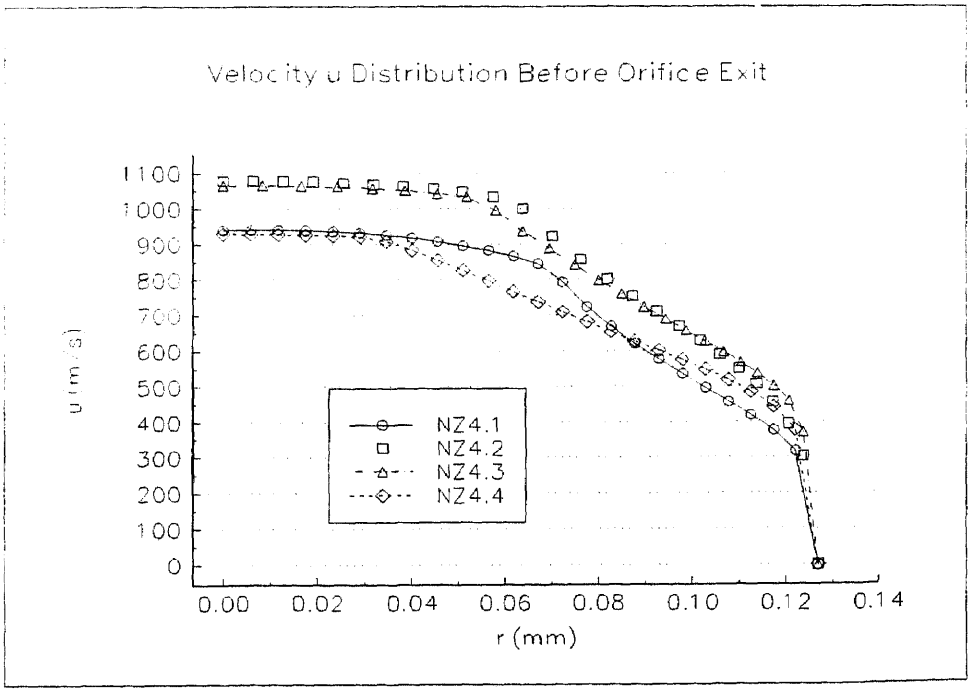

Figure E.11 Velocity (u) at the Orifice Exit of the Nozzle NZ4

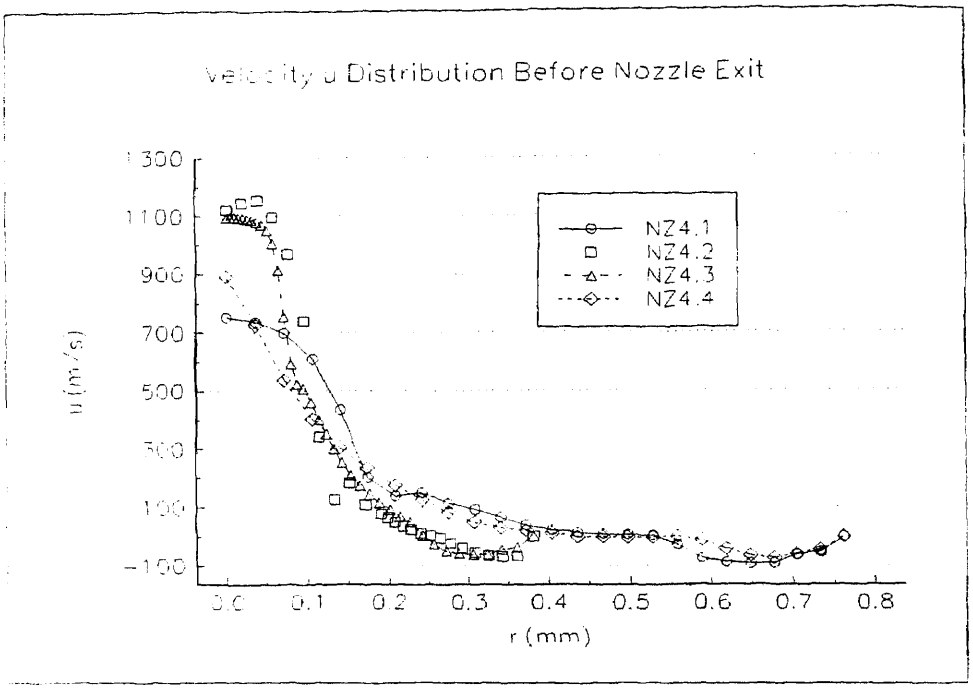

Figure E.12 Velocity (u) Distribution at the Exit of the Nozzle NZ4

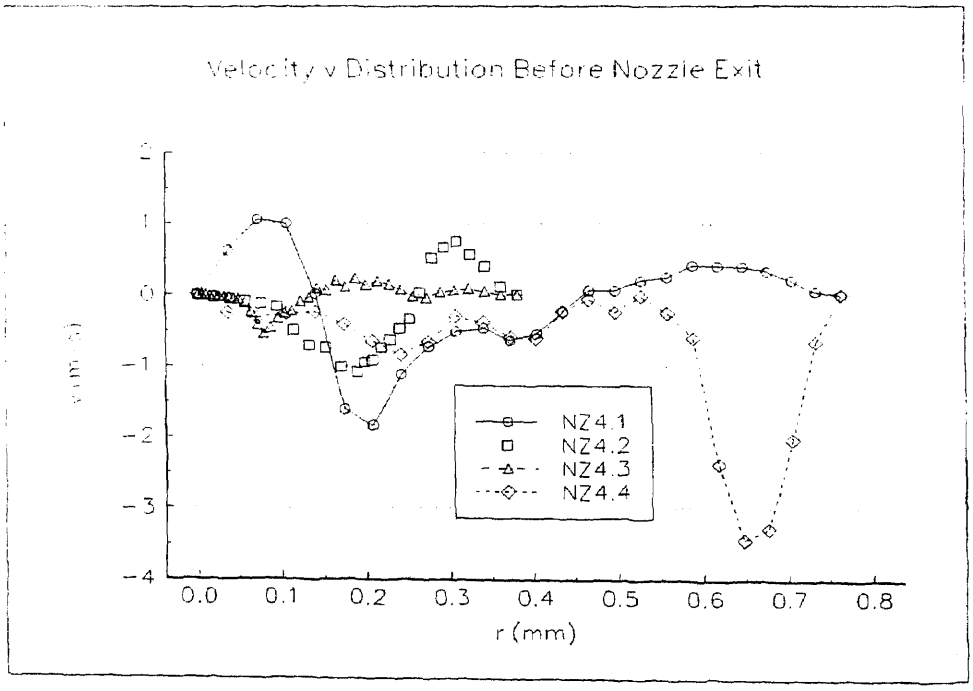

Figure E.13 Velocity (v) Distribution at the Exit of the Nozzle NZ4

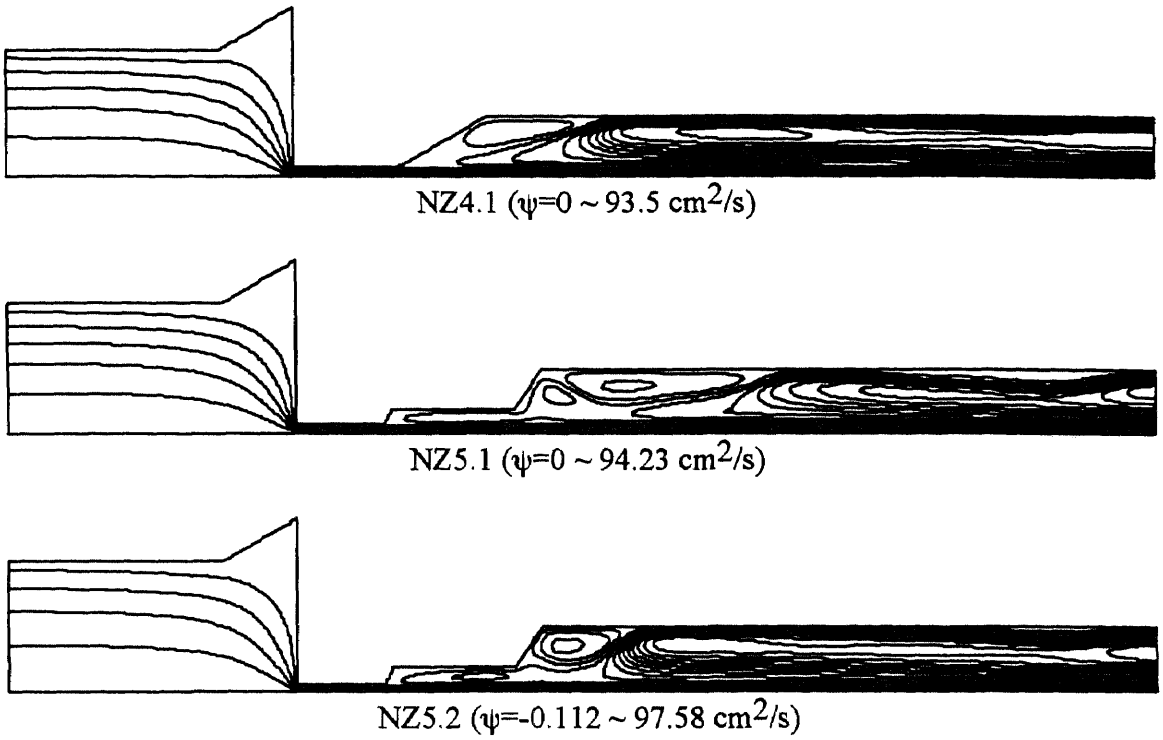

Figure E.14 Stream Line Contour Plot (Nozzles NZ4 & NZ5).
Highest ψ occurs at the eye of circulation.

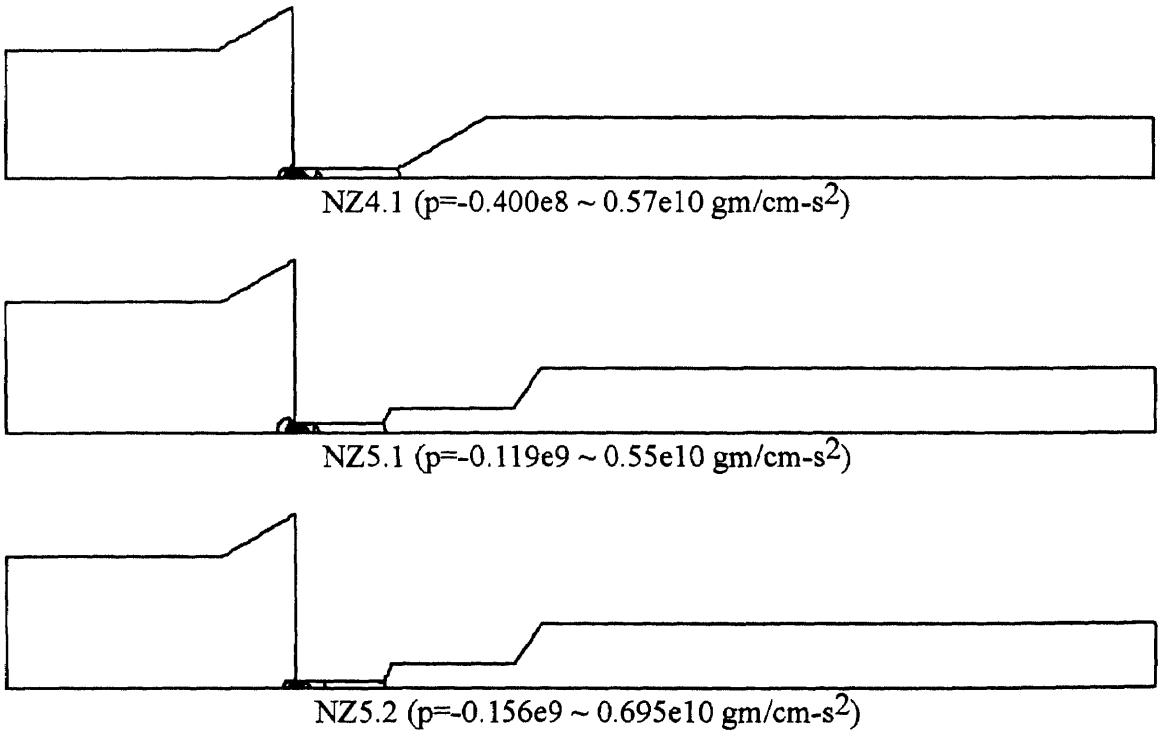

Figure E.15 Pressure Contour Plot (Nozzles NZ4 & NZ5).

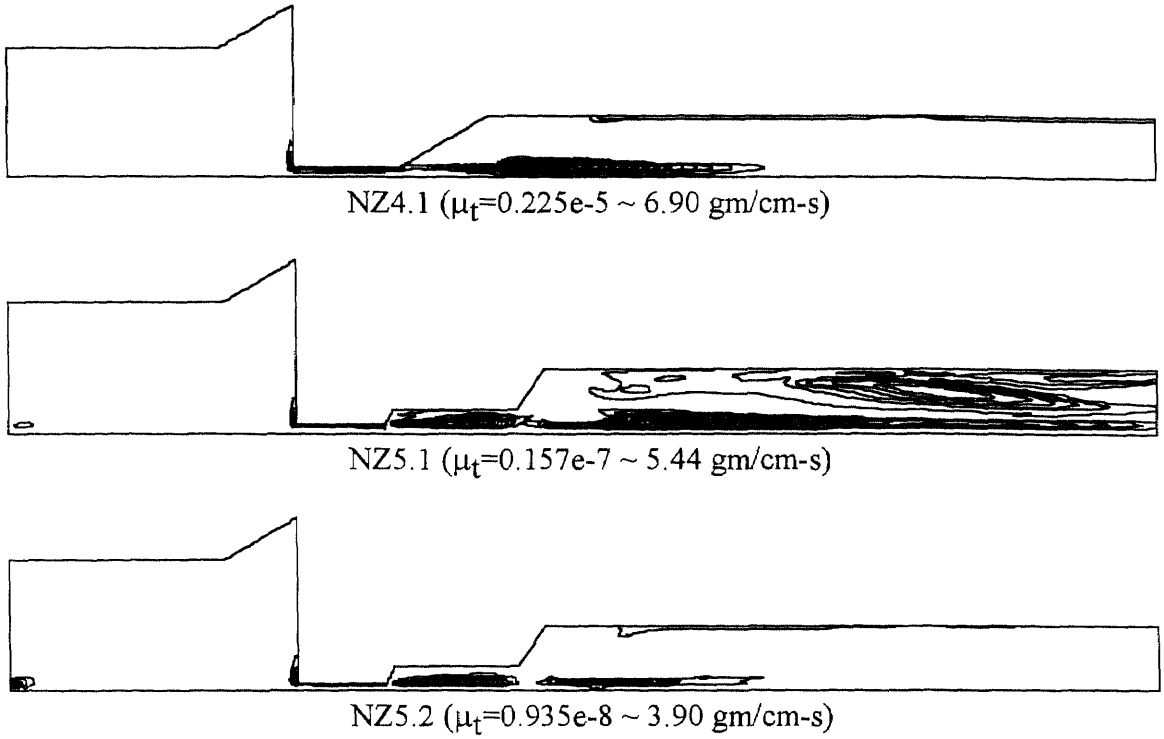

Figure E.16 Eddy Viscosity Contour Plot (Nozzles NZ4 & NZ5).
Highest μ_t occurs at orifice exit.

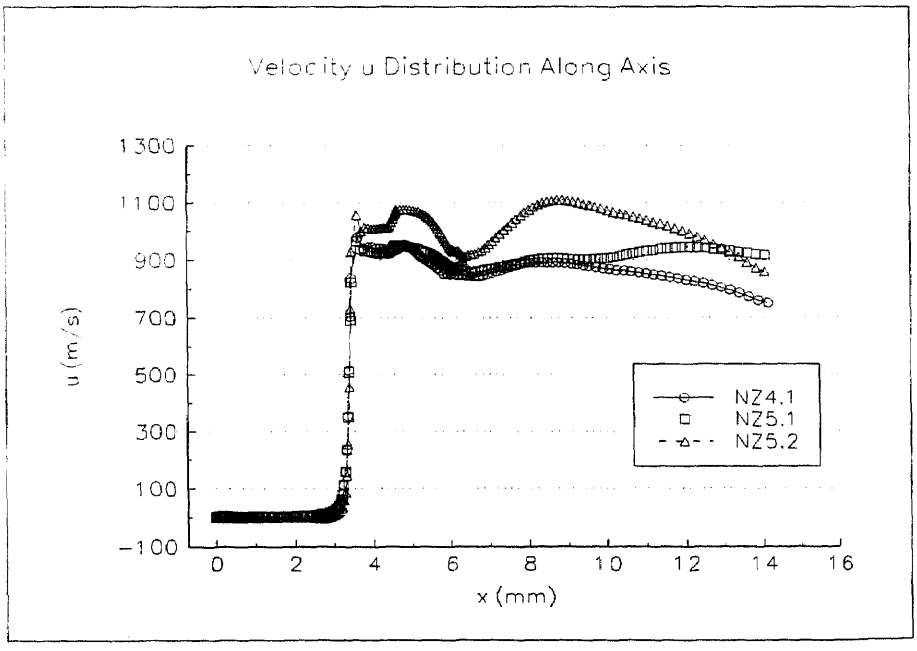

Figure E.17 Centerline Velocity (u) Distribution of the Nozzles NZ4 and NZ5

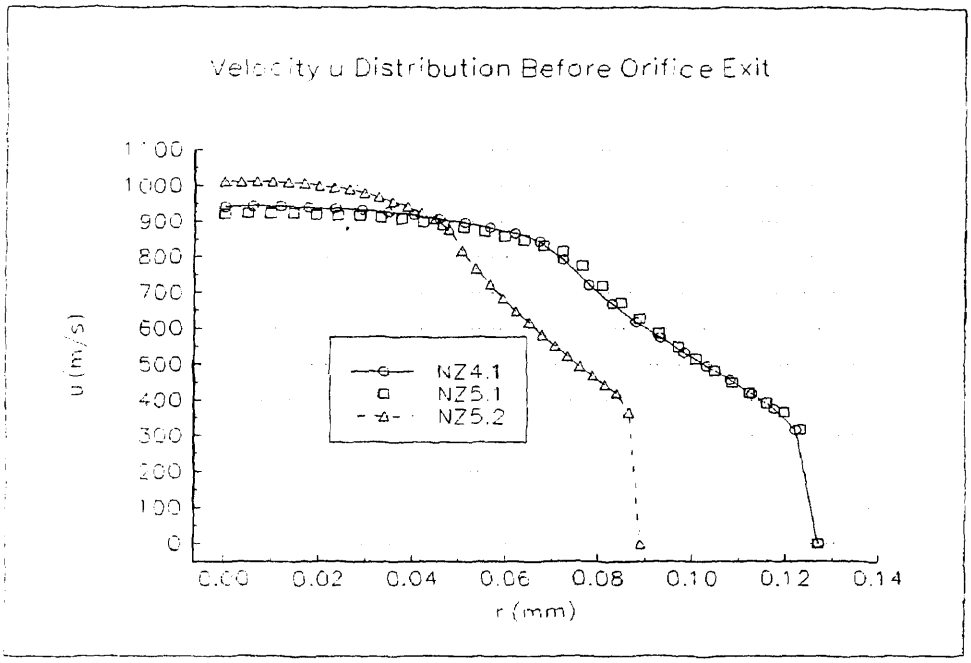

Figure E.18 Velocity (u) at the Orifice exit of the Nozzles NZ4 and NZ5

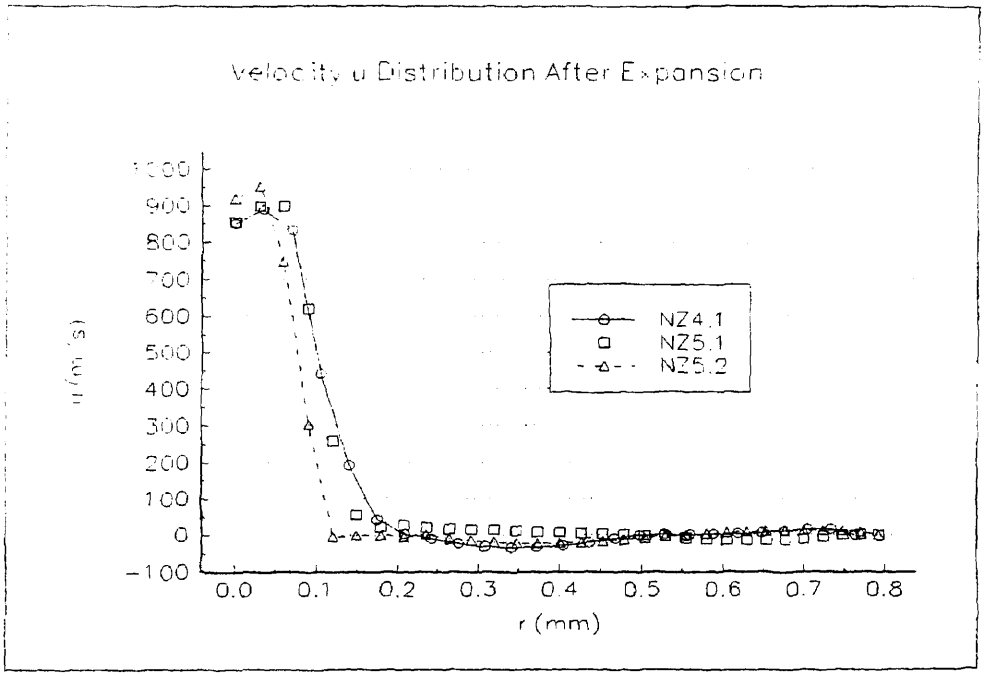

Figure E.19 Velocity (u) Distribution after Expansion of the Nozzles NZ4 and NZ5

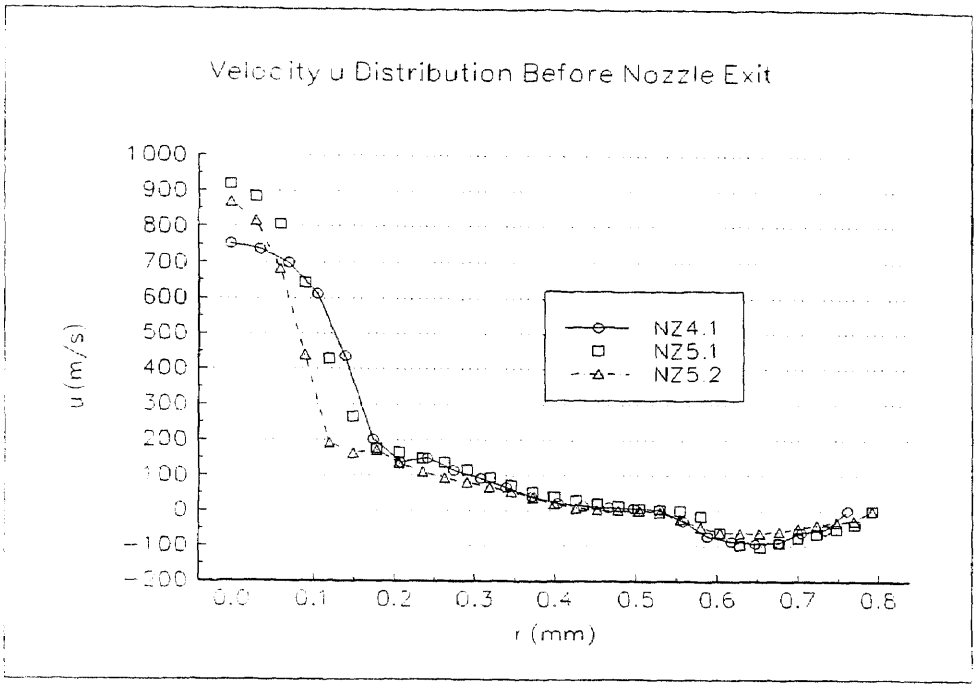

Figure E.20 Velocity (u) Distribution at the Exit of the Nozzles NZ4 and NZ5

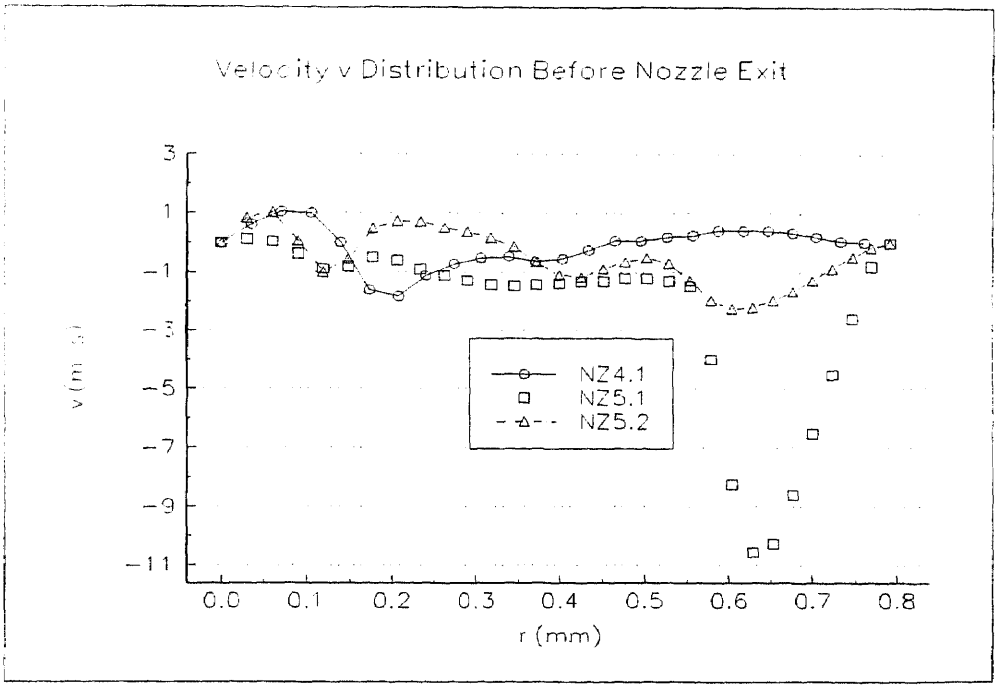

Figure E.21 Velocity (v) Distribution at the Exit of the Nozzles NZ4 and NZ5

APPENDIX F

COMPUTER PROGRAM LISTING FOR FIDAP 6.01

About thirty programs for five different nozzles configurations have been used in the numerical simulations. Two typical programs are listed in this appendix. The second one shows how user supplied input flow profiles can be implemented in the program.

F.1 Program for Nozzle NZ1.4 (d=0.254 mm, t1=60^0)

```
*NOINTERACTIVE
*title
2-D axi-symm turb flow thru 60 deg conv'd d=0.010in
*fimesh(2-d,imax=7,jmax=3)
expi
/1  2  3  4  5  6  7  8  9  10  11
1   0  31 0  47 0  57
expj
/1  2  3  4  5  6  7
1  0  11
point
1  1  1  1  0.0  0.0  0.0
2  3  1  1  1.598 0.0  0.0
3  5  1  1  1.6829 0.0  0.0
4  7  1  1  1.9379 0.0  0.0
5  1  3  1  0.0  0.1598  0.0
6  3  3  1  1.598  0.1598  0.0
7  5  3  1  1.6829 0.0127  0.0
8  7  3  1  1.9379 0.0127  0.0
line
1 2 .98
5 6  .98
3 2 1.01
7 6 1.01
3 4 1.004
7 8 1.004
5 1 1.006
6 2 1.006
7 3 1.006
8 4 1.006
```

```
surface
1  8
bcnode(uzc)
1 5  400
bcnode(velo)
8 7 0
7 6 0
6 5 0
bcnode(urc)
1 5 0
1 4 0
bcnode(kinetic)
1  5  1.6e3
bcnode(dissipation)
1  5  4.005e7
number
2  1
elements(quadrilateral,nodes=4,all)
elements(boundary,face)
8 7
7 6
6 5
bcnode(coordinate)
7 7 1
6 6 1
end
*fiprep
bcsystem(set=1,corner)
problem(nonlinear,axi-symmetric,turbulent)
pressure(mixed=1.0e-14,discontinuous)
execution(newjob)
icnode(uzc,const=400.0)
icnode(kinetic,const=1.6e4)
icnode(dissipation,const=4.005e8)
density(const=1.0)
viscosity(k.e.,clip=1e6)
1.0e-2
solution(segregated=800,reform=6,pprojection,velconv=0.00010)
relaxation
.3 .3 0 0 0 0 .7 .7
options(upwinding)
upwinding
6 6 0 0 0 0 8 8
/dataprint(control)
/printout(none)
```

```
nodes(fimesh)
elements(quadrilateral,nodes=4,fimesh)
elements(wall,nodes=2,fimesh)
elements(wall,nodes=2,fimesh)
elements(wall,nodes=2,fimesh)
renumber
end
*end
```

F.2a Program for Nozzle NZ4.1

```
*NOINTERACTIVE
*title
2-D axi-symm turb flow sap noz d=0.01in
*fimesh(2-d,imax=11,jmax=7)
expi
/1  2  3  4  5  6  7  8  9  10  11
1   0  15 0  39 0  55  0  79  0  131
expj
/1  2  3  4  5  6  7
1   0  25  0  37 0  55
point
1  1  1  1  0.0  0.0  0.0
2  3  1  1  0.254 0.0  0.0
3  5  1  1  0.345 0.0  0.0
4  7  1  1  0.475 0.0  0.0
5  9  1  1  0.584 0.0  0.0
6  11 1  1  1.415 0.0  0.0
7  1  3  1  0.0  0.0127  0.0
8  3  3  1  0.254 0.0127  0.0
9  5  3  1  0.345 0.0127  0.0
10  7  3  1 0.475 0.0127  0.0
11  9  3  1 0.584 0.0762  0.0
12  11 3  1 1.415 0.0762  0.0
13  1  5  1  0.0  0.086  0.0
14  3  5  1  0.254 0.086  0.0
15  5  5  1  0.345 0.114 0
16  1  7  1  0.0  0.1598  0.0
17  3  7  1  0.254 0.1598 0.0
18  5  7  1  0.345 0.213  0.0
line
1 2 1.01
7 8 1.01
13 14 1.01
```

```
16 17 1.01
3 2 1.01
9 8 1.01
15 14 1.01
18 17  1.01
3 4 .9
9 10 .9
4 5 1.05
10 11 1.05
5 6 1.02
11 12 1.02
7 1 1.01
8 2 1.01
9 3 1.01
10 4 1.01
11 5 1.01
12 6 1.01
7 13 2.5 3
8 14 2.5 3
9 15 2.5  3
16 13 1.01
17 14 1.01
18 15 1.01
surface
1   18
3   12
bcnode(uzc)
1 16  400
/if use subroutine uncomment the following lines
/bcnode(uzc,subroutine=1)
/1 16
bcnode(velo)
12 11 0
11 10 0
10 9 0
9 18 0
18 17 0
17 16 0
bcnode(urc)
1 16 0
1 6 0
bcnode(kinetic)
1   16  2.24e4
/if use subroutine uncomment the following lines
/bcnode(kinetic,subroutine=2)
```

```
/1 16
bcnode(dissipation)
1  16  2.64e9
/if use subroutine uncomment the following lines
/bcnode(dissipation,subroutine=3)
/1 16
number
2  1
elements(quadrilateral,nodes=4,all)
elements(boundary,face)
12  11
11  10
10  9
9   18
18  17
17  16
end
*fiprep
problem(nonlinear,axi-symmetric,turbulent)
pressure(mixed=1.0e-14,discontinuous)
execution(newjob)
icnode(uzc,const=400.0)
icnode(kinetic,const=2.24e4)
icnode(dissipation,const=2.64e9)
density(const=1.0)
viscosity(k.e.)
1.0e-2
solution(segregated=900,reform=6,pprojection,velconv=0.00010)
relaxation
.5 .5 0 0 0 0 .7 .7
options(upwinding)
upwinding
5 5 0 0 0 0 5 5
nodes(fimesh)
elements(quadrilateral,nodes=4,fimesh)
elements(wall,nodes=2,fimesh)
elements(wall,nodes=2,fimesh)
elements(wall,nodes=2,fimesh)
elements(wall,nodes=2,fimesh)
elements(wall,nodes=2,fimesh)
elements(wall,nodes=2,fimesh)
renumber
end
*end
```

F.2b Subroutine for Input Flow profiles for Nozzle NZ4.1

```
    SUBROUTINE USRBC
(X,NODEP,VALNOD,NPOINT,VAL,NVAL,SUB,NDF,IERR)
C
C   USER SUPPLIED SUBROUTINE FOR THE DEFINITION OF BOUNDARY
VALUES
C
C   INPUT:
C   =====
C   SUB    THE VALUE SPECIFIED ON THE CONTROL CARD "SUBR=SUB"
C   X(3,*)  COORDINATES OF POINTS
C   NPOINT  NUMBER OF POINTS ON CURRENT BCNODE REQUEST
C   NODEP   (NPOINT) LIST OF THESE NODES
C   NDF    DEGREE OF FREEDOM
C
C   INPUT/OUTPUT:
C   ============
C   VALNOD  (INPUT) IF THE NODES ARE ALONG A LOGICAL LINE,
VALNOD(I)
C          IS THE DISTANCE FROM VALNOD(1) ALONG THE LINE
C          (OUTPUT) BOUNDARY VALUE FOR NODE NODEP(I)
C   VAL(NVAL) (INPUT) 4 VALUES SPECIFIED ON DATA CARD AFTER IP1 IP2
C           (OUTPUT) VAL(1) NCURV
C                 VAL(2) FAC
C
C   OUTPUT:
C   ======
C   IERR =  0 NORMAL COMPLETION
C       .GT.0 ERROR
C
    IMPLICIT DOUBLE PRECISION (A-H,O-Z)
c    DIMENSION X(3,*),VAL(4),VALNOD(NPOINT),NODEP(NPOINT)
    DIMENSION x(3,*),val(*),valnod(*),nodep(*)
c    IERR = 0
C
C   INSERT HERE NORMAL EXECUTION COMMANDS
c
    r=0.1598
    ur=425.0
    xm=6.4
    const=0.09
    if (sub .gt. 1) go to 100
    do 10 i=1,npoint
    y=(r-x(2,nodep(i)))
```

```
      valnod(i)=ur*(y/r)**(1/xm)
   10 continue
c     valnod(1)=-valnod(1)
      return
  100 if (sub .gt. 2) go to 200
      do 20 i=1,npoint
      y=(r-x(2,nodep(i)))
      el=r*(0.14-0.08*(1-y/r)**2-0.06*(1-y/r)**4)
      dudy=abs(ur/xm*(1/r)**(1/xm)*(1/y)**((xm-1)/xm))
c     valnod(i)=const*(el*dudy)**2
      valnod(i)=(const**0.5)*((el*dudy)**2)
   20 continue
      return
  200 do 30 i=1,npoint
      y=(r-x(2,nodep(i)))
      el=r*(0.14-0.08*(1-y/r)**2-0.06*(1-y/r)**4)
c     dudy=abs(ur/xm*(1/r)**(1/xm)*y**((1-xm)/xm))
      dudy=abs(ur/xm*(1/r)**(1/xm)*(1/y)**((xm-1)/xm))
c     valnod(i)=el**2*dudy**3
      ek=(const**0.5)*((el*dudy)**2)
      valnod(i)=const*(ek**2)*(1/(el**2*dudy))
   30 continue
C     RETURN
C
C     ON ERROR SET IERR TO POSITIVE
C
c     IERR = 1
C     DELETE NEXT LINE
c     CALL ERMESG (2303,0,0,0)
      RETURN
C
      END
```

BIBLIOGRAPHY

Abramovich, G. N. 1948. *Turbulent Free Jets of Liquid and Gas*: Moscow.

Abramovich, G. N. 1963. *The Theory of Turbulent Jets.* Cambridge: MIT Press.

Amano, R. S. and Neusen, K. F. 1982. "A numerical and Experimental Investigation of High-Velocity Jets Impinging on Flat Plate." *6th International Symposium on Jet Cutting Technology.* 6: c3.107-c3.122.

Baker, C. R. and Selberg, B. P. 1978. "Water Jet Nozzle Performance Tests." *4th International Symposium of Jet Cutting Technology.* 4: A.11-A.14.

Baskharone, E. A. 1991. "Finite-Element Analysis of Turbulent Flow in Annular Exhaust Diffusers of Gas Turbine Engines." *Journal of Fluids Engineering. Transactions of the ASME.* 113: 104-110.

Batchelor, G. K. 1953. *The Theory of Homogeneous Turbulence.* Cambridge: University Press.

Chen, W. L. 1990. *Correlation Between Particles Velocities and Conditions of Abrasive Water Jet Formation.* Ph. D. Dissertation New Jersey Institute of Technology.

Cherdron, W., Durst, F. and Whitelaw, J. H. 1977. "Asymmetric Flows and Instabilities in Symmetric Ducts with Sudden Expansion." *Journal of Fluid Mechanics.* 84: 13-.

Davies, T. W., Metcalfe, R. A. and Jackson, M. K. 1980. "The Anatomy and Impact Characteristics of Large Scale Water Jets." *5th International Symposium of Jet Cutting Technology.* 5: A2.15 - A2.32.

Dunne, B. and Cassen, B. 1954. "Some Phenomena Associated with Supersonic Liquid Jets." *Journal of Applied Physics.* 25; 5: 569- 572.

Dunne, B. and Cassen, B. 1956. "Velocity Discontinuity Instability of a Liquid Jet." *Journal of Applied Physics.* 27; 6: 577-582

Durst, F., Melling, A., and Whitelaw, J. H. 1974. "Low Reynolds Number Flow Over a Symmetrical Sudden Expansion." *Journal of Fluid Mechanics.* 64:111-.

Durst, F., Pereira, J. C. F. and Tropea, C. 1993. "The Plane Symmetric Sudden Expansion Flow at Low Reynolds Numbers." *Journal of Fluid Mechanics.* 248: 567-581.

Eddingfield, D. L., Evers, J. L. and Setrok, A. 1981. "Mathematical Modeling of High Velocity Water Jets." *1st U. S. Water Conference.* 1: I-3.1 - I-3.14.

BIBLIOGRAPHY
(Continued)

Edwards, D. G. and Welsh, D. J. 1978. "A Numerical Study of Nozzle Design For Pulsed Water Jets." *Fourth International Symposium on Jet Cutting Technology.* 4: B1.1 -B1.12.

Edwards, D. G., Smith, R. M. and Farmer, G. 1982. "The Coherence of Impulsive Water Jets." *6th International Symposium of Jet Cutting Technology.* 6: C4.123 - C4.140.

Field, J. E. and Lesser, M. B. 1977. "On the Mechanics of High Speed Liquid Jets." *Proc. R. Soc. Lond.* A.357: 143-162.

Habib, M. A. and Whitelaw, J. H. 1982. "The Calculation of Turbulent Flow in Wide-Angle Diffusers." *Numerical Heat Transfer.* 5: 145-164.

Hetsroni, G. and Sokolov, M. 1971. "Distribution of Mass, Velocity, and Intensity of Turbulence in a Two-Phase Turbulent Jet." *Journal of Applied Mechanics.* Transactions of the ASME: 315-326.

Himmelreich, U. and Riess, W. 1991. "Laser Velocimetry Investigations of the Flow in Abrasive Water Jets with Varying Cutting Head Geometry." *Proceedings of the 6th American Water Jet Conference. 6:* 355-370.

Hinze, J. O. 1975. *Turbulence.* Second Edition. New York: McGraw-Hill.

Hishida, K., Nakano, H. and Maeda, M. 1989. "Turbulent Flow Characteristics of Liquid-Solid Particle Confined Jet." *International Conference on Two-Phase Flows.* Taipei: 209-214.

Hjelmfelt, A. T. and Mockros, L. F. 1965. "Motion of Discrete Particles in a Turbulent Fluid." *Appl. Sci. Res.* 16: 149-161.

Hoffmann, J. A. and Gonzalez, G. 1984. "Effects of Small-Acale, High Intensity Inlet Turbulence on Flow in a Two-Dimensional Diffuser." *Journal of Fluids Engineering.* 106: 121-124.

Lai, M. K. Y., Vijay, M. M. and Zou, C. 1991. "Computational Fluid Dynamics Analysis of Submerged Cavitating Water Jets." *6th American Water Jet Conference.* 6: 411-426.

Launder, B. E. 1984. "Second-Moment Closure: Methodology and Practice." *Turbulence Models and Their Applications.* 2, Eyrolles.

BIBLIOGRAPHY
(Continued)

Launder, B. E. and Spalding, D. B. 1972. *Lectures in Mathematical Models of Turbulence.* Academic Press.

Launder, B. E. and Spalding, D. B. 1974. "The Numerical Computation of Turbulent Flows." *Computer Methods in Applied Mechanics and Engineering.* 3: 269-289.

Leach, S. J. and Walker, G. L. 1966. "The Application of High Speed Liquid Jets to Cutting." *Phil Trans. Royal Soc.* 260:295-308.

Murphy, J. D. 1984. *Turbulence Modeling.* NASA Technical Memorandum 85889.

Nallasamy, M. 1985. "A Critical Evaluation of Various Turbulence Models as Applied to Internal Fluid Flows." *NASA Technical Paper 2474.*

Neusen, K. F., Gores, T. J. and Labus, T. J. 1992. "Measurement of Particle and Drop Velocities in a Mixed Abrasive Water Jet using a Forward-Scatter LDV System." *Jet Cutting Technology, 11th International Conference.* 11: 63-73.

Noumi, M. and Yamaoto, K. 1992. "Flow Characteristics and Impact Phenomena of Pulsed Water Jets." *The Third Pacific Rim International Conference on Water Jet Technology.* 3: 47-58.

Patankar, S. V. and Spalding, D. B. 1970. *Heat and Mass Transfer in Boundary Layers.* Second Edition. London: Intertext.

Parthasarathy, R. N. and Faeth, G. M. 1987. "Structure of Particle-Laden Turbulent Water Jets in Still Water." *Intl. J. Multiphase Flow.* 13.5: 699-716.

Phinney, R. E. 1973. "The Breakup of a Turbulent Liquid Jet in a Gaseous Atmosphere." *Journal of Fluid Mechanics.* 60; 4:689-701.

Rajaratnam, N. 1976. *Turbulent Jets.* Elsevier.

Restivo, A. and Whitelaw, J. H. 1978. "Turbulence Characteristics of the Flow Downstream of a Symmetric, Plane Suuden Expansion." *Journal of Fluids Engineering. Transactions of the ASME.* 100: 308-310.

Rodi, W. 1980. *Turbulence Models and Their Applications in Hydraulics.* International Association for Hydraulic Research, The Netherlands.

BIBLIOGRAPHY
(Continued)

Sala, R., Vivarelli, P. L. and Garuti, G. 1980. "Numerical Analysis of Wide-Angled Diffusers in Turbulent Flow." *Journal of the Hydraulics. ASCE Proceedings. Hydraulics Division.* 106: 629-647.

Schlichting, H. 1979. *Boundary Layer Theory.* McGraw-Hill.

Semerchan, A. A., Vereshchagin, L. F., Filler, F. M. and Kuzin, N. N. 1958. "Distribution of Momentum in a Continuous Liquid Jet of Supersonic Velocity." *Sov. Phys. - Tech. Phys.* 3; 9:1894-1903.

Shavlovsky, D. S. 1972. "Hydrodynamics of High Pressure Fine Continuous Jets." *1st International Symposium of Jet Cutting Technology.* 1: A6.81 - A6.92.

Smyth, R. 1976. "Experimental Study of Turbulence in Plane Separated Flows." *Proc. of ISL/AGARD workshop on Laser Anemometry.* p. 223.

Swanson, R. K., Kilman, M., Cerwin, S. and Tarver, W. 1987. "Study of Particle Velocities in Water Driven Abrasive Jet Cutting." *Proceedings of the 4th U. S. Water Jet Conference.* 4: 103-107.

Tropea, C., Weiser, W. and Nitsche, W. 1989. "Experimental Investigation of the Flow Through Axisymmetric Expansions." *Journal of Fluids Engineering. Transactions of the ASME.* 111: 464-471.

Vijay, M. M, Hu, S. G. and Lai, M. K. Y. 1993. "Enhancing the Performance of Cavitating Water Jets." *7th American Water Jet Conference.* 7: 233-250.

Yanaida, K. and Ohashi, A. 1978. "Flow Characteristics of Water Jets in Air." *Fourth International Symposium on Jet Cutting Technology.* 4: A3-39-A3-54.